



**HAL**  
open science

# Development of an optical system for preclinical molecular imaging of atherothrombosis

Dinh Hoang Nguyen

► **To cite this version:**

Dinh Hoang Nguyen. Development of an optical system for preclinical molecular imaging of atherothrombosis. Imaging. Université Sorbonne Paris Cité, 2017. English. NNT : 2017USPCD062 . tel-02294001

**HAL Id: tel-02294001**

**<https://theses.hal.science/tel-02294001>**

Submitted on 23 Sep 2019

**HAL** is a multi-disciplinary open access archive for the deposit and dissemination of scientific research documents, whether they are published or not. The documents may come from teaching and research institutions in France or abroad, or from public or private research centers.

L'archive ouverte pluridisciplinaire **HAL**, est destinée au dépôt et à la diffusion de documents scientifiques de niveau recherche, publiés ou non, émanant des établissements d'enseignement et de recherche français ou étrangers, des laboratoires publics ou privés.



**LABORATOIRE DE PHYSIQUE DES LASERS-CNRS UMR7538**

**LABORATOIRE DE RECHERCHES VASCULAIRES TRANSLATIONNELLES**

**INSERM U1148**

## **THÈSE**

Présentée pour obtenir le grade de

DOCTEUR EN PHYSIQUE

DE L'UNIVERSITÉ PARIS 13

Par

Nguyễn Đình Hoàng

# **Development of an optical system for preclinical molecular imaging of atherothrombosis**

Soutenue le 21 Décembre 2017 devant le jury composé de:

Mme Christine MENAGER	Rapporteur
Mr Thierry GACOIN	Rapporteur
Mme Laurence MOTTE	Examinatrice
M. Phalla OU	Examinateur
M. Ngoc-Diep LAI	Examinateur
M. Eric TINET	co-superviseur
M. Jean-Michel TUALLE	co-Directeur de thèse
M. Frédéric CHAUBET	co-Directeur de thèse

I, Nguyen Dinh Hoang confirm that the work presented in this thesis is my own. Where information has been derived from other sources, I confirm that this has been indicated in the thesis.

## **Acknowledgements**

Firstly, I would like to express my very great appreciation to director Jean-Michel Tualle, who has supported me throughout my thesis with his patience and knowledge. I appreciate all his contributions of time, ideas, and funding to make my Ph.D, experience productive and stimulation.

I would like to offer my special thanks to my director Frédéric Chaubet. It has been an honor to be his student. He taught me a lot about synthesis of nanoparticles and coating them for biocompatible to recognize thrombus giving me all chemical material to synthesize nanoparticles.

My thesis would not successful without good advices of professor Nouredine Jouini. His contributions on synthesis of nanoparticle and analyzing nanoparticles are very valuable to me.

I would also like to acknowledge Eric Tinet for his experience on data processing and computer engineering. He also supports, advice and stamina me on every experiment.

I would like to thank Thierry Gacoin from Ecole Polytechnique and Christine Ménager from Pierre and Marie Curie University for their time spent on reviewing the manuscript and for their comments.

I want to acknowledge professor Phalla Ou from Bichat-Claude Bernard Hospital, Lai Ngoc Diep from Université Paris-Saclay, and Laurence Motte from University Paris 13 who accepted to examine my works.

The members of the Laboratoire de Physique des Lasers group and Laboratoire de Recherche Vasculaire Translationnelle group have contributed immensely to my personal and professional time at University Paris 13.

I wish to acknowledge the help provided by Ovidiu Brinza, Thierry Chauveau, Silvana Mercone, LSPM - UPR 3407/CNRS, University Paris 13 for TEM, XRD and magnetic measurements.

I am particularly grateful for the advices, coating nanoparticles and characteristic measurements assistance given by Laurence Motte, Frederic Geinguenaud, Yoann Lalatonne, Inserm, U1148, LVTS, Science, UFR SMBH, University Paris 13.

Clément Journé, Inserm, U1148, LVTS, University Paris 7, Sorbonne Paris Cité, CHU X Bichat provided me with very valuable MRI data and useful imaging tool.

I would like to thank Marie-Claire Schanne-Klein, Ecole Polytechnique for imaging with the second-harmonic microscopy and differential interference contrast microscopy.

Lastly, I would like to thank my family and my friend for all their love and encouragement. For my parents who raised me with a love of science and supported me in all my pursuits.

## Abstract

In this thesis work, we develop optical imaging protocols for the observation of the nanoparticles on tissue slices in order to further link their localization and their “behaviour” to the biological pathological environment. Bimodal zinc and iron oxide-based MRI/optical nanoparticle contrast agents (Zn(Fe)O) have been synthesised with a novel azeotropic polyol method in glycol solvents (DEG and PG). The most potent NPs, as regard to their MR contrast power, have been coated with carboxymethyl pullulan, polyethylene glycol, carboxymethyl dextran (CMD) and fucoidan, the latter being a polysaccharide able to specifically bind to the vascular wall. The coated NPs were injected into rat to locate atherothrombosis by MRI. Then the histological slices of harvested diseased tissue were imaged with our homemade optical microscope. Water removal using Dean-Stark apparatus is a novel strategy for the synthesis of NPs in polyol solution with high yield and small size. The NPs show the good magnetic and optical properties at room temperature. The coated nanoparticles were injected into an atherothrombotic rat model to locate the thrombus by MRI prior to sacrifice of the animals and tissue collection for histological study by optical microscopy. The difference of MRI images between before and after injection with Fucoidan-NPs and CMD-NPs is clear. The results indicated that fucoidan-NPs are linked to the thrombus. Some type of microscopies, such as fluorescent microscopy, dark field microscopy, hyperspectral dark field microscopy and interference dark field microscopy have been developed for the detection of NPs in liquid medium and in the histological tissue. By analyzing the spectrum of every pixel and comparing to the spectrum of reference materials, hyperspectral microscopy can detect the presence of nanomaterial on exposed tissue slices, locate, identify, and characterize them. Zn(Fe)O NPs would therefore constitute a potential bimodal contrast agent for MRI and optical imaging. Although many advance optical tools have been developed, but we found it is still a challenge to identify reliably the NPs in the tissue.

## Résumé

Dans ce travail de thèse, nous développons des protocoles d'imagerie optique pour l'observation des nanoparticules sur des coupes de tissus afin de relier leur localisation et leur «comportement» à l'environnement biologique, en particulier son éventuel état pathologique. Nous avons synthétisé des agents de contraste bimodaux, sous forme de nanoparticules -NP- visibles en résonance magnétique et en optique, à base d'oxydes de fer et de zinc (Zn(Fe)O) avec une nouvelle méthode de polyol azéotropique dans des solvants glycoliques (DEG et PG). L'élimination de l'eau à l'aide de l'appareil Dean-Stark est une nouvelle stratégie pour la synthèse de NP dans une solution de polyol, avec un rendement élevé et produisant des particules de petite taille. Les NP les plus visibles, selon leur contraste IRM, ont été revêtus de carboxyméthyl pullulane, de polyéthylène glycol, de carboxyméthyl dextrane et de fucoïdane, ce dernier étant un polysaccharide capable de se lier spécifiquement à la paroi vasculaire. Les NPs montrent de bonnes propriétés magnétiques et optiques à température ambiante. Les NP recouvertes ont été injectées dans un modèle de rat d'athérombose pour localiser le thrombus par IRM avant sacrifice et collecte des tissus pour étude des coupes histologiques par microscopie optique. La différence entre les images IRM avant et après l'injection de fucoïdane-NPs et de CMD-NPs est claire. Les résultats montrent que les NP recouvertes de fucoïdane sont liées au thrombus. Certains types de microscopies, tels que la microscopie de fluorescence, la microscopie en champ sombre, la microscopie hyperspectrale à champ sombre et la microscopie interférentielle à champ sombre ont été développés pour la détection des NPs en milieu liquide et dans les tissus. En analysant le spectre de chaque pixel et en le comparant au spectre des matériaux de référence, la microscopie hyperspectrale peut détecter la présence de NPs sur des coupes de tissus, les localiser, les identifier et les caractériser. Zn(Fe)O NPs constituerait donc un agent de contraste bimodal potentiel pour l'IRM et l'imagerie optique. Cependant, bien que de nombreux outils optiques avancés aient été développés, nous avons constaté qu'il est toujours difficile d'identifier de manière fiable les NP dans le tissu.

## Contents

Acknowledgements.....	i
Abstract .....	iii
Résumé .....	iv
Contents .....	v
List of figures .....	viii
List of tables .....	xiii
List of abbreviations .....	xiv
Introduction .....	1
<b>Chapter 1. Bibliography.....</b>	<b>4</b>
1.1. Atherothrombosis.....	4
1.2. Platelets and atherothrombosis .....	5
1.3. Medical imaging modalities .....	6
1.3.1. X-ray projection imaging .....	6
1.3.2. Computed tomography .....	6
1.3.3. Nuclear imaging.....	7
1.3.4. Ultrasound imaging.....	7
1.3.5. Magnetic resonance imaging.....	8
1.3.6. Optical imaging.....	8
1.3.7. Conclusions.....	10
1.4. MRI contrast agent.....	11
1.4.1. Relaxivity.....	11
1.4.2. T <sub>1</sub> contrast agent.....	12
1.4.3. T <sub>2</sub> contrast agent.....	12
1.5. Zinc oxide .....	13
1.6. Bimodal MRI/optical contrast agents .....	14
1.7. The biospecificity of contrast agents .....	15
1.8. Strategy of the project .....	16

<b>Chapter 2. Chemistry .....</b>	<b>18</b>
2.1. Materials and methods .....	19
2.1.1. Synthesis of NPs .....	19
2.1.2. Iron concentration measurement by UV-visible spectrophotometry.....	20
2.1.3. Iron and zinc concentration measurement by AAS .....	21
2.1.4. Coatings .....	21
2.1.5. Fucoidan content .....	22
2.1.6. Particle size analysis and isoelectric point analysis.....	23
2.1.7. UV-visible and fluorescence spectroscopy .....	23
2.1.8. FT-IR spectroscopy .....	23
2.1.9. Magnetic properties.....	24
2.1.10. Relaxivity.....	24
2.1.11. Transmission electron microscopy.....	24
2.1.12. X-ray diffraction .....	24
2.1.13. Thermogravimetric analysis .....	25
2.2. Results and discussion.....	25
2.2.1. Synthesis of NPs in propylene glycol .....	25
2.2.2. Synthesis of NPs in diethylene glycol.....	28
2.2.3. Conclusion .....	42
<b>Chapter 3. Optics.....</b>	<b>43</b>
3.1. Development of the optical system.....	43
3.1.1. Fluorescence microscopy .....	43
3.1.2. Simple dark field microscopy .....	44
3.1.3. Dark field interference microscopy .....	44
3.1.4. Dark field hyperspectral microscopy .....	46
3.2. Use of NPs with optical system .....	47
3.2.1. Dark field microscopy for real-time 2D NPs tracking.....	47
3.2.2. Dark field interference microscopy for 3D NPs tracking .....	54
3.2.3. Dark field hyperspectral microscopy for locating NPs.....	62
3.1. Conclusion .....	64
<b>Chapter 4. Imaging.....</b>	<b>65</b>

4.1. MRI .....	65
4.1.1. Materials and methods .....	65
4.1.2. Results and discussion.....	66
4.2. Optical imaging.....	70
4.2.1. Perls' Prussian Blue Staining .....	70
4.2.2. Healthy vessel and diseased vessel.....	70
4.2.3. Images of atherothrombosis.....	72
4.3. Conclusion.....	74
General discussion.....	76
General conclusion and perspectives.....	79
Bibliography .....	81
Appendix A. Characterization techniques .....	99
Appendix B. Microscopy basics .....	106
Appendix C. List of synthesis NPs experiments .....	113
Appendix D. Synthesis of ZnO NPs in PG without azeotropic distillation .....	117
Appendix E. Synthesis of NPs in DEG without azeotropic distillation .....	118
Appendix F. Carboxymethyl pullulan synthesis .....	121
Appendix G. Characterization of PEG-NPs .....	123
Appendix H. Characterization of Fucoidan-NPs with different Fe concentration ...	125
Appendix I. TEM images, size distribution and XRD spectra.....	127
Appendix J. XRD analysis report .....	128
Appendix K. Gaussian fit and center of mass method.....	130
Appendix L. Accuracy of the 3D location algorithm .....	134
Appendix M. Matlab code for hyperspectral microscopy imaging.....	135
Appendix N. Determination of iron content of the NPs by visible spectroscopy ....	137

## List of figures

Figure 1.1. The development of atherosclerosis up to atherothrombosis. The evolution of the process is depicted from the left to the right, from the very beginning (early fat streaks formation) to the rupture of the atherosclerotic plaque and the thrombotic event. .5	
Figure 2.1. Experimental setup for synthesis of NPs with Dean-Stark apparatus. .... 20	20
Figure 2.2. TEM images and size distribution of PG-ZnO NPs without water. .... 26	26
Figure 2.3. TEM images and size distribution of PG-0.2 NPs..... 26	26
Figure 2.4. XRD diffractogram of PG-ZnO (left) and PG-0.2 (right) NPs. .... 27	27
Figure 2.5. Magnetization (M) versus temperature (left) and versus applied field (H) at 5 K and 300 K (right) synthesized in PG. .... 28	28
Figure 2.6. TEM images of $R_{Fe, i} = 0.05$ (a), 0.20 (b) and 0.50 (c). .... 29	29
Figure 2.7. XRD diffractograms of $R_{Fe, i} = 0.05, 0.10, 0.15, 0.35$ and 0.50. .... 29	29
Figure 2.8. Wurtzite structure: (a) unit cell; (b) hexagonal structure [121]. .... 30	30
Figure 2.9. TEM images of fuco-0.35 (a) and fuco-0.50 (b). .... 32	32
Figure 2.10. $R_{Fe, i} = 0.50$ (left), fuco-0.50 (middle), and fuco-0.50 with applied magnetic field (right) in PBS..... 34	34
Figure 2.11. Size distribution of fuco-0.50 (a), and CMD-0.50 (b). .... 34	34
Figure 2.12. Magnetization (M) versus temperature (a), versus applied field (H) at 5 K and 300 K (b) of $R_{Fe, i} = 0.50$ , and versus applied field (H) of $R_{Fe, i} = 0.50$ , fuco-0.50 and CMD-0.50 in water(c, d). .... 36	36
Figure 2.13. Absorption spectra (left) and fluorescence spectra (right) of $R_{Fe, i} = 0.50$ , fuco-0.50, and CMD-0.50 with 370 nm excitation wavelength..... 36	36
Figure 2.14. IR absorption spectra of $R_{Fe, i} = 0.50$ (a), fuco-0.50 (b), and CMD-0.50 (c). 37	37
Figure 2.15. Thermogram of fuco-0.50 and CMD-0.50. .... 38	38
Figure 2.16. MRI image (left) and relaxivity determination of Fucoidan-NPs suspension ( $R_{Fe}=0.5$ ) with ( $C_{Fe} = 0.7$ (A), 0.303(B), 0.147(C), 0.113(D), 0.0774(E), 0.0522(F), and 0.0261(G) mM. .... 40	40
Figure 3.1. Fluorescence microscopy configuration. .... 43	43
Figure 3.2. Dark field microscopy configuration. .... 44	44
Figure 3.3. Dark field interference microscopy configuration..... 45	45

Figure 3.4. Dark field image of NP (a), reference laser beam (b) and interference image (c). .....	46
Figure 3.5. Hyperspectral dark field microscope configuration. ....	46
Figure 3.6. The flow charts for estimating particle size distribution. ....	47
Figure 3.7. Image of single a single NP before (left) and after applying a gaussian filter (right).....	48
Figure 3.8. Peaks detection algorithm, a pixel is determined as a peak if it is stronger than at least 16 nearby pixel in 8 different directions. ....	49
Figure 3.9. ROI Image (left) 2D Gaussian function is applied to locate center more precisely (right).....	50
Figure 3.10. Brownian motion of NPs in DEG. ....	52
Figure 3.11. Estimation of the diffusion coefficient.....	52
Figure 3.12. Hydrodynamic size of $R_{Fe, i} = 0.2$ NPs measured by NTA.....	53
Figure 3.12. TEM image and size distribution of $R_{Fe, i} = 0.2$ NPs. ....	53
Figure 3.13. Hydrodynamic size of CMP-NPs measured by NTA and DLS. ....	53
Figure 3.14. Flow-charts for 3d NPs tracking analysis. ....	55
Figure 3.15. Dark field interference image before (left) and after (right) background subtraction. ....	56
Figure 3.16. Interference images of NP as a function of z: 0 $\mu\text{m}$ (a), 20 $\mu\text{m}$ (b), 40 $\mu\text{m}$ (c), and 100 $\mu\text{m}$ (d). ....	57
Figure 3.17. Original interference image (a) and its reconstruction images at different depths z: 70 $\mu\text{m}$ (b), 80 $\mu\text{m}$ (c), and 95 $\mu\text{m}$ (d).....	58
Figure 3.18. Contrast of reconstruct image versus z. ....	58
Figure 3.19. Gaussian fitting for precise determination. ....	59
Figure 3.20. Reconstruction image versus z. ....	60
Figure 3.21. Brownian movement of NP in medium. ....	61
Figure 3.22. The diffusion coefficient estimation. ....	61
Figure 3.23. Refection spectra of four materials present in a slice. ....	63
Figure 3.24. Image of histological sample exposed to nanoparticles obtained by conventional dark field (left) microscopy and dark field hyperspectral (right) microscopy. ....	63

Figure 3.25. NPs in histological slices can be located by using suitable angle $\square$ .....	64
Figure 3.26. Image of NPs obtained via conventional dark field (left) microscopy and dark field hyperspectral (right) microscopy.....	64
Figure 4.1. MRI of atherothrombosis after Fucoidan-NPs injection.....	67
Figure 4.2. MRI of atherothrombosis after PEG-NPs injection.....	67
Figure 4.3. MR signal after NPs injection versus time.....	68
Figure 4.4. MRI of atherothrombosis after CMD-coated NPs and fucoidan-coated NPs injection.....	69
Figure 4.5. MR signal versus time after CMD-coated and fucoidan-coated NPs injection on T2* weighted MRI images. ....	69
Figure 4.6. Iron distribution (blue dots) in vessel wall. L = lumen of the vessel .....	70
Figure 4.7. Bright field imaging of a healthy vessel (left) and a diseased vessel (right)..	71
Figure 4.8. Dark field imaging of a healthy vessel (left) and a diseased vessel (right). ...	71
Figure 4.9. Bright field imaging (left) and fluorescence imaging (right) of a healthy vessel.....	71
Figure 4.10. Bright field, dark field, fluorescence, hyperspectral images of atherothrombosis. The dotted lines encircle diseased areas, the yellow dash line could be fibrin, the white plain lines can be collagen fragments, and the white arrow is probably NPs.....	72
Figure 4.11. Second-harmonic images of atherothrombosis. ....	73
Figure 4.12. DIC image of atherothrombosis.....	74
Figure A.1. Layout of optical components in a basic TEM.....	100
Figure A.2. X-rays scattered by crystal. ....	101
Figure A.3. Schematic diagram of X-ray diffractometer.....	102
Figure A.4. Schematic diagram of fluorescence spectrophotometer. ....	102
Figure A.5. Schematic diagram of DLS.....	103
Figure A.6. Schematic diagram of a vibrating sample magnetometer. ....	105
Figure B.1. Airy patterns and the limit of resolution. ....	106
Figure B.2. Some type of bright field illumination configurations: transmission (left) and reflection (right).....	110

Figure B.3. Some types of dark field illumination configuration. ....	112
Figure B.4. Bright field illumination image (left) and dark field illumination image (right) of vessel. ....	112
Figure D.1. TEM images and size distribution of PG-ZnO NPs with water. ....	117
Figure E.1. TEM image and size distribution of DEG-ZnO NPs with catalysts. ....	118
Figure E.2. XRD diffractogram of DEG-ZnO NPs synthesized with Na <sup>+</sup> . ....	118
Figure E.3. TEM image and size distribution of DEG-ZnO NPs with dried salt. ....	119
Figure E.4. TEM image and size distribution of DEG-0.01 with dried salt. ....	119
Figure E.5. TEM image and size distribution of DEG-0.2 with dried salt. ....	120
Figure E.6. XRD diffractogram of pure ZnO and DEG-0.1. ....	120
Figure F.1. Determination amount of CM in CMP .....	122
Figure F.2. Size distribution of CMP-0.50 NPs. ....	122
Figure G.1. Size distribution of PEG-0.50. ....	123
Figure G.2. Magnetization (M) versus applied field (H) of DEG-0.50 and PEG-0.50...	123
Figure G.3. Infrared absorption spectra of PEG-0.50. ....	124
Figure G.4. Thermogram of PEG-0.50. ....	124
Figure H.1. Magnetization (M) versus applied field (H) curves of fuco-NPs with different Fe concentrations. ....	125
Figure H.2. Absorption spectra of fuco-NPs with different Fe concentrations. ....	126
Figure H.3. Fluorescence spectra of fuco-NPs with excitation wavelengths of 270 nm (left) and 370nm (right) with different Fe concentrations. ....	126
Figure H.4. Infrared absorption spectral of DEG –NPs and Fu-NPs with different Fe concentration. ....	126
Figure I.1. TEM images, size distribution and XRD spectra of NPs. ....	127
Figure K.1. Simulated image of NPs with different collected photons count and noise.	131
Figure K.2. Error histograms of the center of mass method algorithm (left) and of the Gaussian fitting method algorithm, without noise .....	132
Figure K.3. Error histogram of the center of mass method algorithm (left) and the Gaussian fitting method algorithm, with shot noise .....	132

Figure K.4. Error histogram of the center of mass method algorithm (left) and the Gaussian fitting method algorithm, with shot noise and background ..... 133

Figure K.5. Error of the Gaussian fit algorithms and the center of mass algorithms versus the number of incoming photons ..... 133

Figure L.1. Simulated interference images of NP versus SNR: 10 (a), 100 (b), 1000 (c), and 10000(d)..... 134

Figure L.2. Error versus SNR (left) and distance to focus plane (right). ..... 134

Figure N.1. Determination of relationship between  $R_{Fe}$  and  $m_{Fe}/m_{NPs}$ . ..... 137

## List of tables

Table 1.1. Comparing medical imaging method.....	11
Table 2.1. Chemical analysis of Fe in NPs synthesized in PG .....	26
Table 2.2. Chemical analysis of Fe in NPs synthesized in DEG with $R_{Fe} = 0.05, 0.1, 0.15, 0.2, 0.35$ and $0.50$ .....	28
Table 2.3. Characterization of bare DEG-NPs. Rietveld refinements for NPs with $R_{Fe, i} = 0.50$ have been performed with the stoichiometry established from chemical analysis. ...	31
Table 2.4. Average hydrodynamic size and zeta potentials of NPs.....	35
Table 2.5. Characterization of coated NPs compared to references.....	41
Table 4.1. Comparing optical imaging method.....	75
Table C.1. List of synthesis NPs experiments in DEG.....	113
Table C.2. List of synthesis NPs experiments in PG.....	115
Table C.3. List of synthesis NPs experiments in mixture of DEG/PG .....	116
Table F.1. The degree of substitution of CM.....	122
Table J.1. The degree of substitution of CM.....	128
Table N.1. Estimation of $R_{Fe}$ in samples.....	137

## List of abbreviations

$\mu$ Obj	Microscope objective
AAS	Atomic absorption spectroscopy
CCD	Charge coupled device
CM	Carboxymethyl
CMD	Carboxymethyl Dextran
CMP	Carboxymethyl pullulan
DEG	Diethylene glycol
DLS	Dynamic light scattering
DMSA	Dimercaptosuccinic acid
EMCCD	Electron multiplying charge-coupled device
IR	Infrared
KDa	Kilo Dalton
MRI	Magnetic resonance imaging
MW	Molecular weight
NA	Numerical Aperture
ND	Neutral-density
NPs	Nanoparticles
NTA	Nanoparticle Tracking Analysis
PBS	Phosphate-buffered saline
PEG	Polyethylene Glycol
PG	1,2-propanediol; Propylene glycol
QDs	Quantum dots
$R_{Fe}$	Ratio Fe/(Zn+Fe) (mol/mol)
RPM	Revolutions per minute

SAM	Spectral Angle Mapper
SEM	Scanning electron microscope
SHG	Second-harmonic generation
SNR	Signal-to-noise ratio
TEM	Transmission electron microscopy
UV	Ultraviolet
XRD	X-ray diffraction

## **Introduction**

Atherothrombosis is a formation of a blood clot within an artery. The main cause of this pathological situation is atherosclerosis, which is a widespread disease and the main cause of death in the world. Despite the development of modern technologies, it is very challenging to detect atherosclerosis because of its silent and asymptomatic evolution. Atherosclerosis is also a very slow developing pathology and an early detection of this disease is considered as essential to improve the ability of successful treatments.

Diagnosing atherosclerosis using magnetic resonance imaging (MRI) is a good method that has attracted many research interests for more than three decades. However, a disadvantage of the MRI is that its spatial resolution is not good enough to detect and discriminate details at the cellular scale, which would allow a better understanding of the biological phenomena. For the last 20 years, nanotechnology provided numerous nanosystems, namely contrast agents, dedicated to improve medical imaging with the main modalities: MRI, scintigraphy, CTscan, ultrasonography and optical imaging. More specifically, nanoparticulate systems such as iron oxide nanocrystals (USPIO) and quantum dots have been widely developed for MR and optical imaging. However, these nanosystems are devoid of biospecificity which constitutes another challenge

This project aimed at producing a novel approach for better detection and diagnosis accuracy of thrombosis by combining MRI with an optical imaging technique, which resolution is far better than that of MRI. More precisely, a biospecific dual MR-optical contrast agent would be used both to localize the vascular pathological area in vivo and to get higher resolution images from histological slices prepared from the harvested tissues.

In recent few years, nanoparticles (NPs) containing iron and zinc oxide having both magnetic and fluorescent have obtained a lot of significant attraction because of their potential applications. ZnO-based nanocrystals doped up to 25 wt% Fe synthesized by the polyol method was reported with narrow size distribution by Imen Balti [1, 2, 3, 4]. Following this works, we have first synthesized bimodal zinc and iron oxide-based nanoparticle with magnetic and optical properties using diethylene glycol and propylene glycol as solvents. We found that without water, the size of NPs is smaller. In the beginning, we tried to remove all of water by using Dean-Stark apparatus just before the starting of

chemical reactions. Because of the limitation of time, we did not investigate the complete influence of water over the synthesis process. This work will be continued in future projects in the framework of the collaboration between LPL and LVTS.

The most potent NPs, as regard to their MR contrast power, have been coated with carboxymethyl pullulan, polyethylene glycol, carboxymethyl dextran and fucoidan, the latter being a polysaccharide able to specifically bind to the vascular wall.

Then the coated NPs were injected into a rat model of atherothrombosis. After localization with MRI, some histological sections of harvested diseased tissue were imaged with our homemade optical microscope. Some type of dark field microscopies, such as hyperspectral dark field microscopy and interference dark field microscopy have been developed for the detection of NPs. Some software for collecting and processing images have been developed.

The manuscript is presented as follows:

In the first part, we will briefly remind the pathological context of atherothrombosis and the ways to image the diseased arterial wall. We will also present some common kind of medical imaging modalities. For safety reasons and acceptable resolution, we chose both MRI and optical imaging to study the development of atherothrombosis. Some basic concepts of MRI and optical imaging as well as about the importance of bimodal MR/optical contrast agent will be presented.

The second chapter of the manuscript will present the synthesis of the NPs by a novel azeotropic polyol method in glycol solvents (DEG and PG) and their characterization, as well as systems, methods and models we used and developed for the imaging.

In the third part, we introduce about the development optical system used for imaging histological slides. Some of works with detecting, tracking, estimating hydrodynamic size of the NPs with homemade software will be describe. We don't focus to optimize configuration of optical system. So, we design optical system with quick installation, fast modification and good enough resolution image qualities.

The imaging results are presented and discussed in the fourth chapter where the most potent NPs, as regard to their MR contrast power and coatings have been used for in vivo

MR imaging of thrombosis followed by optical studies on histological sections from harvested tissue.

At last, after a general discussion, we will conclude about our study and we will suggest some perspectives.

## Chapter 1. Bibliography

### 1.1. Atherothrombosis

Atherothrombosis is a formation of a blood clot within an artery because of atherosclerosis. It is a widespread disease, which is one of the leading causes of death worldwide with many serious complications such as heart attack, stroke, limb gangrene, and ischemia organ disease including dementia [5]. Atherosclerosis is a slow process that begins early in childhood and progresses asymptotically in adult life. In some people, the disease grows rapidly in the age of 30s but it does not become dangerous until they reach to the age of 50s or 60s [6].

Because the evolution of atherosclerosis is very slow (over decades), an early detection of this disease is very important to get accurate diagnosis and successful treatment. However, determining the reasons of the evolution of this disease is very challenging. It is widely admitted that atherosclerosis starts from the damages of the inner wall of the artery [7]. The reasons of the damages could be high amounts of lipids and cholesterol in the blood, high blood pressure, diabetes mellitus, obesity, and smoking, lack of physical activity, metabolic syndrome, mental stress and depression [8, 9, 10].

The schematic evolution of atherosclerosis up to atherothrombosis depicted in Figure 1.1 [11] begins when lipids such as cholesterol deposit in artery wall (fat streaks). Gradually fat streaks evolve into plaques which growth decreases the inner diameter of the artery. It is an extremely complex disease, where the inflammation of the artery wall is the main activator leading the formation of a diseased area, namely the necrotic core, made of lipids, cells and cellular debris located beneath the endothelium [12, 13, 14, 11]. As blood flows make stress forces to the surface of the plaque, someday the plaque may break up, and thrombosis occurs. Thrombosis can limit or completely stop the blood flow to part of downstream tissues causing heart attack or stroke in the case of heart or brain respectively. Therefore, the treatment of atherothrombosis and the prevention of thrombosis are very important. For this purpose, the disease must be detected as early as possible. Nowadays, this is possible thanks to the development of clinical imaging techniques such as X-ray imaging and Magnetic resonance imaging [15]. However, if functional images can be

obtained, there is a need for molecular images which would highlight the biological processes implicated in the progression of the disease.

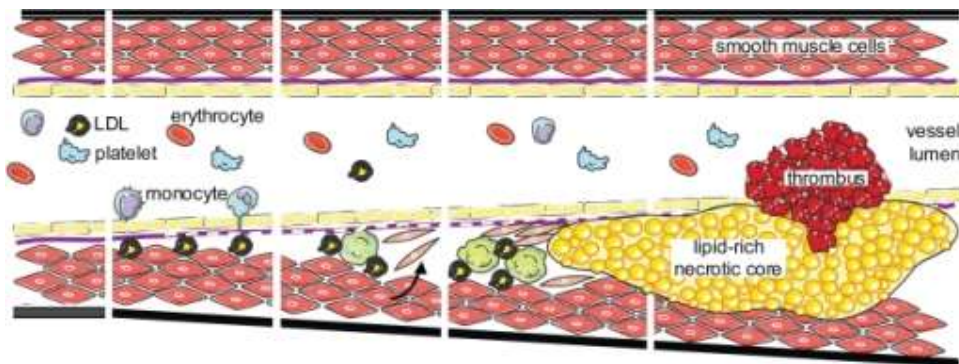


*Figure 1.1. The development of atherosclerosis up to atherothrombosis. The evolution of the process is depicted from the left to the right, from the very beginning (early fat streaks formation) to the rupture of the atherosclerotic plaque and the thrombotic event.*

## **1.2. Platelets and atherothrombosis**

When the atherosclerotic vessel is ruptured, thrombogenic substances within the necrotic core are exposed to the blood and platelets contribute to the pathophysiologic process via adhesion, activation and aggregation stages [16]. At a cellular level, phenotypical and morphological modifications of vascular cells are observed early in atherosclerosis [17, 18]. Platelets represent a major link between inflammation, thrombosis and atherogenesis [19, 20]. Beside, activated vascular cells overexpress membrane glycoproteins, in particular lectins, such as E-selectin, L-selectin and P-selectin (E, L and P stand for endothelial, leucocyte and platelet respectively). These are glycoconjugates which carbohydrate moieties play a critical role such as cell-cell interactions, cell growth, lymphocytes trafficking, thrombosis, inflammation, host defence or cancer metastasis [21, 22]. P-selectin, overexpressed on activated platelets, is recognized by a natural ligand PSGL-1 (P-selectin glycoprotein ligand-1) expressed by lymphocytes via the tetrasaccharide sialyl LewisX [23]. Structural features of sialyl LewisX are essential for the recognition of PSGL-1: the hydroxyls of L-fucosyl and D-galactosyl, carboxylic group of sialic acid [24], and sulfated tyrosines in the protein backbone [25, 26].

Fucoidan, heparin and dextran sulfate are sulfated polysaccharides which bind to P-selectin [27, 28, 29, 30] mimicking the interaction with PSGL-1. Low molecular weight fucoidan was formerly demonstrated to be of potential interest for revascularization in cardiovascular diseases [31, 32, 33] and found as the most efficient glycosidic ligand of P-

selectin in purified system and in human whole blood experiments [27, 34, 35, 36, 37]. The large amount of P-selectin in platelet-rich thrombi formed after atherosclerotic plaque rupture or erosion makes it a good target for fucoidan.

In this context, P-selectin appears as a good candidate target for the diagnosis of atherothrombosis and a contrast agent able to bind to P-selectin, i.e. vectorised by fucoidan to activated platelets, would efficiently enhance the detection of early thrombus formation.

### **1.3. Medical imaging modalities**

Medical imaging refers to several different technologies that are used to view the human body in order to diagnose, monitor, or treat medical conditions. Each type of technology gives specific information about the area of the body being studied or treated, related to a possible disease, injury, or the effectiveness of a medical treatment [15, 38]. Depending on the desired diagnostic information, the body can be observed by the following common techniques:

#### **1.3.1. X-ray projection imaging**

X-ray imaging is one of the first medical imaging modality. It found its way into medical practice shortly after the discovery of X-rays in 1895 by Wilhelm Röntgen, a German professor of physics. Today X-ray imaging is still one of the most commonly used forms of medical imaging. Because it became a big industry, equipment is relatively inexpensive and years of software improvements lead to a fast imaging procedure.

X-rays are created by bombarding a tungsten target with high-energy electrons inside an X-ray tube. When imaging with X-rays, the X-ray beam passes through the body. On its way through the body, parts of the energy of the X-ray beam are absorbed. The denser the tissues, the more X-rays are attenuated. For example, X-rays are attenuated more by dense bone than by soft lung tissue. On the opposite side of the body, detectors or a film capture the attenuated X-rays and a 2D image is produced.

#### **1.3.2. Computed tomography**

In 1979 G.N. Hounsfield and A.M. Cormack were awarded the Nobel Prize in Physiology or Medicine for the invention of computed tomography (CT). This technique uses computers to combine many X-rays slices to reconstruct a two- or three-dimensional

absorber map. Furthermore, the contrast of the computed image is software-enhanced and is much higher than that of a simple X-Ray projection imaging system [39].

Hounsfield's original CT scan prototype took several hours to acquire one single slice of image data and more than 24 hours to reconstruct this data into an image [40]. Today, many advances have been made in contrast, image quality, spatial resolution, and acquisition time. The modern clinical CT scanners can produce a 2D cross-sectional image in less than a second and reconstruct the image instantly – i.e., during the time the patient stays in the machine. Spatial resolution can be as low as 100  $\mu\text{m}$  in-plane. However, clinical CT scanners are expensive, ranging in the millions of dollars, preventing a widespread adoption [15, p. 37].

### **1.3.3. Nuclear imaging**

Nuclear imaging uses small amounts of isotopes called radiotracers that are typically injected into the bloodstream, inhaled or swallowed. Gamma-rays from the radiotracer are detected by a special camera and computed images of the distribution of radiotracers inside the body are obtained.

Three-dimensional reconstruction technologies in nuclear imaging are single-photon emission computed tomography (SPECT), or positron emission tomography (PET). Both methods have a significantly lower resolution than CT with voxel sizes not much smaller than 1  $\text{cm}^3$ .

In many centers, nuclear medicine images can be superimposed on CT or magnetic resonance imaging (MRI) images to produce special views, a practice known as image fusion or co-registration. These views allow the information from two different exams to be correlated and interpreted on one image, leading to more precise information and accurate diagnoses [15].

### **1.3.4. Ultrasound imaging**

Ultrasound imaging uses high-frequency sound for creating pictures of the inside of the body. The high-frequency (MHz) sound waves generated by a probe propagates into the body. The transducer collects echo of the sounds and a computer then uses those data to create an image. The depth of an echogenic object can be determined by the travel time of

the echo. The intensity of image relies on the intensity of the echo. The data is instantly processed and displayed by a computer.

Because ultrasound machines are cost-effective and of small size, they are widely used in hospitals or in physicians' offices. However, an ultrasound exam requires the presence of an experienced operator to adjust various parameters for optimum contrast, and ultrasound images usually require an experienced operator to interpret the image [15]. For standard clinical ultrasound, sound wave frequencies cover a wide range (3 – 40 MHz) and yield spatial resolution of 0.1 to 1 mm. The higher resolution of 0.015 to 0.02 mm has been achieved with ultrasound frequency of 100 MHz. However, the high frequency ultrasound is strongly attenuated in biological tissues. Therefore, the imaging depth is only a few millimetres [41, 42].

### **1.3.5. Magnetic resonance imaging**

Magnetic resonance imaging (MRI) is used in radiology to form pictures of the anatomy and the physiological processes of the body. Using strong magnetic fields, radio waves, and field gradients, MRI scanners can generate images of the organs in the body. MRI does not involve ionizing radiations, so it is a lot safer for operator and the studied patients except for people with irremovable metal implants because of eddy currents in conductors. MRI is based on nuclear magnetic resonance (NMR) in which certain atomic nuclei such as hydrogen atoms are able to absorb and emit radio frequency energy when placed in an external magnetic field. Hydrogen atoms exist naturally in all of biological organisms, particularly in water and fat. For this reason, MRI can image the whole body [43].

MRI requires a very strong and uniform magnetic field. The field strength of the superconducting magnets used in commercial MRI systems is between 0.2 and 7 Tesla. The world's currently strongest MRI Machine (21.1 T) is in Florida, USA [44].

### **1.3.6. Optical imaging**

Optical imaging is the use of light to study images of organs and tissues as well as smaller structures, including cells and even molecules. Images are generated by using light range from ultraviolet to near infrared. Many techniques have been developed for optical imaging:

**Fluorescence imaging:** As its name says it, fluorescence imaging uses fluorescence (fast emission) and phosphorescence (longer times) to study properties of organic or inorganic substances. When materials absorb light or other electromagnetic radiation, the materials may emit light back. Excited atoms or molecules in the material may return to their ground state through a radiative path. Normally, light isn't the sole component of the deexcitation path and thus the wavelength of emission light is longer than that of excitation light. Shorter wavelength can be generated if more than one photon contributed to the molecule's excitation. Some optical filters can, and frequently should, be added to block excitation light: as fluorescence has usually a low efficiency, excitation wavelength scattering may be too intense. The emitted fluorescence can be recorded by a detector for imaging. Fluorescence imaging can be used to detect molecules at small concentrations with a good signal-to-noise ratio if nothing else emits anything in the same wavelength range. A basic fluorescence imaging system is simple; however, a lot of complicated designs have been made to get better resolution of the fluorescent images, such as confocal microscopy and super resolution microscopy [45, 46, 47, 48].

**Second harmonic imaging:** in this technique, a high power and very short pulsed laser (femtosecond or picosecond) is focused into the sample. Ti-Sapphire (TiSa) lasers are frequently used for this application. The pulse width of Ti-Sapphire laser is between 10 fs to a few ps, with a possible spectral tuning range of  $\approx 650$  nm to 1100 nm [49]. These wavelengths penetrate deeply inside biological tissues, and short pulses give a very high light intensity while keeping the average power low enough. Commercially available TiSa lasers are now reliable and they can be operated very easily. This technique is based on the optical effect of second harmonic generation (SHG), whereby laser light passing through molecules with a non-centrosymmetric structure (ie with no centre of symmetry) leads to the generation of light at exactly half the wavelength of the incident light. Some well-ordered biological materials such as collagen, muscle myosin and microtubules can be imaged in this way without the need for additional labelling [50, 51]. By combining SHG with a confocal microscopy, one can obtain three dimensional images of biological tissues [52, 53].

**Optical coherence tomography:** Optical coherence tomography (OCT) is a technique for obtaining sub-surface images such as diseased tissue just below the skin. OCT uses low-

coherence interferometry, typically Michelson type, to produce a two-dimensional image of optical scattering from internal tissue microstructures in a way that is analogous to ultrasonic pulse-echo imaging. OCT is sensitive to scattering, thus it is mostly useful for tissues which aren't too optically dense. Tomographic imaging is demonstrated *in vivo* in the peripapillary area of the retina examination [54, 55, 56]. Light in an OCT system is broken into two arms as we expect in a Michelson interferometer: a sample arm (containing the item of interest) and a reference arm (usually a mirror). The combination of reflected light from the sample arm and reference light from the reference arm gives rise to an interference pattern, but only if light from both arms have travelled the "same" optical distance ("same" meaning a difference smaller than a coherence length). By scanning the mirror in the reference arm, the length of reference arm is changed. Areas of the sample that reflect back a lot of light will create greater interference than areas that don't. Any light that is outside the short coherence length will not interfere. By analyzing interference pattern, a reflectivity profile of the sample can be obtained [57].

**Photoacoustic imaging:** During photoacoustic imaging, high-repetition-rate laser pulses are delivered into biological tissues. A part of laser energy is absorbed and converted into heat, leading to transient thermoelastic expansion, and generating ultrasounds. The generated ultrasonic waves are detected by ultrasonic transducers and then analysed to produce images. Since deposited optical energy is, by definition, a function of the absorption coefficient, this is a way get a volume image of the absorption coefficient. The oxygenated or not oxygenated hemoglobin is the main absorber in the near infrared region. This makes this technique useful for medical purposes.

### 1.3.7. Conclusions

All of the medical imaging methods (X-ray projection imaging, computed tomography nuclear imaging, nuclear imaging, ultrasound imaging, magnetic resonance imaging and optical imaging) are used very commonly. However, all of them have some drawbacks. The X-ray projection imaging, computed tomography nuclear imaging and nuclear imaging (scintigraphy) are rather dangerous for patients who undergo repetitive examinations. The ultrasound imaging is safe but its resolution is not good enough. MRI is a good candidate for atherothrombosis detection because of it is safe and it offers a good tissue resolution. Then, optical imaging can be used to study finer structures of diseased areas with cell

resolution. We compare all of medical imaging method with their main advantages and drawbacks in Table 1.1 [58, 59, 60].

*Table 1.1. Comparison of medical imaging methods*

Types	Resolution	Sensitivity	Advantages	Drawbacks
X-ray	100 $\mu\text{m}$	0.16	Cheap, fast	Danger
CT	100 $\mu\text{m}$	0.67	3D imaging	Danger, expensive
Nuclear	1 cm	0.60	3D imaging	Danger
MR	100 $\mu\text{m}$	0.81	Safe	Expensive
Ultrasound	100 $\mu\text{m}$	0.55	Safe, cheap	Difficult in use
Optical	0.2-10 $\mu\text{m}$	0.94	Safe, cheap	Invasive

#### 1.4. MRI contrast agent

MRI contrast agents are used to improve the visibility of internal body structures studied in MRI. Their main effect is the shortening of the longitudinal or transversal relaxation times,  $T_1$  or  $T_2$  respectively, of the hydrogen nuclei of neighbour water molecules. The capability of shortening the  $T_1$  and  $T_2$  relaxation times is described by the term "relaxivity". The relaxivities associated to the longitudinal and transversal relaxation rates,  $1/T_1$  and  $1/T_2$ , are denoted by  $r_1$  and  $r_2$ .

##### 1.4.1. Relaxivity

MRI contrast agents are characterized by their relaxivity. The relaxivity of an MRI contrast agent shows the change of relaxation rates as a function of solution concentration  $[C]$ . There are two corresponding relaxivities,  $r_1$  and  $r_2$  which are calculated as equation 1.1 and 1.2.

$$\frac{1}{T_1} = r_1 \times [C] \quad (1.1)$$

$$\frac{1}{T_2} = r_2 \times [C] \quad (1.2)$$

where:  $T_1$  and  $T_2$  are relaxation rates (s),  
 $[C]$  is the concentration of solution (mM),  
 $r_1$  and  $r_2$  are relaxivities ( $\text{mM}^{-1}\text{s}^{-1}$ ).

The relaxation rates of a MRI contrast agent in solution are obtained by linear fitting relaxation rates ( $1/T_1$ ) and ( $1/T_2$ ) versus different concentrations. The slopes of the lines present  $r_1$  and  $r_2$  [61, 62, 63].

#### 1.4.2. $T_1$ contrast agent

Because of high paramagnetic moment, Gadolinium ion ( $\text{Gd}^{3+}$ ) is the most common  $T_1$  contrast agent used in clinical applications. However, like most free ion metals, the free ion  $\text{Gd}^{3+}$  is toxic for living tissue. Therefore, in order to use it as a contrast agent, gadolinium ions need to be grafted on a suitable ligand to form a nontoxic complex. The relaxation mechanism of a  $T_1$  contrast agent is described by the Solomon-Bloembergen-Morgen (SBM) theory [64, 65, 66]. The relaxation is mainly due to the interaction between a  $\text{Gd}^{3+}$  ion and nearby water molecules, which directly coordinate with the  $\text{Gd}^{3+}$  ion. This interaction is characterized by the exchange correlation time  $\tau_m$ . In the complex,  $\text{Gd}^{3+}$  usually has one directed coordination with a water molecule. The rotation of the complex is also important: The rotation frequency of Gd complexes is faster than the Larmor frequency. The effect of the complex rotation is characterized by the rotational correlation time  $\tau_r$ . The slowing down of complexes close to the Larmor frequency improves the relaxation. One way to improve this relaxation is to link many Gd chelates on a single macromolecule. The consequences are both the longer rotational correlation time and the local increase in the concentration of  $\text{Gd}^{3+}$  ions [67].

#### 1.4.3. $T_2$ contrast agent

Magnetite ( $\text{Fe}_3\text{O}_4$ ) or maghemite ( $\gamma\text{-Fe}_2\text{O}_3$ ) NPs are superparamagnetic contrast agents. They are the most effective  $T_2$  contrast agents [68, 69]. With their size ranging from 4 nm to 50 nm, the superparamagnetic agents contain thousands of paramagnetic Fe ions ( $\text{Fe}^{2+}$  and/or  $\text{Fe}^{3+}$ ). Therefore, exposed to an external magnetic field, superparamagnetic agents induce strong local fields, which speed up the dephasing of the neighboring water protons [70], i.e. making a shortening of  $T_2$  and an increment of  $r_2$ . Depending on their size, crystal structure and coating, the superparamagnetic agents are classified into superparamagnetic

iron oxide particles (SPIO), ultra-small superparamagnetic iron oxide particles (USPIO), very small superparamagnetic iron oxide particles (VSOP), monocrystalline iron oxide particles (MION) and cross-linked iron oxide particles (CLIO) [71, 72, 73, 74]. SPIO and USPIO contrast agents have been successfully used for MR images enhancement [75, 76].

### 1.5. Zinc oxide

Zinc oxide is widely used as an industrial additive to produce many materials such as rubbers, plastics, ceramics, concrete, glass, lubricants, paints, ointments, adhesives, sealants, pigments, foods, batteries, laser diodes, light emitting diodes, spintronics, solar cells, sensors and actuators [77].

Zinc oxide usually crystallizes in three different forms: hexagonal wurtzite, cubic zinc blende and cubic rocksalt. The ZnO wurtzite, which is the most common structure of ZnO [78], has the highest thermodynamic stability among the three above structures.

Zinc oxide is a direct gap semiconductor with  $E_g = 3.4$  eV. It has many excellent properties such as a good transparency, high electron mobility, wide band gap, and good room-temperature luminescence [79]. ZnO produces UV emission around 370 nm and visible emission of around 510 nm [80, 81, 82]. For the visible emission, many point defects have been suggested, including oxygen vacancies, interstitial oxygen, antisite oxygen, zinc vacancies, zinc interstitials, and surface states [83]. There are two popular mechanisms, which explain this visible emission: the recombination of an electron from the conduction band (CB) with a hole in a deep trap [84] and the recombination of holes from the valence band with a deeply trapped electron [85].

Semiconductor quantum dots (QD) have been used for biological imaging since 1998 [86, 87]. However, the traditional QDs, like CdSe and CdTe, are toxic. Cytotoxicity of quantum dots used for in vitro cellular labelling have been investigated [88, 89, 90]. In contrast to QD, zinc oxide is categorized as a non-toxic material because it does not cause skin and eye irritation and there is no evidence of carcinogenicity, genotoxicity and reproduction toxicity in humans [91]. Luminescent ZnO NPs, due to their special advantages, such as bright emission, low cost, and good biocompatibility, is a better candidate in biological applications [92, 93]. Although the ZnO NPs have been used for cell imaging successfully [94, 95, 96], we still have to overcome many challenges. First, because

of their broad emission band, the fluorescence spectra overlap the autofluorescence of biological cells [97]. Secondly, UV light is used for excitation because ZnO is a wide-bandgap semiconductor. However, UV light is not suitable for deep tissue imaging *in vivo* because cells strongly absorb light in UV band. In addition, UV light kills cells, tissues, and live animals, damaging their DNA [98, 99]. Therefore, multi-photon or fluorescence lifetime imaging may solve the above problems but add complexity to the setup.

### 1.6. Bimodal MRI/optical contrast agents

MRI contrast agents, like all contrast agents, are used for image enhancements. Many studies on human and animals have been performed using MRI. The method has many advantages, however, it has some drawbacks too. The first one is its spatial resolution. The spatial resolution of a commercial MRI machine is around one hundred micrometres [100, 101, 102] and this resolution requires a long acquisition time. This limited resolution is not suitable for analysing the distribution of the MRI agents in small volumes such as a single cell or the layers of a small artery wall. The resolution of MRI is far worse than the resolution of an optical microscopy (~100 times). Many efforts to synthesize fluorescent MRI agents were proposed in order to advance the art. For example, fluorophores linked with MRI agents have been synthesized [103, 104]. However, autofluorescence of biological tissues and the main fluorophores used for agents have overlapped wavelengths bands, making it sometimes difficult to interpret the images. Hence, some fluorescent markers emitting in the near infrared region have been studied, in order to stand out of the autofluorescence of the tissues [105]. Another approach is to use long fluorescence lifetime emission by the use of lanthanide complexes. Europium and terbium, lanthanide compounds have been employed for forty years in analytical biochemistry [106, 107] with several advantages compared to purely organic fluorophores such as a very long luminescence decay (some hundred microseconds to some milliseconds), better photostability, narrow emission lines and large Stokes shift [108, 109]. The fluorescent emission lies in the visible domain: green light for terbium and red light for europium [110]. Within a time resolved microscope system, this emission can be easily discriminated from the autofluorescence noise. Gadolinium, europium and terbium have close physicochemical properties. By replacing  $Gd^{3+}$  ions with  $Eu^{3+}$  or  $Tb^{3+}$  ions, the same agents could possibly be used in MRI and in a time-gated fluorescence microscopy in the visible band. Unfortunately, the organic

fluorophores and lanthanide complexes are toxic needing a complexing chemical structure to protect the organism. Recently, a macromolecular complex bearing both terbium and gadolinium ions have been used to image thrombosis in a rat model [111]. However, these structures are not easy-to-handle.

In recent years, nanoparticles (NPs) containing iron and zinc oxide showing both magnetic and fluorescent properties have attracted significant research interests because of their potential applications. NPs base on ZnO have been synthesized by many ways. The most popular approach is polyol method. Different structures such as core@shell systems based on ZnO and superparamagnetic iron oxide like ZnO@Fe<sub>3</sub>O<sub>4</sub> [112] and Fe<sub>3</sub>O<sub>4</sub>@ZnO [113, 114], ZnO nanorods decorated with  $\gamma$ -Fe<sub>2</sub>O<sub>3</sub> have been proposed [2]. ZnO-based nanocrystals doped with up to 25 wt% Fe synthesized by the polyol method was also reported with narrow size distribution (17–21 nm) [3].

### **1.7. The biospecificity of contrast agents**

The response of the reticuloendothelial system (RES, mainly liver and spleen) to foreign particles is influenced by particle size, charge, shape and the nature of the surface. Particles less than 5 nm are rapidly cleared from the circulation through extravasation or renal clearance [115, 116]. As particle size increases, accumulation occurs primarily in the liver, the spleen and the bone marrow. The first process that occurs when NPs are exposed to plasma is a quick and massive non-specific protein adsorption which results in the formation of a protein corona around the material [117, 118]. Among the adsorbed proteins, opsonins trigger the complement activation and a signalling cascade leading in phagocytosis via RES. Eventually this results in non-ideal biodistribution and unpredictable pharmacokinetics of the NPs. This phenomenon is considerably attenuated when the average hydrodynamic diameter of the NPs does not exceed a hundred nanometers and when their surface is coated with low fouling polymers (e.g. polyethylene glycol (PEG)) which ensure the formation of a repulsive hydration shell limiting the protein adsorption [119]. In the majority of cases, NPs achieve their effects through passive targeting, which relies on non-specific accumulation in diseased tissue, usually tumours. Within the tumour microenvironment, the endothelial paving of the vessels is disjoint allowing the paracellular diffusion of NPs whose dimensions do not allow the passage of a healthy endothelium. This permeability of blood vessels in combination with poor lymphatic drainage or transport

leads to NPs accumulation within the diseased area: this phenomenon is defined as the Enhanced Permeability and Retention (EPR) effect.

In our research, we adopt polyol method to synthesize NPs, because the size of synthesized NPs is less than 100 nm. This small size will limit their catch by the immune system, allowing a longer blood circulation time.

### **1.8. Strategy of the project**

In this project, we develop imaging tools for the observation of arterial wall thrombus at cellular and molecular scales for better understanding of processes involved in the development of thrombotic diseases. This work is divided in two main parts: the preparation of biospecific nanoprobes endowed with magnetic and optical relevant properties, and the development of optical imaging methods to effectively recover injected nanoparticles in tissue sections, to interpret their distribution and location in relation to the pathological environment. It is not any type of nanoparticle that can be used for this objective. These must comply with precise specifications: (i) the materials used must lead to nanostructures with relevant magnetic and optical properties; for this study we have prepared nanoparticles based on Zn(Fe)O crystals, (ii) the size of the colloids formed by the inorganic core and its hydrophilic hemocompatible coating must be as small as possible at the nanometric scale to limit an early elimination once injected into the blood; (iii) the colloids must be stable in a physiological medium for the duration of their use; (iii) the method of preparation must efficiently provide simple nanostructures.

We synthesized our NPs without water using an azeotropic polyol synthesis method with the objective to study the role of water over the synthesis. Surprisingly, the absence of water led to smaller NPs with a tighter size distribution than with water and in higher yields. We have thus focused our works on the preparation of the NPs with this novel method. The nanocrystals have been coated with hydrophilic polymers compatible with use in a murine model of atherothrombosis, in particular with a polysaccharide recognized as a ligand specific for the thrombus. MR imaging was performed in a rat model of atherothrombosis and histological sections of tissues were examined with dedicated optical microscope setup. In a first step, we have explored in vitro optical imaging strategies using as-prepared nanosystems. As many techniques were available, some of them being quite sophisticated and expensive, we have chosen to keep the experiments as simple and straightforward as

possible. We added complexity gradually as needed. Then at the end of this work, when we built enough confidence in the setup, we applied the different optical imaging modalities to histological slices.

## Chapter 2. Chemistry

During this study, we prepared a large number of samples. The specifications explained previously led us to focus on a novel polyol strategy. To help the reader to understand our entire approach, we have chosen to focus on the main results obtained with nanoparticles prepared under azeotropic conditions. Other avenues have been explored, which are briefly presented as appendixes to the main document. Indeed, only the polyol azeotropic method has made it possible to quantitatively and efficiently obtain nanocrystals of controlled composition in zinc and iron, which made it possible to carry out studies in MRI and optical microscopy. The novelty of the azeotropic synthesis led us to gather our results for a publication in *Chemical Communications* which will be submitted soon.

Thus, we have prepared Zn(Fe)O NPs with different Fe ratios ( $R_{Fe} = Fe/(Zn+Fe) = 0, 0.05, 0.10, 0.15, 0.20, 0.35$  and  $0.50$ ) from azeotropic distillation with toluene. We investigated the morphology, crystallinity, and magnetic properties of Zn(Fe)O NPs using a transmission electron microscope, X-ray diffraction, and a vibrating sample magnetometer. We coated our NPs with carboxymethyl pullulan, polyethylene glycol, fucoidan, and carboxymethyl dextran (CMD), but only the two latter coatings are presented in this chapter since the corresponding NPs could be used for animal experiments. Physicochemical properties of the colloids have been determined as well as magnetic and optical capacities.

The following notations will be applied in the following:

+ Bare NPs obtained in diethylene glycol with  $R_{Fe} = X$  will be noted:  $R_{Fe, i} = X$ .

(ex:  $R_{Fe, i} = 0.50$ )

+ Fucoidan-coated or CMD coated NPs with  $R_{Fe} = X$  will be noted: fuco- $X$  or CMD- $X$ .

(ex: fuco-0.50)

## 2.1. Materials and methods

### 2.1.1. Synthesis of NPs

#### Chemicals

Zinc acetate dehydrate (98%, Sigma Aldrich) and iron II acetate (97%, Strem Chemicals) were used as precursors. Diethylene glycol (99%, Alfa Aesar), polyethylene glycol (98%, Alfa Aesar) and toluene (99%, Alfa Aesar) were used as solvent. Carboxymethyl dextran was purchased from Sigma Aldrich (MW = 10-20 KDa, and CM content = 1.1-1.5 mmol CM/g). Carboxymethyl pullulan was prepared from pullulan (Hayashibara, Japan) as described in the Appendix F. Low molecular weight fucoidan from the brown seaweed *Ascophyllum nodosum* was purchased from Algues & Mer (Ile d'Ouessant, France). Fucose and sulfate contents were  $30.1 \pm 0.6$  and  $26.5 \pm 0.5$  respectively (%w/w) with Mn = 7,200 g/mol and Mw = 10,100 g/mol. Purified water used for the experiments was obtained by ion-exchange from running tap water (Millipore, USA).

#### Preparation of bare NPs

We used the following protocol to prepare the nanoparticles used later in animal experiments. The variants of this protocol that were made with other conditions, especially in the presence of water, are presented in the Appendix D. In absence of water NPs we have obtained smaller NPs in higher yields and with a tighter size distribution. Zinc acetate and iron II acetate were used as precursors. Diethylene glycol (DEG), propylene glycol (PG) and toluene were used as solvents.

0.02 mol of zinc acetate and iron II acetate with different Fe/Zn ratio (mol/mol) ( $R_{Fe} = Fe/(Zn+Fe) = 0, 0.05, 0.1, 0.15, 0.20, 0.35$  and  $0.50$ ) were dried at 60°C under vacuum overnight. Then salts were dispersed in a mixture of 80 ml of DEG (or 80 ml of PG) and 120 ml of toluene, in a three necks 500 mL round bottom flask and heated under nitrogen and a gentle mechanical stirring. The flask was connected to a Dean-Stark apparatus for entrapping water azeotropically (Figure 2.1). For 1 h, water (a few mL) and toluene (120 mL) were successively collected by reflux into the Dean-Stark trap and fully eliminated through a Teflon tap. During this process, the temperature did not exceed 110°C. Collection was stopped when the temperature started to rise again reaching 240°C (or 180°C with PG). The mixture was heated at 240°C (or 187°C with PG) for 4 additional hours (or 2 additional

hours with PG). After cooling down to room temperature, NPs were quantitatively collected by centrifugation (8000 RPM, 15 minutes) and washed 2 times with acetone, 2 times with ethanol and kept as a concentrated suspension in absolute ethanol.

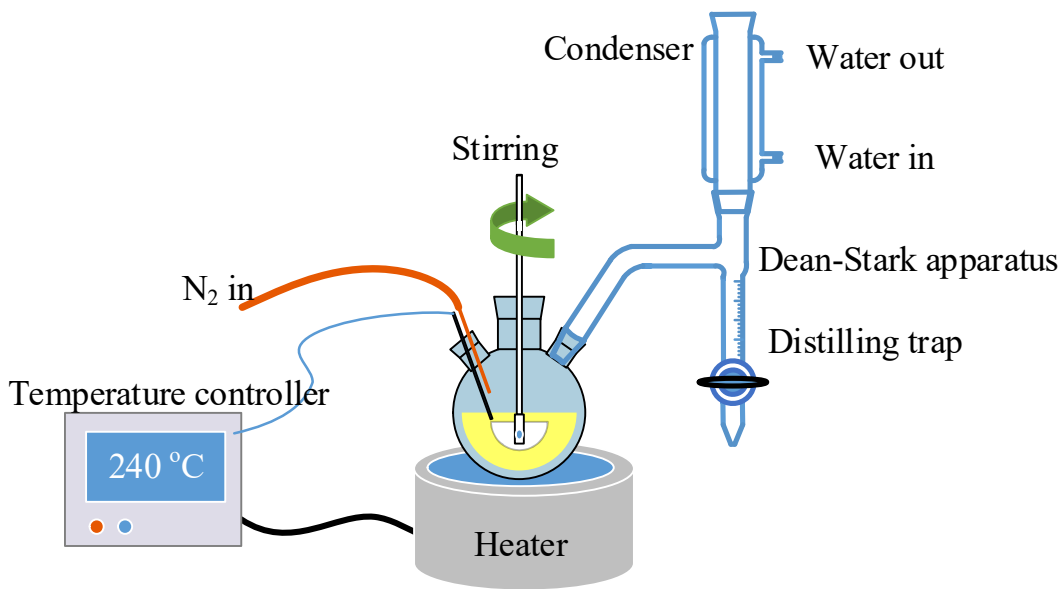


Figure 2.1. Experimental setup for synthesis of NPs with Dean-Stark apparatus.

### 2.1.2. Iron concentration measurement by UV-visible spectrophotometry

The iron concentration was measured as follows: 10  $\mu\text{L}$  of NPs suspended in water were mixed with 100  $\mu\text{l}$  of  $\text{HNO}_3$  7 M and 100  $\mu\text{l}$  of  $\text{H}_2\text{O}_2$  20%. The mixture was heated to 80°C for 2 hours. After cooling to room temperature, 1 mL of water and 100  $\mu\text{L}$  of KSCN 2 M were added to the tube just before each measurement. The iron concentration of diluted solution was determined by absorption spectra at 477 nm with a JASCO V-630 UV-visible spectrophotometer (JASCO, Germany). The concentration of Fe ( $C_{Fe}$ ) in diluted solution is calculated by the equation 2.1.

$$C_{Fe} = \frac{D+0.0055}{7322.377} \text{ (mol/l)} \quad (2.1)$$

where:  $D$  is the absorption at 477 nm.

Then the concentration of Fe in the original suspension is calculated from the value of  $C_{Fe}$  and the dilution factors.

### 2.1.3. Iron and zinc concentration measurement by AAS

The chemical composition of the powders was obtained from suspension (0.5M) by atomic absorption spectroscopy (AAS) with a Perkin-Elmer Analyst 100 apparatus (Perkin-Elmer, USA) after degradation of the nanocrystals in boiling HCl (35%).

### 2.1.4. Coatings

#### *Fucoidan coating*

3 mL of suspension were prepared as following: 1 mL of bare NPs ( $R_{Fe} = 0.05, 0.15, 0.35, 0.50$ ) in HCl  $10^{-2}M$  ( $[Fe] = 0.12 \text{ mol/L}$ ) was diluted in 14 ml of HCl  $10^{-2}M$  (pH=2) and sonicated for 30 minutes (SA). Then 4 mg of fucoidan were dissolved in 15 ml of water (SB). SA and SB were mixed and gently shaken at room temperature for 2 hours. The fucoidan coated NPs were collected by centrifugation (7300 RPM, 30 minutes) and resuspended in 3 ml solution of glucose 5% (w/w). The pH of final suspension was adjusted to 7.2 and 7.5 with a few drops of diluted NaOH. The suspension was split into 6 tubes of 0.5 ml each which were kept in the dark at  $-20^{\circ}C$ .

#### *Polyethylene glycol coating*

2 mL of suspension were prepared as following: 0.667 mL of  $R_{Fe, i} = 0.50$  NPs in HCl  $10^{-2}M$  ( $[Fe] = 0.12 \text{ mol/L}$ ) was diluted in 3 ml of HCl  $10^{-2} M$  (pH=2) and sonicated for 30 minutes (SA). Then 50 mg Polyethylene glycol (PEG) was strongly sonicated in 10 ml of HCl  $10^{-2} M$  (pH=2) for 2 hours (SB).

SA was added drop by drop into SB under stirring. After stirring for 2 hours at room temperature, the pH of the suspension was adjusted to 7 by adding a few drops of NaOH 0.1 M. The PEG-NPs then were washed to remove ungrafted PEG by filtration (filtration device with 30 kDa cut-off membrane) at 3900 RPM for 15 minutes. For each washing water was filled-up to 10 ml and the solution was drained out of filter and sonicated for 20 seconds. The process was repeated 5 times. Glucose solution 5% (w/w) was used for the last washing by centrifugation (3900 RPM, 30 minutes). Finally, PEG-NPs were resuspended in 2 ml solution of glucose 5% (w/w). The pH of final suspension was adjusted between 7.2 and 7.5 with a few drops of diluted NaOH. The suspension was split into 4 tubes of 0.5 ml each which were kept in the dark at  $-20^{\circ}C$ .

### ***Carboxymethyl dextran coating***

2 mL of suspension were prepared as following: 667  $\mu\text{L}$  of  $R_{\text{Fe}, i} = 0.50$  NPs in  $\text{HCl } 10^{-2}\text{M}$  ( $[\text{Fe}] = 0.12 \text{ mol/L}$ ) were diluted in 10 ml of  $\text{HCl } 10^{-2} \text{ M}$  ( $\text{pH}=2$ ) and sonicated for 30 minutes (SA). Then 3.5 mg Carboxymethyl dextran sodium salt (CMD) (MW= 10-20 kDa) was dissolved in 10 ml of water (SB). SA and SB were mixed and gently shaken at room temperature for 2 hours. The CMD-coated NPs were collected by centrifugation (7300 RPM, 30 minutes) and resuspended in 2 ml solution of glucose 5% (w/w). SA and SB were mixed and gently shaken at room temperature for 2 hours. Then, CMD-coated NPs were collected by centrifugation (7300 RPM, 30 minutes) and resuspended in 2 ml solution of glucose 5% (w/w). The pH of final suspension was adjusted between 7.2 and 7.5 with a few drops of diluted NaOH. The suspension was split into 4 tubes of 0.5 ml each which were kept in the dark at  $-20^{\circ}\text{C}$ .

### ***Carboxymethyl pullulan coating***

50 mg of  $R_{\text{Fe}, i} = 0.50$  NPs (average size is 4 nm), 80 mg of dimercaptosuccinic acid (DMSA) and 25 ml of absolute ethanol were sonicated for 30 minutes. DMSA-0.50 were washed 2 times with ethanol. Then DMSA-0.50 were resuspended in 8 ml of ethanol. The mixture of 160 mg of CMP in 16 ml of  $\text{HCl } 10^{-3} \text{ M}$  ( $\text{pH}=3.5$ ) and DMSA-0.50 in 8 ml of ethanol was shaken for 24 hours at room temperature for ligand exchange. CMP-0.50 were collected by centrifugation (8000 RPM, 15 minutes) and washed several times with pure water. Finally, CMP-0.50 were resuspended in 8 ml solution phosphate-buffered saline (PBS) and kept in the dark in a refrigerator at  $6^{\circ}\text{C}$ .

Note: the synthesis and the characterization of CMP are described in Appendix F.

### **2.1.5. Fucoïdan content**

The fucoïdan coating was evaluated by the amount of sulfate groups per gram of NPs [35]. Sulfate content was obtained by formation of methylene blue after acidic hydrolysis of the samples, reduction of sulfate as hydrogen sulphide, and formation of methylene blue from N,N-dimethyl phenylene diamine dihydrochloride in strong acidic medium in presence of ferric chloride. 100 to 200  $\mu\text{L}$  of the suspension of Fuco-0.50 were added to 5 mL a reducing mixture prepared with 100  $\mu\text{L}$  of concentrated hydriodic acid, 25  $\mu\text{L}$  of glacial acetic acid and 2.5 g of hypophosphorous acid. The mixture was refluxed for 20 min

through a water-cooled condenser under a stream of  $N_2$  ( $100 \text{ mL min}^{-1}$ ) which carried away evolved hydrogen sulphide ( $H_2S$ ). After bubbling through a gas-washing column (20 mL of tris buffer 0.1 M, pH 7.2),  $H_2S$  was trapped as zinc sulphide in 30 mL of a solution of zinc acetate prepared by diluting 5 mL of 0.50 M and sodium acetate 0.10M with 25 mL of deionized water. Eight mL of 16 mM ferric chloride in  $H_2SO_4$  0.1 M, and 2 mL of 3.7 mM N,N-dimethyl phenylene diamine dihydrochloride in  $H_2SO_4$  9 M were added to the zinc sulphide solution, and the final volume was adjusted to 50 mL with deionized water. The vial was maintained at room temperature under dark for 20 min and the absorption was measured at 665 nm with a UV-visible spectrophotometer (mc2, Safas, Monaco). The amount of sulphur was determined from a standard curve obtained with potassium sulfate solutions submitted to the overall process.

#### **2.1.6. Particle size analysis and isoelectric point analysis**

The hydrodynamic diameter of particles in PBS (0.5M Zn) and the zeta potentials were measured by dynamic light scattering (DLS), using a Zetasizer Nano S. Size (Malvern Instruments, UK) measurements range from 0.3 nm (diameter) to 10 microns. Zeta potential dependence on pH was obtained by measuring the zeta potential in aqueous solution by adjusting the pH value by the addition of HCl and NaOH (1 M).

For measurements, the folded capillary cell is filled up with 1 ml of NPs in PBS ( $C_{Fe} \sim 1 \text{ mM}$ ). The hydrodynamic diameter and the zeta potentials are measured at  $25^\circ\text{C}$ .

#### **2.1.7. UV-visible and fluorescence spectroscopy**

The absorption spectra were recorded by JASCO V-630 UV-visible spectrophotometer (JASCO, Germany). Fluorescence spectra were measured by FluoroMax Plus (HORIBA Scientific, Japan).

#### **2.1.8. FT-IR spectroscopy**

The mixture of 1 mg of NPs powder and 100 mg of potassium bromide (KBr) was grinded into fine powder. The powder then is left drying at  $70^\circ\text{C}$  overnight. Finally, the powder pressed by a hydraulic compressor with approximately 10-ton force made 13 mm pellets. All of the measurements were recorded by NICOLET 380 FT-IR (Thermofischer, France).

### **2.1.9. Magnetic properties**

The magnetic behavior of the as-synthesized nanoparticles was characterized at room temperature using a vibrating sample magnetometer, VSM (Quantum Design, USA). The VSM measures the magnetization by cycling the applied field from -30 kOe to +30 kOe, with a step rate of 100 Oe/s.

### **2.1.10. Relaxivity**

The relaxation rates of NPs in suspension are obtained by linear fitting relaxation rates ( $1/T_1$ ) and ( $1/T_2$ ) versus different Fe concentrations. The 500  $\mu$ l tubes were carefully filled up with colloidal NPs suspension ( $C_{Fe} = 0.0261, 0.0522, 0.0774, 0.113, 0.147, 0.303,$  and  $0.7$  mM or  $1.46, 2.93, 4.39, 6.32, 8.26, 17.0,$  and  $3.92$  mg Fe/L). All of the tubes were checked to confirm that there are no air bubbles remaining in the tubes. The relaxation times  $T_1$  and  $T_2$  were measured with the small animal 7T MRI Bruker Pharmascan (Bruker, Germany).

### **2.1.11. Transmission electron microscopy**

TEM images were taken on a JEOL JEM-ARM200F Cs-corrected Field Emission Transmission Electron Microscope (JEOL, USA). Samples were prepared by dropping of the colloidal suspension onto holey carbon-coated Cu grid.

### **2.1.12. X-ray diffraction**

The equipment used for these measurements is an INEL EQUINOX 1000 X-Ray diffractometer in asymmetric geometry (INEL, France). The X-Ray monochromatic incident beam (Co  $K_{\alpha 1} = 0.1788976$  nm radiation) makes an angle of around  $6^\circ$  with the sample. 2 crossed slits ( $0.15 \times 5 \text{ mm}^2$ ) are placed in trough the beam at 70mm before the sample. A continuous rotation of the sample (around the normal of the analysed face) is done during the acquisition time in order to reduce texture effects. Line profiles are collected on a curved linear detector ( $0^\circ$ - $115^\circ$ ) placed at 180mm from the sample. In order to characterize the different phases (lattice parameters, microstructures, % of phases ...) Rietveld refinements were performed using MAUD software (Material Analysis Using Diffraction) [120].

### 2.1.13. Thermogravimetric analysis

The average number of CMD, PEG and Fucoidan molecules per nanocrystal was measured by thermogravimetric analysis using a LabsSys evo TG-DTA-DSC 16000 device (Setaram Instrumentation, France). 15 mg of coated NPs was put in a furnace tube. The temperature of the furnace was controlled from 30°C to 1500°C.

## 2.2. Results and discussion

We synthesized the Zn(Fe)O NPs by polyol method with Fe ratio =  $R_{Fe}$  = 0, 0.05, 0.10, 0.15, 0.2, 0.35 and 0.50 (mol/mol). The advantages of using this method are the polar character and the high boiling point of the solvents, which makes it possible to solubilize a large number of metallic precursors and to activate efficiently the reactions [121, 122]. Anyway, NPs were synthesized by different ways (see Appendixes). Finally, we found that by using azeotropic distillation to remove water from the starting mixture, NPs were very small with a narrow size distribution. The Figure 2.1 presents a scheme of the system which was used.

It should be noted that as much as possible, the NPs have been maintained suspended in a liquid phase. Very small samples were dried only to estimate yields (always above 70% with the azeotropic method) and to perform some analyzes (such as XRD and TGA) requiring dried powders. The concentration of the suspensions was determined by chemical analysis. There were two reasons for this strategy: NPs in the dry state are very difficult to resuspend in liquids and their potential toxicity to the manipulator is limited in the liquid phase. However, the suspensions were most often unstable and few minutes of treatment with ultrasounds were needed before use (with some exceptions, in particular with coated NPs).

### 2.2.1. NPs synthesis in Propylene glycol

#### Chemical analysis

Chemical analysis was performed by atomic absorption to provide iron and zinc content. Measured  $R_{Fe}$  values increased with the initial amounts of salts but they were always lower than the starting ones.

Table 2.1. Chemical analysis of Fe in NPs synthesized in PG

$R_{Fe}$ initial (mol)	$R_{Fe}$ measured (mol)
$R_{Fe} = 0.05$	0.498
$R_{Fe} = 0.10$	0.0805
$R_{Fe} = 0.20$	0.181
$R_{Fe} = 0.50$	0.499

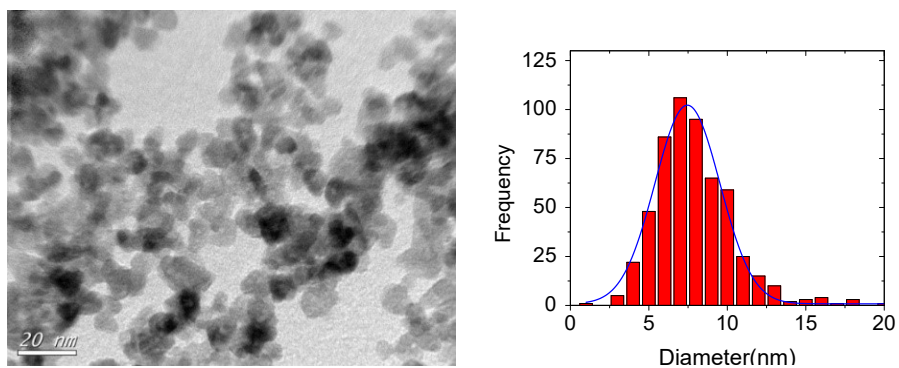
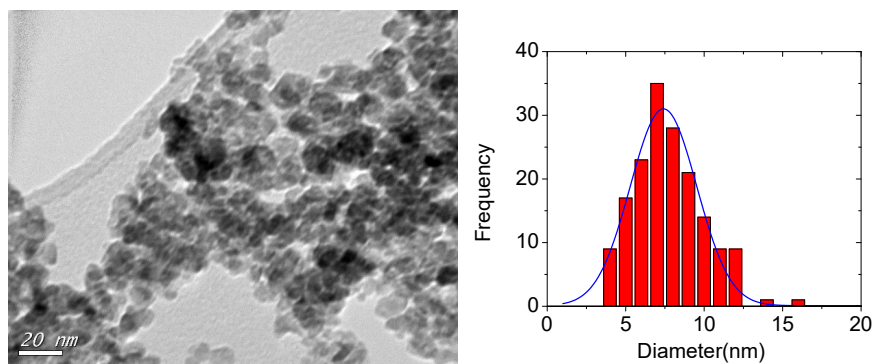
**TEM and XRD analyses**

Figure 2.2. TEM images and size distribution of bare ZnO NPs.

Figure 2.3. TEM images and size distribution of bare NPs with  $R_{Fe} = 0.2$ .

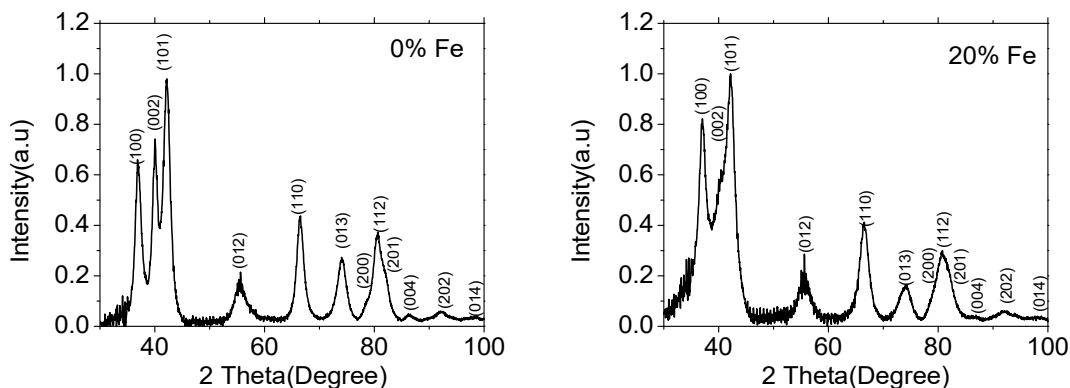


Figure 2.4. XRD diffractogram of bare ZnO (left) and  $R_{Fe} = 0.2$  (right) NPs.

In Figure 2.2 and Figure 2.3, the TEM images show that the mean size of bare ZnO and Zn(Fe)O  $R_{Fe} = 0.2$  is only about 7.5 nm with narrow size distribution.

The crystalline quality and phase purities of the prepared Zn(Fe)O samples synthesized in PG with azeotropic distillation were examined by powder XRD method (Figure 2.4). The crystalline sizes of all NPs samples were calculated using the highly intense peak by Scherrer's formula. It was found that all of the diffraction peaks are come from wurtzite ZnO phase. No other impurity peaks are detected indicating the purity of the synthesized samples. The calculated averaged crystalline size of NPs is around 6 nm which matches with results of TEM). The size of XRD are smaller than size TEM. So, there are amorphous layers outside the NPs.

### Magnetic properties

The magnetic properties of the  $R_{Fe} = 0.5$  NPs powder were determined at 5 K and 300 K using a vibrating sample magnetometer (VSM) in the applied field ranging from  $-70$  to  $+70$  kOe (Figure 2.5). Hysteresis plots show the variation of magnetization ( $M$ , emu/g) as a function of applied magnetic field ( $H$ , Oe). The weak magnetism confirms that, the NPs are wurtzite phase. Because of the weak magnetism, we did not consider NPs synthesized in PG for further works.

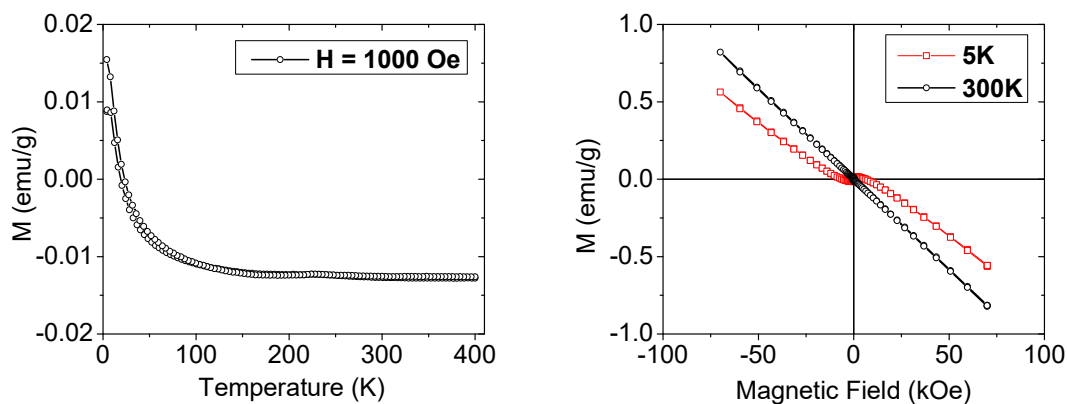


Figure 2.5. Magnetization ( $M$ ) versus temperature (left) and versus applied field ( $H$ ) at 5 K and 300 K (right) of  $R_{Fe} = 0.2$  NPs synthesized in PG.

### 2.2.2. NPs synthesis in diethylene glycol

#### Chemical analysis

Chemical analysis was performed by atomic absorption and UV-visible spectrometry, to provide iron and zinc content (Table 2.2).

Table 2.2. Chemical analysis of Fe in NPs synthesized in DEG with  $R_{Fe} = 0.05, 0.1, 0.15, 0.2, 0.35$  and  $0.50$ .

$R_{Fe}$ initial (mol)	$R_{Fe}$ measured (mol)
$R_{Fe, i} = 0.05^*$	0.064
$R_{Fe, i} = 0.1$	0.191
$R_{Fe, i} = 0.15^*$	0.179
$R_{Fe, i} = 0.2$	0.198
$R_{Fe, i} = 0.35^*$	0.461
$R_{Fe, i} = 0.50$	0.569

\* obtained by visible spectrometry (see Appendix N).

Measured  $R_{Fe}$  values increased with the initial amounts of salts and they were always higher than the initial ones.

### TEM and XRD analyses

#### *Bare NPs*

TEM and XRD analyses were performed and data are presented on Figure 2.6 and Figure 2.7. The TEM images were analysed manually using the graphical software *ImageJ* with measurement of about 200 NPs for each sample. Results are presented in Table 2.3.

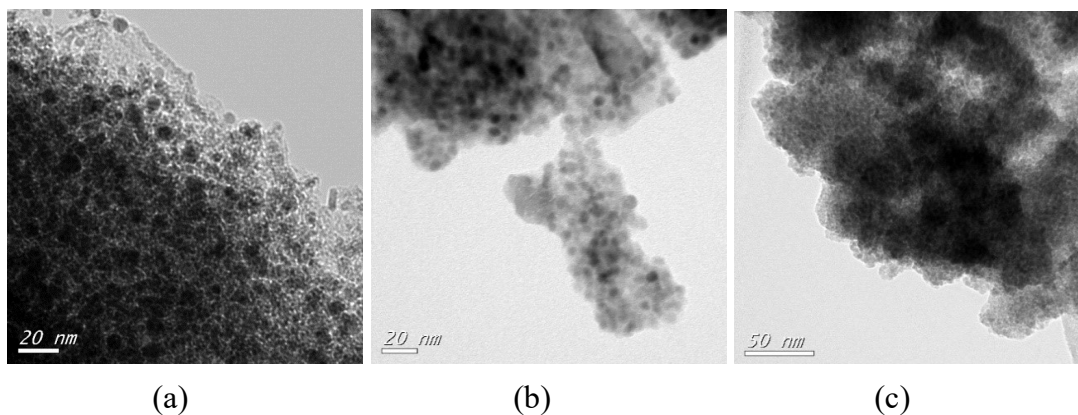


Figure 2.6. TEM images of  $R_{Fe,i} = 0.05$  (a),  $0.20$  (b) and  $0.50$  (c).

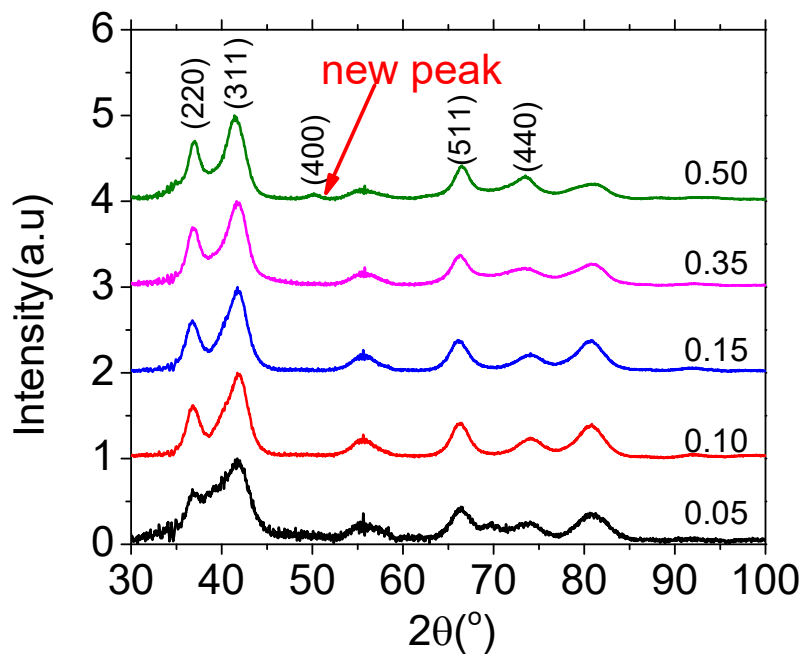


Figure 2.7. XRD diffractograms of  $R_{Fe,i} = 0.05, 0.10, 0.15, 0.35$  and  $0.50$ .

We use XRD to investigate phase and crystal of bare NPs with different Fe concentration. In the Figure 2.7, we can see that the diffractograms of the  $R_{Fe, i} = 0.05-0.35$  NPs are the same. All of them are belong to Wurtzite ZnO phase. This classical crystalline structure for ZnO is presented on Figure 2.8 .

In the case of the sample  $R_{Fe, i} = 0.50$ , we found a new peak, which is the evidence of other phase. By analyzing *XRD*, we found the presence of a cubic spinel phase which is characteristic of the  $ZnFe_2O_4$  crystalline structure in this sample. Analysis of XRD diffractograms allows the determination of cell parameters, and of the crystalline size through Scherrer's formula (also called coherent domain of diffraction). The size of XRD are rather close to the size obtained by TEM and they are always smaller than size TEM. Size of XRD is the size of cristal core, size of TEM is the real size. So, there are amorphous layers outside the NPs. Using stoichiometry we can calculate ration mol/mol between to phase. All these data are presented in Table 2.3.

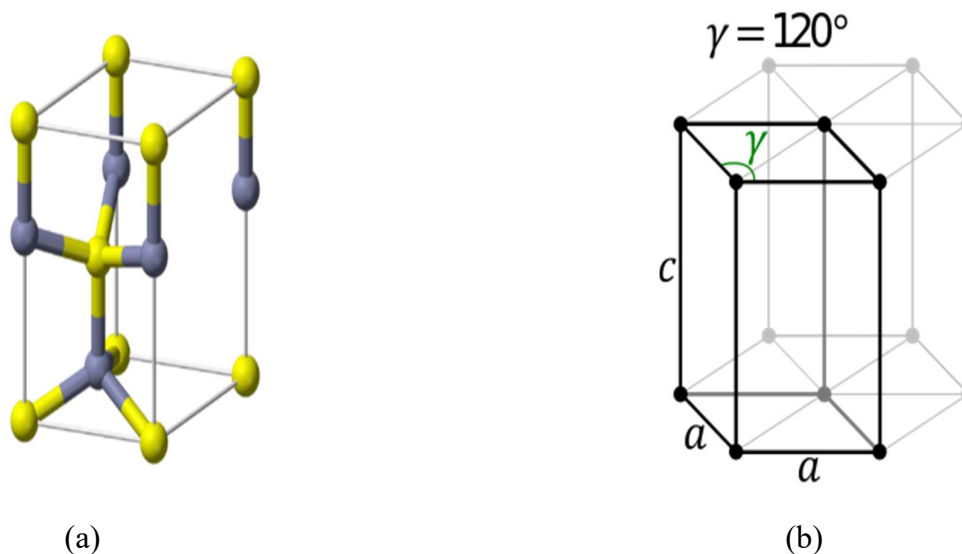


Figure 2.8. Wurtzite structure: (a) unit cell; (b) hexagonal structure [123].

So, XRD evidenced a wurtzite phase of zinc oxide doped with iron ions, with Fe concentration up to  $R_{Fe, i} = 0.35$ , and a mixture of iron-doped wurtzite ZnO phase and a  $ZnFe_2O_4$  cubic spinel phase for  $R_{Fe, i} = 0.50$ . The sizes of NPs obtained from TEM were ranging from about 3 nm to 7 nm, in good accordance with the coherent domains of diffraction obtained from XRD measurements. The sizes are much smaller than the NPs synthesized in previous studies by Balti et al: 17 nm [3], Dinesha et al : 19–34 nm [124],

Ciciliati et al : 11-25 nm [125], Il'ves et al : 10–20 nm [126] and Arciniegas-Grijalba et al : 20- 35 [127].

Without water, the particles are smaller than in presence of water. The main reason could be the quick formation of initial nuclei when the temperature reaches the reaction threshold temperature (at 200°C). Because the quantity of particles is increased, the mean size of resulting particles is decreased [128].

*Table 2.3. Characterization of bare DEG-NPs. Rietveld refinements for NPs with  $R_{Fe, i} = 0.50$  have been performed with the stoichiometry established from chemical analysis.*

$R_{Fe}$ initial	Size TEM (nm)	Size XRD* (nm)	XRD Lattice parameters (nm)	$R_{Fe}$
$R_{Fe, i} = 0.05$	7	5.9	Wurtzite a: 0.325839±6.68E-5; c: 0.53225±2.05 E-4.	0.064
$R_{Fe, i} = 0.1$	ND	7.0	Wurtzite a: 0.32691±3.7 E-5; c: 0.52280±8.9 E-5	0.191
$R_{Fe, i} = 0.15$	6.9	6.7	Wurtzite a: 0.327126±4.6 E-5; c: 0.52281±1.156 E-4	0.179
$R_{Fe, i} = 0.35$	6.3	5.8	Wurtzite a: 0.327094±2.83 E-5 c: 0.531681±2.83 E-5	0.461
$R_{Fe, i} = 0.50$	4.2	3.85	Wurtzite : $Zn_{0.54}Fe_{0.46}O$ a: 0.32499±1.78 E-4; c: 0.530024±3.87 E-4 0.72 (mol/mol), 0.45 (w/w)	0.569
		4.07	Cubic: $ZnFe_2O_4$ a: 0.84752±4.39 E-4 0.28 (mol/mol), 0.55(w/w)	

### ***Coated NPs***

We coated all of NPs with fucoidan for detection of thrombosis by MRI. CMD coating was performed on NPs with  $R_{Fe,i} = 0.50$  and used as a reference for MRI experiments. The TEM images of fucoidan-coated NPs are shown in Figure 2.9. TEM images of fuco-0.35 (a) and fuco-0.50 (b).

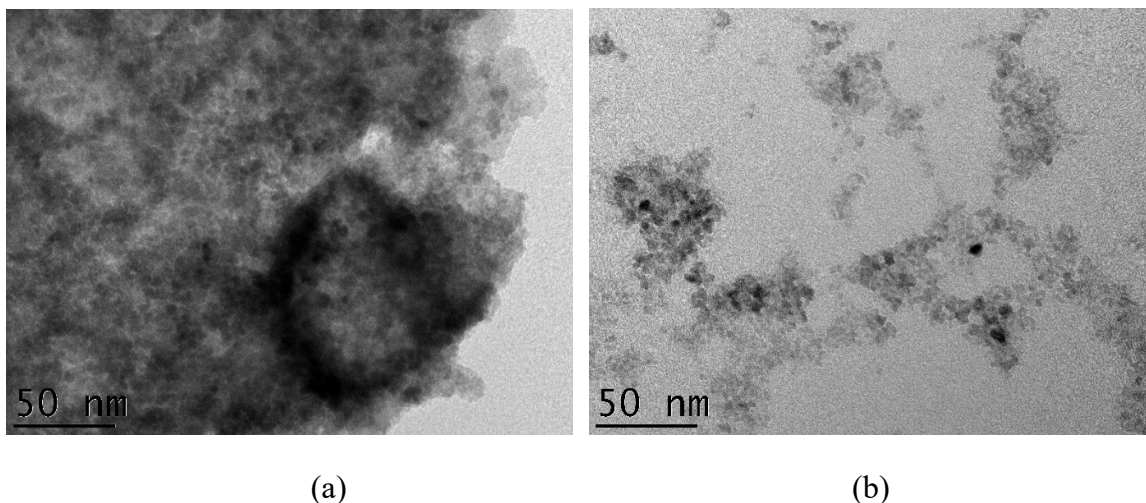


*Figure 2.9. TEM images of fuco-0.35 (a) and fuco-0.50 (b).*

The TEM images did not evidence the fucoidan coating. However, the sizes of the inorganic cores remained below 10 nm with a narrow distribution in good agreement with the sizes of the corresponding bare NPs and XRD data.

Hydrodynamic diameters, zeta-potential and stability of coated NPs in water were determined by dynamic laser light scattering (DLS). As we are going to see it in next subsections, the results of zeta potential, light scattering, IR, absorption spectra and thermogravimetry analysis (TGA) e the presence of fucoidan, and CMD.

### **Stoichiometry**

The formation of  $Zn(Fe)O$  crystals without modification of the elementary cell, ie leading to the same crystal lattice is obtained either by substitution of some zinc ions by iron ions, or by inclusion of iron ions into tetraedic sites of the hexagonal cell [3, 124]. For  $R_{Fe,i} = 0.50$ , we tried to propose a stoechiometry for the hexagonal phase by making the hypothesis of substitution. In this case there is a simple relation between iron and zinc content:  $Zn_x(Fe)_yO$  with  $x+y=1$

Let us assume that the number of mol  $Zn_x(Fe)_yO$  and  $ZnFe_2O_4$  is labelled by  $a$  and  $b$ , respectively.

From XRD data, we found that the ratio between weight of  $Zn_x(Fe)_yO$  and  $ZnFe_2O_4$  is 0.43:0.57 (table 2.2). From AAS data, the ratio between the number of mol of Zn and of Fe in  $R_{Fe, i} = 0.5$  would be 0.45:0.55.

Hence, we can evaluate  $x$  and  $y$  by solving the system of equations 2.1:

$$\begin{cases} x + y = 1 \\ \frac{(65x+56y+16)a}{(65+168+48)b} = \frac{0.45}{0.55} \\ \frac{xa+b}{ya+2b} = \frac{0.43}{0.57} \end{cases} \quad (2.1)$$

In this system, the first equation accounts for the fact that Fe doping in ZnO takes place by substitutions of Zn by Fe, the second equation accounts for the 0.45:0.55 weight ratio between both phases, and the third equation accounts for the ratio of the number of mol of Zn and of Fe. Finally, we have:

$$\begin{cases} a = 2.55b \\ x = 0.54 \\ y = 0.46 \end{cases} \quad (2.2)$$

From the calculated results, we know that the DEG-0.50 is the mixture of  $Zn_{0.54}(Fe)_{0.46}O$  and  $ZnFe_2O_4$ , and the ratio between number of mol  $Zn_{0.54}(Fe)_{0.46}O$  and  $ZnFe_2O_4$  is 2.55:1. The ratio of Zn and Fe in  $Zn_x(Fe)_yO$  phase is rather similar with the initial composition. In addition, the beginning of formation of  $ZnFe_2O_4$  in this sample can be observed.

### Hydrodynamic size and stability

The colloidal stability of fuco-NPs dispersed in physiological suspension was compared with that of uncoated ones. The bare DEG-NPs are stable in ethanol, but when it was changed to water medium, a quick aggregation is observed. After few hours, most of DEG-NPs were precipitated. In contrast to uncoated one, the suspension of fuco-NPs remained stable for more than 3 months in water or PBS solution (Figure 2.10).



Figure 2.10.  $R_{Fe,i} = 0.50$  (left), *fuco-0.50* (middle), and *fuco-0.50* with applied magnetic field (right) in PBS.

We measured the hydrodynamic diameters and the zeta-potentials of coated NPs dynamic laser light scattering (DLS) in water at pH ranging from 6.5 to 6.8 (table 2.4). Size distribution of *fuco-0.50*, and *CMD-0.50* is presented in Figure 2.11.

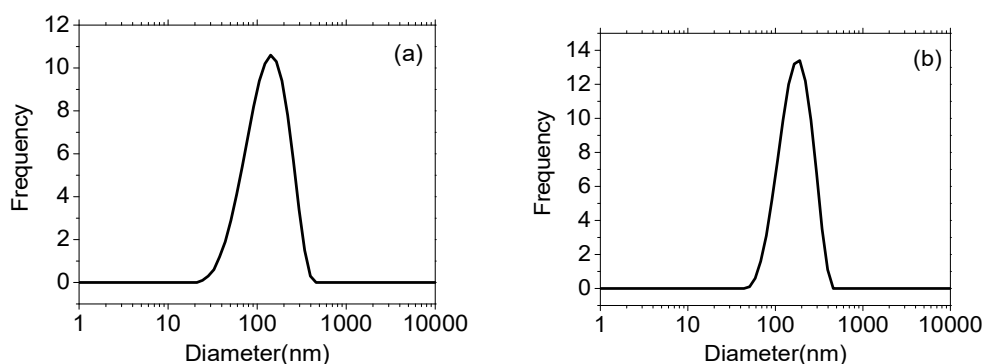


Figure 2.11. Size distribution of *fuco-0.50* (a), and *CMD-0.50* (b).

Polydispersity index (PDI) indicates the stability of the NPs colloidal suspension:

PDI = 0-0.2: suspension is monodisperse,

PDI = 0.2-1: suspension is polydisperse,

PDI > 1: suspension is aggregated.

The results indicate that coated NPs with  $R_{Fe,i} = 0.5$  suspension is stable, whereas aggregation was observed with lower ratios.

The table 2.3 gathers the average sizes and the zeta potentials of fucoidan-coated NPs. Although we focused on *fuco-0.50*, NPs with  $R_{Fe} = 0.05$ , 0.15 and 0.35 have been successfully coated with fucoidan. With the exception of *fuco-0.05*, all sizes were lower than 500 nm and negative zeta potentials evidenced the negatively charged coatings.

Table 2.4. Average hydrodynamic size and zeta potentials of NPs

Coating - $R_{Fe}$	Core size (nm)	Size (nm)	Zeta-potential (mV)	PDI
Fuco-0.05	5.9	1153	7.3	0.582
Fuco-0.15	6.7	459	-32.4	0.425
Fuco-0.35	5.8	362	-36.8	0.463
Fuco-0.50	4.2-7.4	162	-48.7	0.135
CMD-0.50	4.2-7.4	177	-33.3	0.150

### Magnetic properties

The magnetic properties of  $R_{Fe, i} = 0.50$  (powder) were determined at 5K and 300K using a vibrating sample magnetometer (VSM) when the applied field ranged from  $-70$  to  $+70$  kOe (Figure 2.12b). Hysteresis plots show the variation of magnetization ( $M$ , emu/g) as a function of applied magnetic field ( $H$ , Oe). We determined also the magnetic properties of the coated NPs at 300 K when the applied field ranged from  $-30$  to  $+30$  kOe (Figure 2.12c). It is clear from Figure 2.12b that  $R_{Fe, i} = 0.50$  is superparamagnetic with saturation magnetizations of 53 emu/g and 27 emu/g at 5K and 300K, respectively. With  $R_{Fe, i} = 0.50$ , crystal phase of NPs is a mixture of  $ZnFe_2O_4$  and Wurtzite (Wurtzite: 0.45;  $ZnFe_2O_4$ : 0.55(w/w)), which is superparamagnetic with a very small hysteresis loop at room temperature [129, 130]. Fuco-0.05, fuco-0.15 and fuco-0.35 are paramagnetic (see Appendix H) whereas fuco-0.50 is superparamagnetic as expected since the coating did not modify the structure of the inorganic core. The saturation magnetizations of  $R_{Fe, i} = 0.50$ , fuco-0.50 and CMD-0.50 were approximately 22-25 emu/gram (Figure 2.12c).

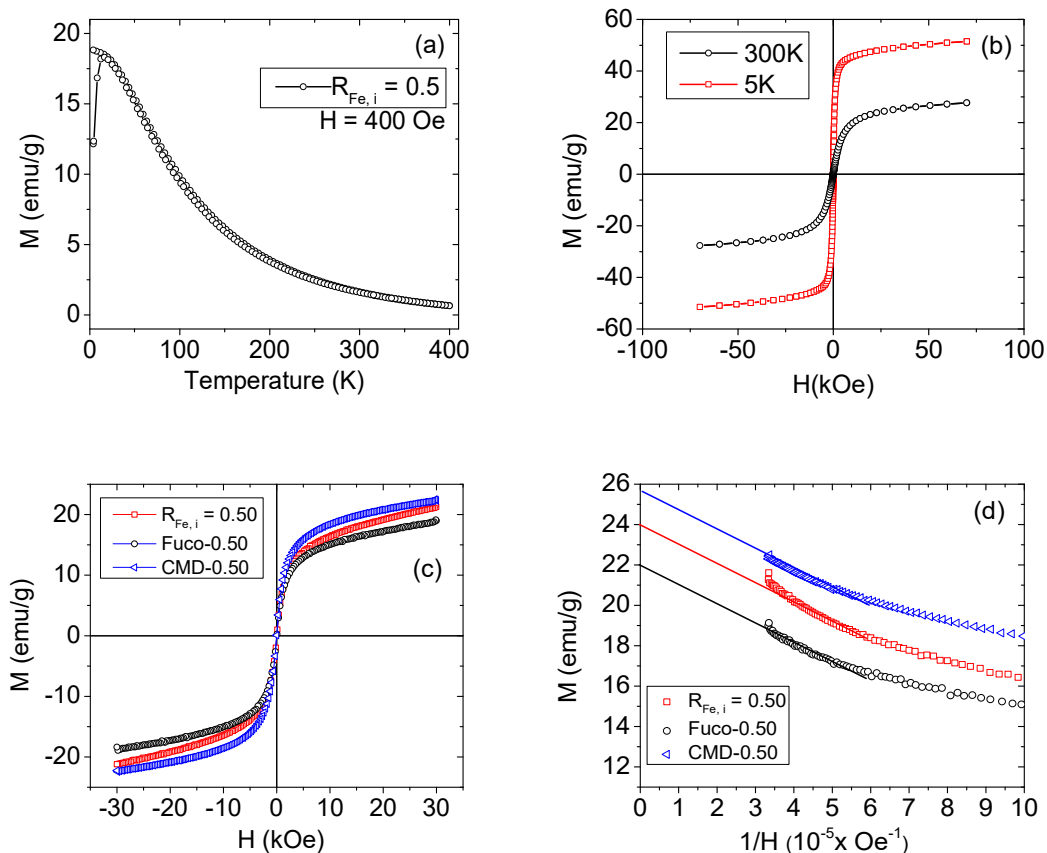


Figure 2.12. Magnetization ( $M$ ) versus temperature (a), versus applied field ( $H$ ) at 5 K and 300 K (b) of  $R_{Fe,i} = 0.50$ , and versus applied field ( $H$ ) of  $R_{Fe,i} = 0.50$ , fuco-0.50 and CMD-0.50 in water (c, d).

### Absorbance and fluorescence spectra

The absorption spectra of  $R_{Fe,i} = 0.50$ , fuco-0.50 and CMD-0.50 are presented in the Figure 2.13. The absorption wavelength of NPs was observed in UV band.

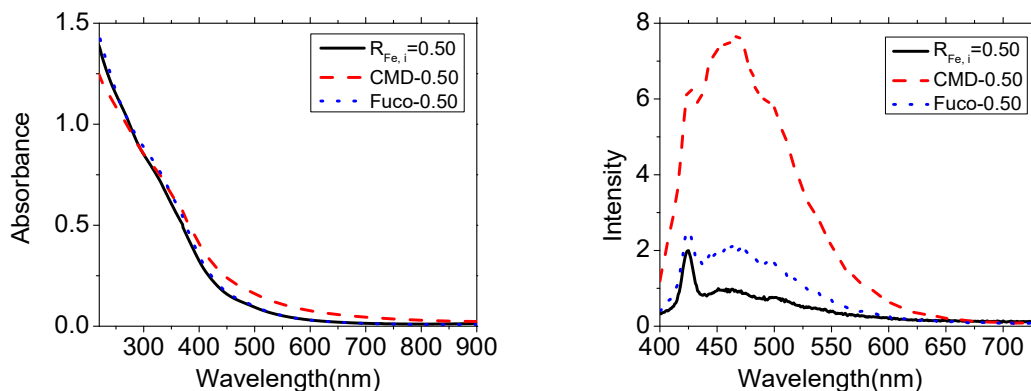


Figure 2.13. Absorption spectra (left) and fluorescence spectra (right) of  $R_{Fe,i} = 0.50$ , fuco-0.50, and CMD-0.50 with 370 nm excitation wavelength.

We looked at the photoluminescent properties of coated NPs in water. The photoluminescent spectra with an excitation at 370 nm indicated that the  $R_{Fe,i} = 0.50$  have a broad visible band with a maximum intensity of photoluminescence at 470 nm due to various intrinsic defects in oxides such as oxygen vacancies, interstitial zinc, singly ionized oxygen vacancies, antisite oxygen, zinc vacancies and even oxygen surface defects [131, 132, 133].

### Infrared absorption spectroscopy

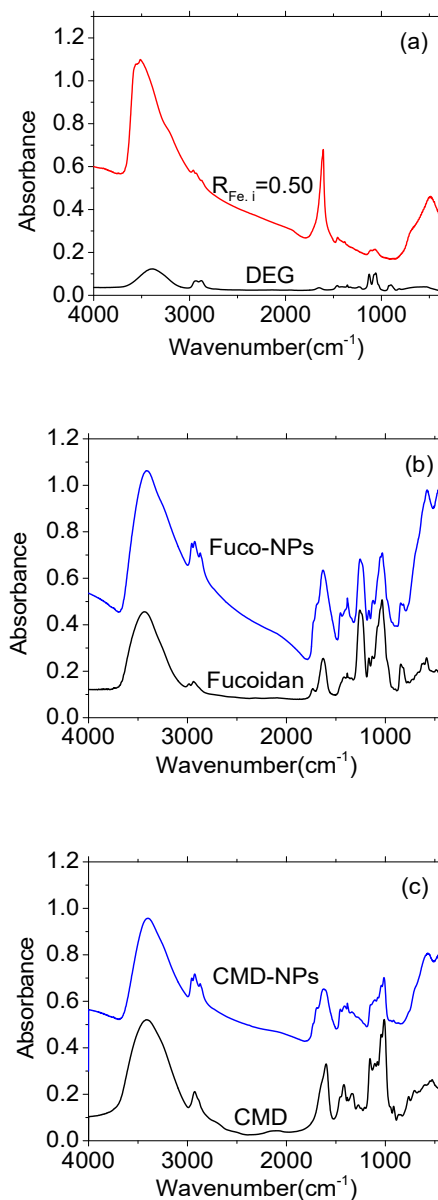


Figure 2.14. IR absorption spectra of  $R_{Fe,i} = 0.50$  (a), fuco-0.50 (b), and CMD-0.50 (c).

We compared infrared (IR) absorption spectra of uncoated  $R_{Fe, i} = 0.50$  with those of coated NPs. The surface coatings can be evidenced (Figure 2.14).

We can clearly see the difference of the infrared absorption spectra peaks between uncoated NPs and coated NPs. In addition, the peaks of infrared absorption spectra between the coated NPs and the surface coatings material completely matched. The results evidenced fucoidan, and CMD in the studied samples.

### Thermogravimetry analysis

Thermogravimetry analysis (TGA) is a method of thermal analysis that can give information about amount of water and organic layer in the decomposition of coated NPs by tracking the weight loss versus time and temperature. In this measurement, 15 mg of coated NPs were put in a furnace tube. The temperature of the furnace was controlled from 30 °C to 1500 °C.

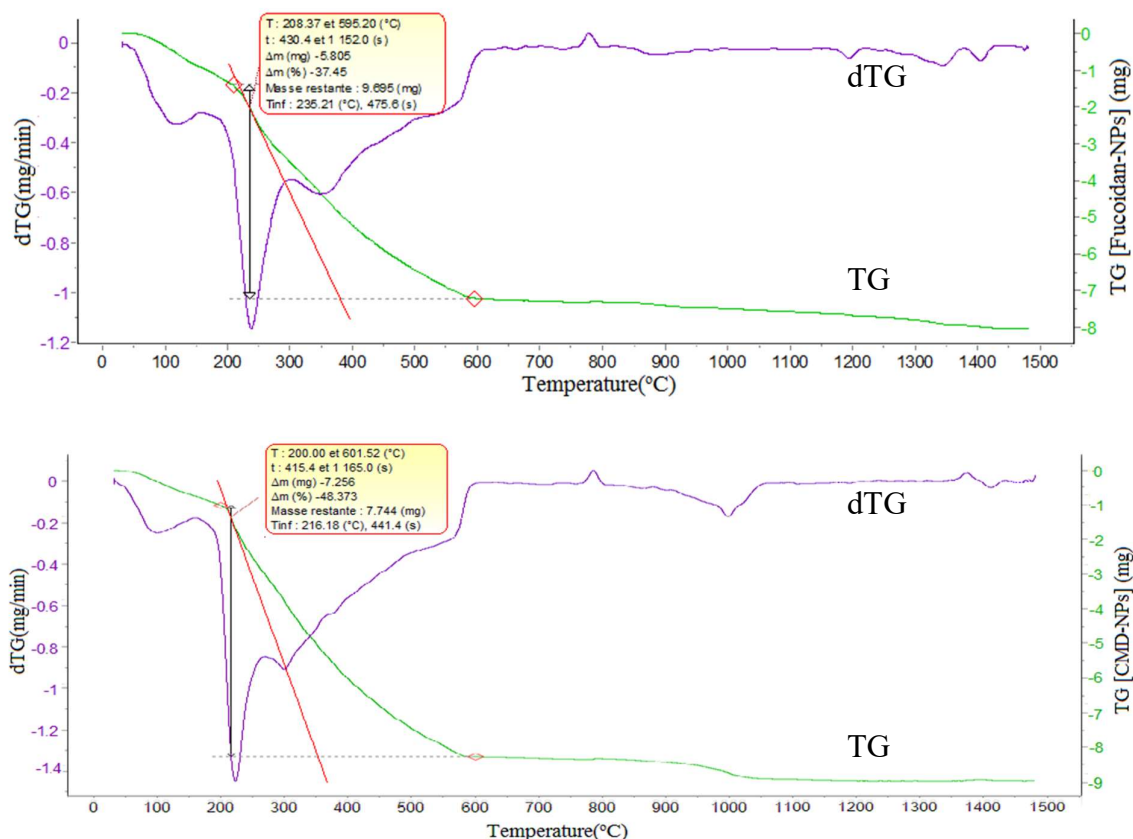


Figure 2.15. Thermogram of fuco-0.50 and CMD-0.50.

The thermogram is presented on Figure 2.15, where the sample mass is plotted (green curve) together with its derivative (mass loss versus temperature, violet curve). In this

figure, the first slope is the loss of free water which was complete around 200°C. The second slope is the carbonization of the cover materials and this process takes place between 200 °C and 600 °C. The last slope corresponds to the remaining oxide NPs that lost very little mass between 600 °C and 1500 °C. By calculating the mass loss of the sample, the weight ratio of cover material to the metal oxide core could be estimated.

By analyzing the thermogram, we estimated that fuco-0.50, and CMD-0.50 contained 37.4%, and 48.4% of polymer, respectively. From ratio of weight between the coating material and the core, average number of fucoidan molecule per NP was estimated 57 and average number of CMD molecule per NP was 22-44.

### **Fucoidan content**

The fucoidan content (mol/w) in fuco-0.50 sample was determined by a colorimetric method currently used in the LVTS [35]. From this result, we have estimated the average amount of fucoidan molecule per nanoparticle by considering the following data:

- XRD data have established that fuco-0.50 is a mixture of 0.45/0.55 (w/w) of wurtzite/ spinel cubic nanocrystals with the average diameter of NPs in both phases is approximately 4.0 nm.

- All calculations were performed by considering an average density of NPs of 5.0 g/cm<sup>3</sup>, corresponding to ZnO-based nanoparticulate systems described in the literature [35].

- Whatever the diameter of the NPs, fucoidan molecules likely interact with their surface in a similar way.

Thus we established that 0.5 mg of NPs was corresponding to  $2.5 \times 10^{15}$  NPs, with surfaces of 1400 cm<sup>2</sup>. Knowing that the sulfate content and the molecular weight of fucoidan were 26.5 g/100g and 10,100 g/mol respectively, a suspension of 17.36 mg of fuco-0.5/mL would correspond to 47 nmol of fuoidan/mg. Eventually, the average number of fucoidan molecule per NP was estimated 30. This result is good agreement to our results from TGA.

### Relaxivity

Relaxivity is an importance parameter of a MRI contrast agent. The relaxivity of coated NPs in water was measured by MRI.

We prepare a lot of tubes with different Fe concentration. In MRI image, the contrast agent will have darkening effect. The higher concentration the darker image.

Figure 2.16 shows MRI image of tubes with different Fe concentration. Tube lettered with A is the most concentrated of Fe, and G is the most diluted Fe concentration. Relaxation times  $T_1$  and  $T_2$  of samples were obtained by fitting average intensity of sample versus time with exponential function.

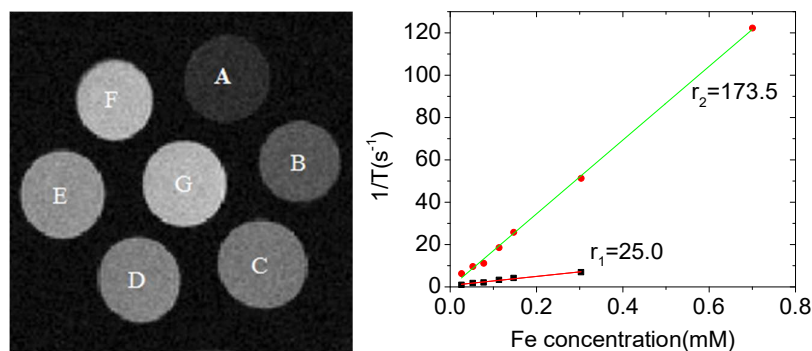


Figure 2.16. MRI image (left) and relaxivity determination of Fucoidan-NPs suspension ( $R_{Fe}=0.5$ ) with ( $C_{Fe} = 0.7(A), 0.303(B), 0.147(C), 0.113(D), 0.0774(E), 0.0522(F),$  and  $0.0261(G)$  mM).

The relaxation rates of NPs in suspension were obtained by linear fitting relaxation rates ( $1/T_1$ ) and ( $1/T_2$ ) versus different Fe concentrations. The slopes of the lines present  $r_1$  and  $r_2$ .

Contrast agents can be divided into two categories, based on the  $r_2/r_1$  ratio. The low  $r_2/r_1$  ratios (close to 1) are referred to as  $T_1$  contrast agents. On the other hand, with  $r_2/r_1$  ratios superior to 5 are called  $T_2$  contrast agents [134, 135]. The  $r_2/r_1$  ratios of NPs ( $R_{Fe} = 0.05, 0.15, 0.35$  and  $0.50$ ) are from 3.9 to 6.9 ( $\gg 1$ ), the value indicates that the NPs had the potential as effective  $T_2$  contrast agents.

We selected the NPs with  $R_{Fe} = 0.50$  for MRI because of the high  $r_2$  value. It can be found in the literature that the value of  $r_2$  does not only depend on maximum magnetization but also depends on coating agents, particle size and shape [136]. The values of  $r_2$  and  $r_2/r_1$  ratio can be controlled by modulating the size [134]. Table 2.5 shows results of relaxivity of

our NPs compare to the other publications. Relaxivity is depended on coating agents, particle size and shape. With the same size of NPs, our NPs have better  $r_2$  value than the other.

Table 2.5. Characterization of coated NPs compared to references

magnetic core	TEM core size (nm)	coating	$r_1$ (mM <sup>-1</sup> s <sup>-1</sup> )	$r_2$ (mM <sup>-1</sup> s <sup>-1</sup> )	$r_2/r_1$	$B_0$ (T)	refs
Zn(Fe)O + ZnFe <sub>2</sub> O <sub>4</sub> , R <sub>Fe</sub> =0.5	4.3	fucoidan	25.0	173.5	6.9	7	this works
Zn(Fe)O + ZnFe <sub>2</sub> O <sub>4</sub> , R <sub>Fe</sub> =0.5		CM dextran	43	295	6.8	7	this works
iron oxide	4.5	dextran	10.1	120	11.9	1.5	[137]
iron oxide	3 – 5	dextran	7.3	57.0	7.8	1.5	[138]
iron oxide	4.5	dextran + citrate	5.0	66.0	13.2	1.4	[139]
γ-Fe <sub>2</sub> O <sub>3</sub>	3	PEG-phosphine oxide	4.8	29.2	6.1	3	[140]
γ-Fe <sub>2</sub> O <sub>3</sub>	4.8	uncoated	3.52	28.3	5.9		[141]
Fe <sub>3</sub> O <sub>4</sub>	4	PEG-phosphine oxide	5.9	39	6.6	1.4	[142]
Fe <sub>3</sub> O <sub>4</sub>	2.2		6.15	28.62	4.65		[143]
ZnFe <sub>2</sub> O <sub>4</sub>	4.8	chitosan		68		9.4	[144]
ZnFe <sub>2</sub> O <sub>4</sub>	4.8	PEG		76		9.4	[144]
ZnFe <sub>2</sub> O <sub>4</sub>	6.1	hydrophilic polyol ligands	6.84	15.77	2.31	1.41	[145]
ZnFe <sub>2</sub> O <sub>4</sub>	5.9	PEG	0.60	49	82	9.4	[146]

### 2.2.3. Conclusion

Water removal using Dean-Stark apparatus is a novel strategy for the synthesis of NPs in polyol solution with high yield and small size. Using PG as solvent, we obtained NPs with high yield, and small size, but the magnetic properties of those NPs were very weak, and they were not suitable for MRI.

Using DEG as solvent, the transition from wurtzite ZnO phase to ZnFe<sub>2</sub>O<sub>4</sub> spinel phase could be seen when we increase the Fe concentration up to 0.5, shown by a superparamagnetic behaviour at room temperature. However, because of a high homogeneity of nanocrystal size, the phase mixture could only be demonstrated by XRD analysis. The fucoidan and CMD coatings were confirmed by DLS, FT-IR spectra, and TGA results. Fucoidan-coated and CMD-coated NPs with  $R_{Fe, i} = 0.5$  were used for animal experiments as described in chapter 4.

## Chapter 3. Optics

In optical imaging, the microscope is one of the most important equipment. We can improve both the contrast of images and the ability to detect NPs by the use of additional components.

### 3.1. Development of the optical system

Image data was collected with a Zeiss inverted microscope (Axio Observer A1m) equipped with an Andor EMCCD camera (Andor iXon 897) cooled at  $-70^{\circ}\text{C}$ . We modified the microscopy setup using some external optical elements in different configurations for imaging atherothrombosis.

#### 3.1.1. Fluorescence microscopy

##### Experimental setup

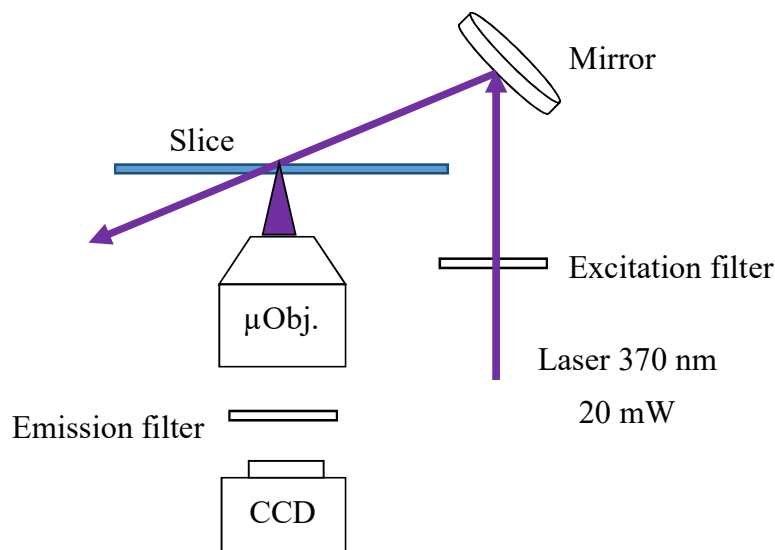


*Figure 3.1. Fluorescence microscopy configuration.*

This is the basic setup (Figure 3.1). A 20 mW UV diode laser (Laser Stradus, Vortran Medical Technology) is the light source. A filter cuts off the unwanted photons from the laser source: the laser indeed has some internal parasitic fluorescence, which could be seen on the fluorescence spectrum. An aluminium mirror directs the laser beam towards the sample. Another filter stops the laser beam from hitting the CCD camera. A microscope collects fluorescence signal from the sample.

### 3.1.2. Simple dark field microscopy

#### Experimental setup

Because dark field microscopy can provide very high contrast images, we developed a dark field microscope to detect our NPs by scattering. If successful, this microscope can be used in order to image atherothrombosis. Dark field microscopy configuration is shown in Figure 3.2.

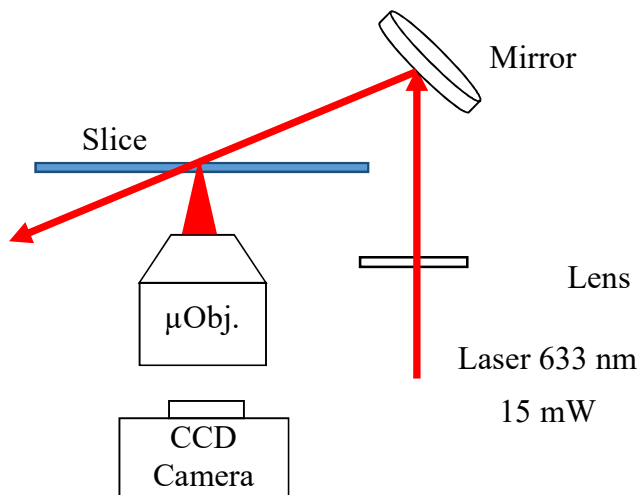


Figure 3.2. Dark field microscopy configuration.

A 14 mW polarized Helium-Neon laser (Melles Griot) is the source light. Here we don't use polarization for our measurements. However, we are sure that random rotation of the polarization inside the laser doesn't induce fluctuations in the intensities. An aluminium mirror direct the focused laser beam to the sample contained in a capped cuvette or between two glass slides. By using lenses, laser beam size is adjusted to about 100  $\mu\text{m}$ . Again, scattered light from the sample is collected by the microscope.

### 3.1.3. Dark field interference microscopy

#### Experimental setup

This is an evolution of the previous basic dark field microscope (see Figure 3.3). Now the microscope is part of an interferometer. We use the same 14 mW Helium-Neon laser as source light. The laser beam is split by 5:95 beam splitter. The strong beam (95% of energy) is focused on the sample. By using lenses, laser beam size is about 100  $\mu\text{m}$  diameter at the

sample. The remained beam (5% of energy) passes through a 10X beam expander. It is the reference beam of the interferometer. The interference images between dark field image and reference beam are recorded by the EMCCD camera (see Figure 3.4). A microscope is used for collecting scattering light from NPs.

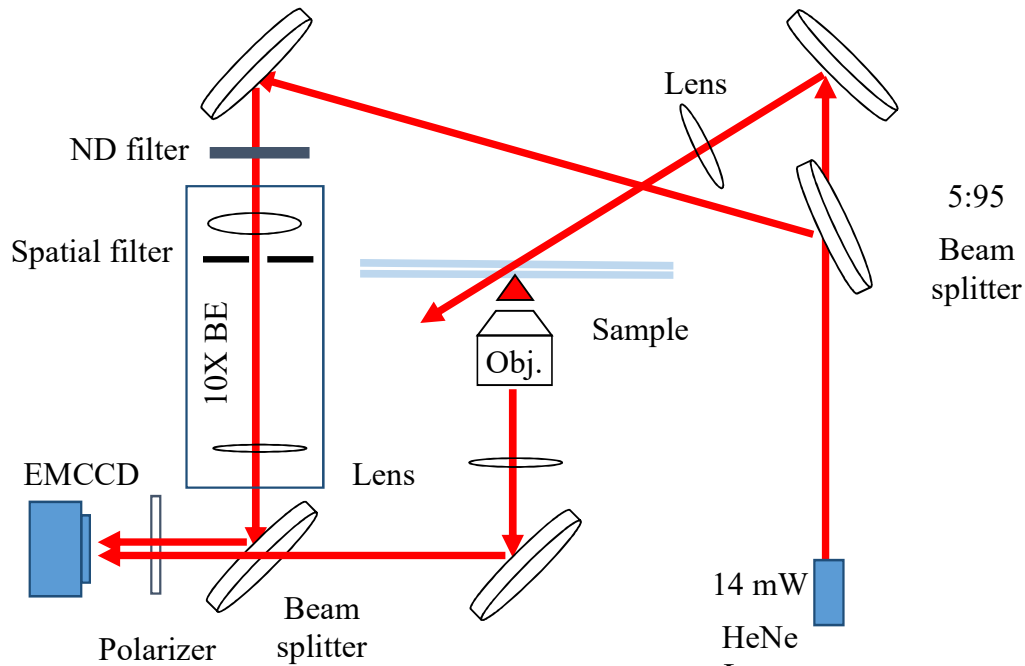


Figure 3.3. Dark field interference microscopy configuration.

Because this microscopy is based on interference, there are some advantages and disadvantages of this microscopy technique.

**+ Advantages:**

- High contrast, low cost.
- Easy and accurate determination of the depth position within a large depth range with the possibility to track many NP at the same time.
- It should be possible to extract the interference signal of NPs from strong background noises by using a high pass frequency filter.

**+ Disadvantages:**

- Difficult to align the beam properly.

- Sensitive to vibrations due to human activities, building vibration, acoustic noise.

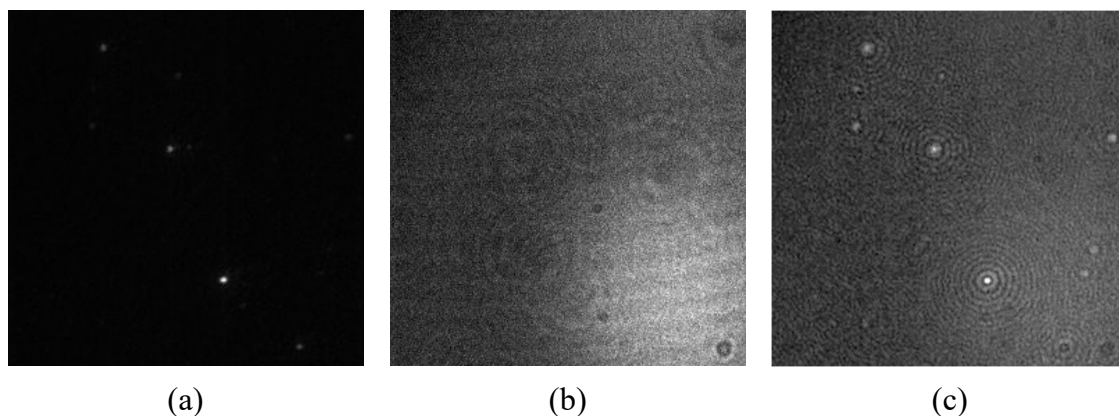


Figure 3.4. Dark field image of NP (a), reference laser beam (b) and interference image (c).

### 3.1.4. Dark field hyperspectral microscopy

Hyperspectral imaging has been used in numerous applications in diverse fields such as agriculture, chemical imaging, food processing, environment and military. More recently, hyperspectral imaging microscopy plays an important role in biological imaging applications, where it has found utility to precisely identify and quantify 10 molecular markers in individual cancer cells in a single pass [147]. It can also be used for nanoparticles mapping [148, 149].

#### Experiment setup

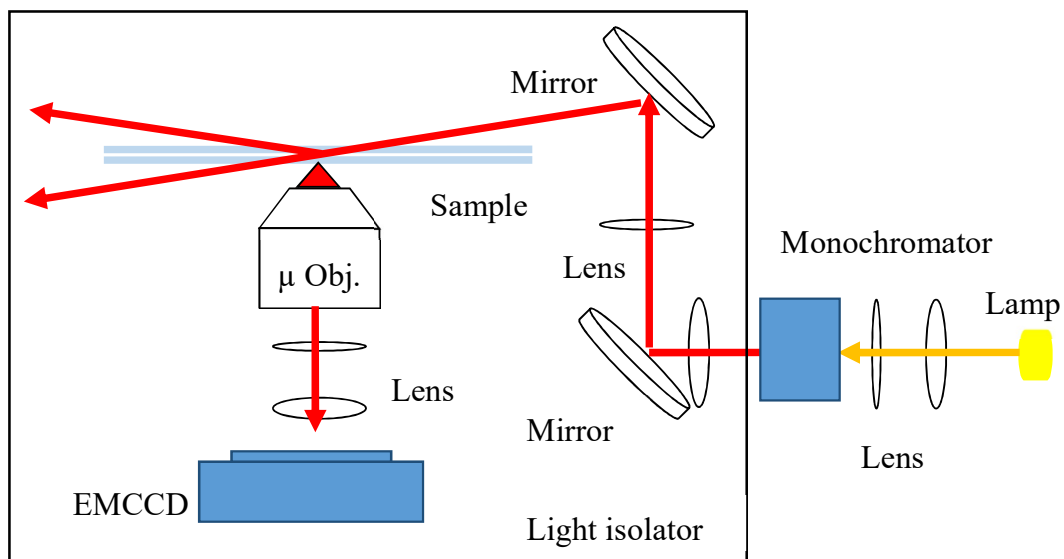


Figure 3.5. Hyperspectral dark field microscope configuration.

We built our own system based on our microscope (see Figure 3.5). The source is a 50 Watt halogen lamp. By using lenses and mirrors, the light beam passes through a 1 nm resolution monochromator. The selected light is focused into the sample. The EMCCD camera shoots images through the microscope. All measurements are taken at room temperature (20°C). A motor attached to the spectrometer tunes the wavelength. At each step, a 14 bits image of the sample is recorded. The full set of images, from 400 nm to 900 nm, is analysed by a homemade software, written in the Matlab language using the Spectral Angle Mapper algorithm (SAM).

### 3.2. Use of NPs with optical system

#### 3.2.1. Dark field microscopy for real-time 2D NPs tracking

##### Image processing

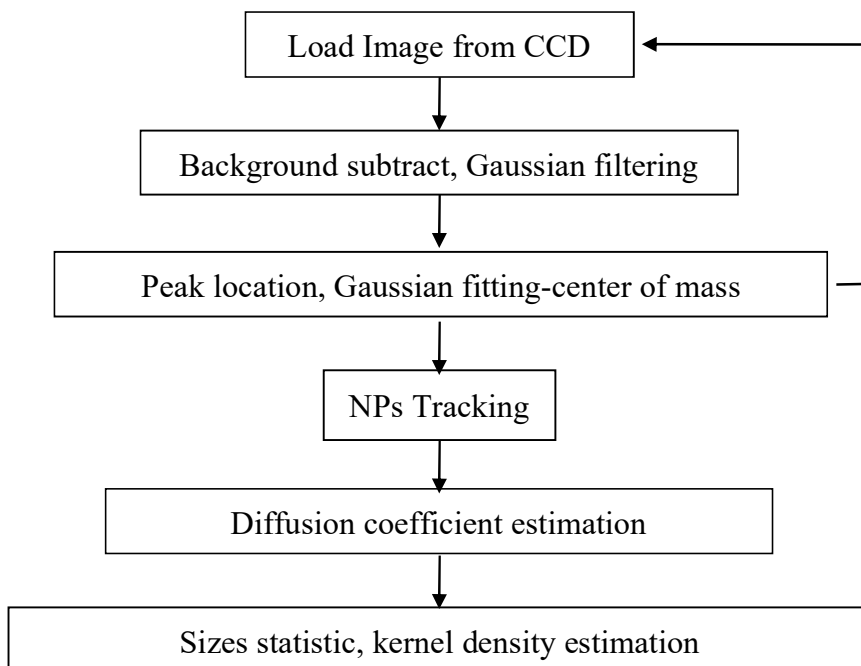


Figure 3.6. The flow charts for estimating particle size distribution.

Nanoparticle tracking analysis (NTA) allows us to determine the size distribution profile of a group of nanoparticles in liquid suspension whose sizes range from tens to thousands nanometers. This technique uses an intense laser beam to illuminate freely moving particles dispersed in the liquid medium. It tracks their Brownian motion by analysis sequential images, and it estimates their size distribution using the Stokes–Einstein

relation. Speed of motion not only depends on the viscosity but also on the temperature of the fluid. It is not affected by particles density or their refractive index. NTA allows determining size distribution of small particles with a diameter of about 10-1000 nanometers (nm) in liquid [150]. This technique can be used for tracking motion of individual NPs inside the living cell.

A stack of images of NPs moving in suspension is recorded by the camera. Each individual image undergoes background subtraction and noise filtering. Then the position of the nanoparticles is determined by finding the local maximum intensities. Each center is positioned with subpixel accurately ( $<1$  pixel) by using a 2-dimensional Gaussian fitting method or center of mass estimator. Once the NPs are being tracked, the diffusion coefficient and size of NPs can be estimated in real time.

### ***Background subtraction***

A background image is calculated from a large set of recorded images. If the laser power is stable, and if all optical elements are well fixed, every pixel of background image should be the minimum value at the same position within all the current data set.

### ***Image filtering***

Noise is an unavoidable phenomenon during any measurement. A low-pass filter is often used before using peaks detection algorithm because the detection algorithm is very sensitive to random noise (Figure 3.7). With the use of a Gaussian filter, we can improve the results of the peak detection algorithm. Mathematically, applying a Gaussian filter to an image is convolving the image with a Gaussian function. It is a frequently used as a low pass filter.

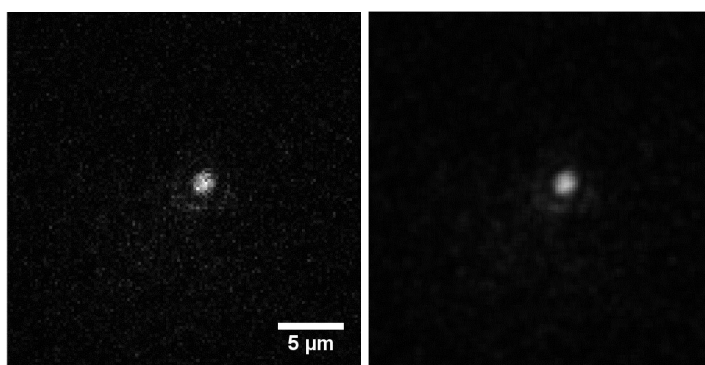


*Figure 3.7. Image of single a single NP before (left) and after applying a Gaussian filter (right).*

### ***Peaks detection and subpixel resolution***

After applying the gaussian filter, in order to remove noise, each pixel of the image whose intensity is higher than a given threshold value compared with at least 16 neighborhood pixels is marked as the local maximum. That is, it is selected if intensity of neighboring pixels decrease in 8 directions. This is described in the Figure 3.8. The number of neighbors should be high enough to avoid false detection of a maximum due to the relatively big diffraction rings around strongly scattering nanoparticles. Position of the maximum pixel is said to be the initial position of the NP.

If two or more maximum pixels are too close, that is if the distance between them is closer than a given value (normally comparable to the spatial resolution of the microscope), the pixel which has the biggest value will be kept as the “true” maximum. The other will be discarded as a false positive.

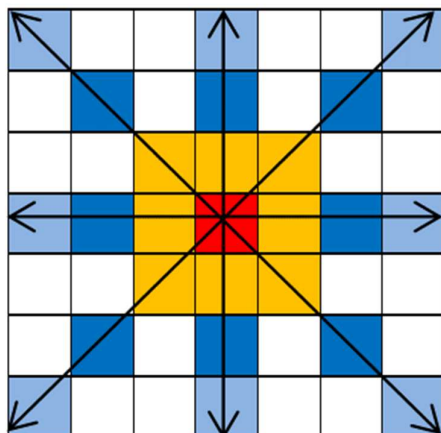


*Figure 3.8. Peaks detection algorithm, a pixel is determined as a peak if it is stronger than at least 16 nearby pixel in 8 different directions.*

We can find many algorithms designed to improve accuracy when determining the center of the NPs. Gaussian function fit and center of mass are used because these methods are simple while providing a high accuracy.

For each NPs found by its maximum, the software crops the full picture into smaller pictures, called a ROI images (Region Of Interest). Those images contain all of an individual particle signal. We process these ROI in order to find precisely the location of the

particle with sub pixel accuracy. The accuracy of the two methods is described and compared in 0.

### ***Gaussian fit with least squares method***

Least squares method is a favourite method for locating particles with subpixel resolution because it is the most reliable one. Data from the ROI images are fitted with a two-dimensional Gaussian function by the least squares method (Figure 3.9). The results will determine the center position of the Gaussian with sub pixel resolution. The accuracy of this method depends on the scattering intensity of the particles. The resolution  $d$  is calculated as equation 3.1 [151]:

$$d = \frac{1}{\sqrt{N}} \times \frac{\lambda}{NA} \quad (3.1)$$

Where  $N$  is the number of photons collected from a particle,  $\lambda$  is the wavelength of light and  $NA$  is the numerical aperture of objective lens microscope.

Typically, image of particles on the sensor should be spread over 9 pixels to ensure resulting matches in the most accurate way.

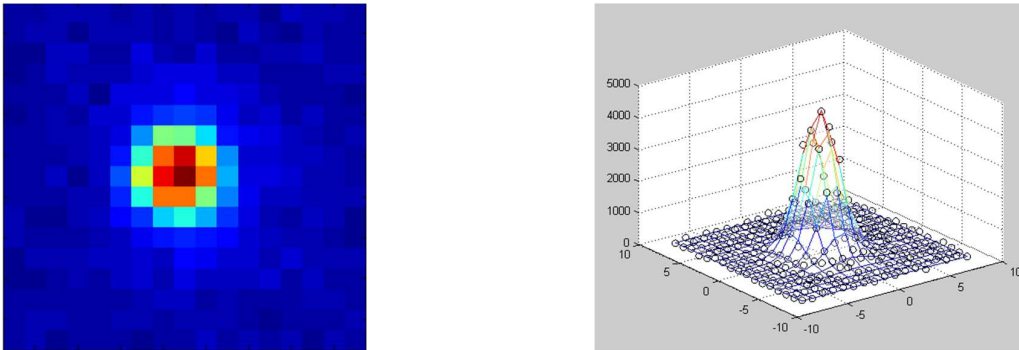


Figure 3.9. ROI Image (left) 2D Gaussian function is applied to locate center more precisely (right).

### ***Center of mass method***

Center of mass is a simple method to calculate subpixel position. For each dimension, the center is given by equation 3.2:

$$C_x = \frac{\sum_i \sum_j (x_i \times I_{ij})}{\sum_i \sum_j I_{ij}} \quad (3.2)$$

where:  $x_i$  is the position in that dimension

$I_{ij}$  is the intensity of a given pixel

Even if this method is extremely simple, its calculated results are rather good. So this method is a favourite when one has to deal with a very big data set with a limited computing power.

### ***Diffusion coefficient and size estimation***

In order to process NPs tracking, we first have to determine a region of interest where the particle movement will be analysed. Knowing particles minimum size in the sample, the temperature and the viscosity, the maximum-expected diffusion coefficient  $D_{max}$  can be calculated by the Stokes–Einstein relation equation 3.3.

$$D_{max} = \frac{k_B T}{3\pi\eta d_{min}} \quad (3.3)$$

where:  $k_B$  is the Boltzmann constant,  
 $T$  the absolute temperature,  
 $\eta$  the viscosity of the medium and  $d$  the diameter.

We can therefore introduce a radius  $R$  for this region of interest: if we choose for instance  $R = 3\sqrt{\pi D_{max} \Delta t}$ , more than 99% of the expected particle steps are shorter than this radius [152]. Then, according to the same Stokes–Einstein relation, the diffusion coefficient for a spherical particle is expressed as:

$$D = \frac{k_B T}{3\pi\eta d} \quad (3.4)$$

For  $n$  dimensions the time dependence of mean square displacements for isotropic diffusion are:

$$\langle(\Delta r)^2\rangle = 2 \times n \times D \times \Delta t \quad (3.5)$$

where  $\langle(\Delta r)^2\rangle$  is the mean squared displacements corresponding to the time interval  $\Delta t$ . The diffusion coefficient can therefore be obtained by calculating squared displacements of each nanoparticle in the sequence of images. We used the “regression method” in order to calculate the estimated size of nanoparticles. The regression method is the most often used method in the literature to estimate the diffusion coefficient because it is simple and

fast. Squared displacements can be plotted versus the time intervals. The diffusion coefficient is estimated by the slope of the regression line fitting.

### Results and discussion

We have synthesized  $R_{Fe, i} = 0.20$  NPs by polyol method. These NPs were suspended in DEG in order to slow down their movements. We chose the concentration to be  $2 \times 10^7$  particles/ml of NPs. We tracked the Brownian motion of uncoated NPs in DEG cuvette (Figure 3.10), and the estimation of the diffusion coefficient is presented in Figure 3.11.

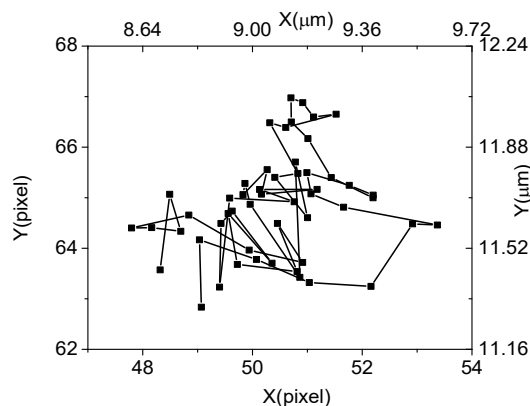


Figure 3.10. Brownian motion of NPs in DEG.

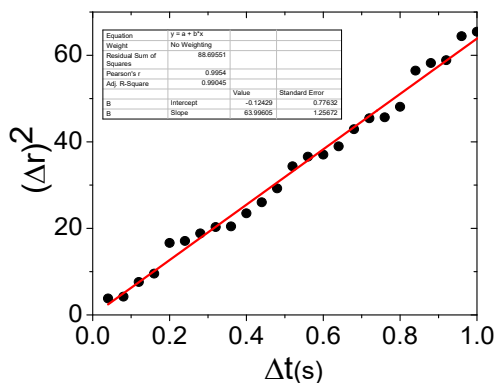


Figure 3.11. Estimation of the diffusion coefficient.

Because the Rayleigh scattering decreases as the sixth power of diameter, NPs with very small size are very difficult to observe. As long as light scattering signals from NPs is higher than the noise of the medium, we can track the NPs and estimate their sizes. In our experiments, by isolating strong light scattering originating from the glass wall, the NPs with hydrodynamic diameter close to 30 nm can be tracked by our dark field microscope

(Figure 3.12). The limit of this method depends on the signal to noise ratio thus is given mostly by the combination of the laser intensity and the sensitivity of the detector.

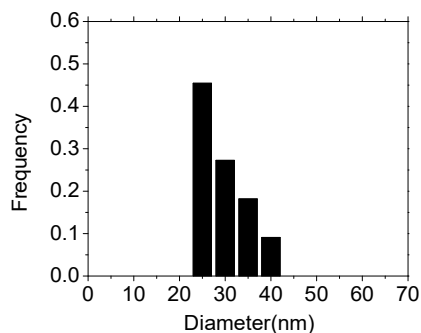


Figure 3.12. Hydrodynamic size of  $R_{Fe,i} = 0.2$  NPs measured by NTA.

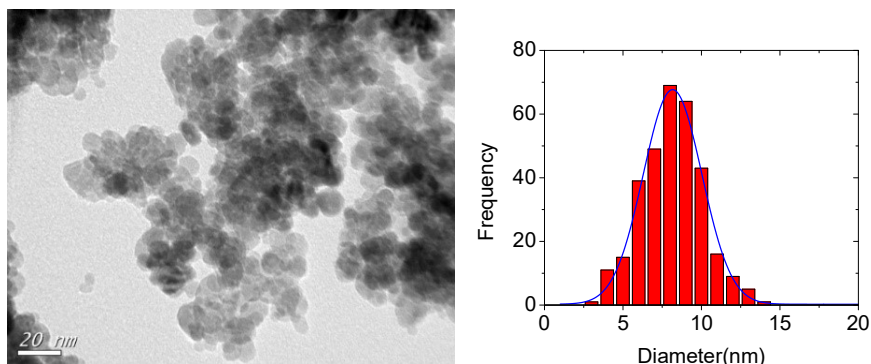


Figure 3.13. TEM image and size distribution of  $R_{Fe,i} = 0.2$  NPs.

Hydrodynamic size is much greater than result by TEM but it is an expected value. The hydrodynamic size always bigger than the size by TEM. Because there are electric dipole layers outside the NPs.

We now compare the results we obtained with NTA and DLS on CMP-NPs in water.

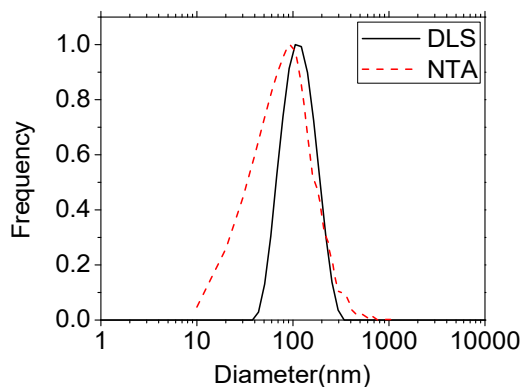


Figure 3.14. Hydrodynamic size of CMP-NPs measured by NTA and DLS.

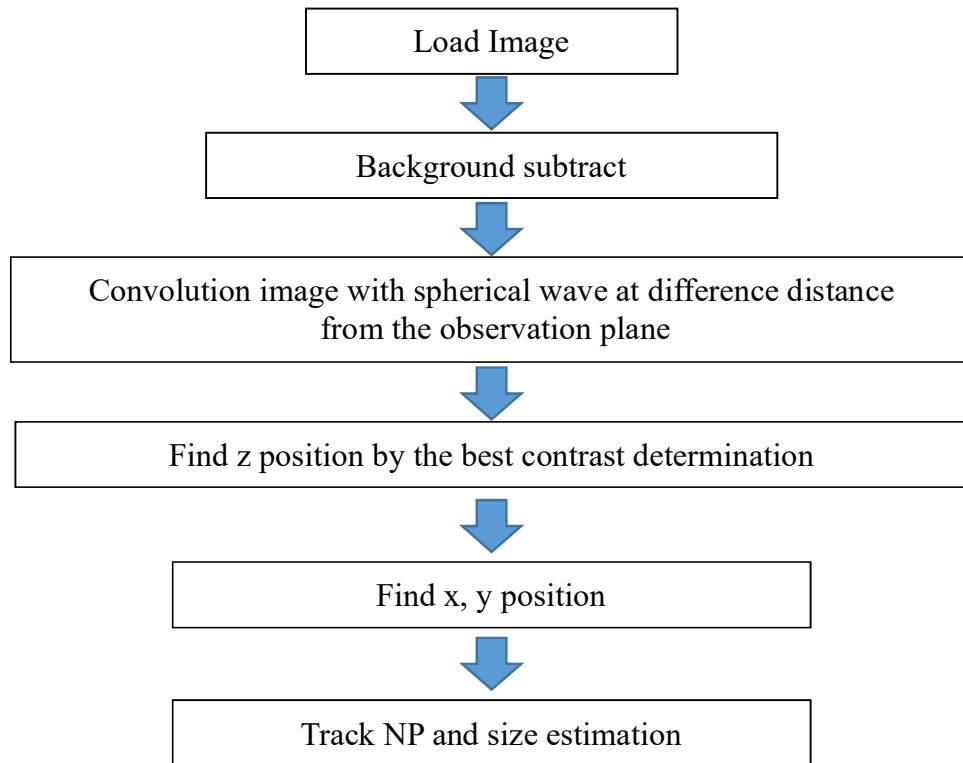
Hydrodynamic size of NPs measured by NTA is in good agreement with the size given by the DLS method (see Figure 3.14). Nanoparticle tracking analysis is therefore a valuable tool for characterizing nanoparticle suspensions. In our setup, we found that this technique could be used for analyzing NPs as small as 30 nm. A homemade program for tracking and analyzing sizes in real time has been developed.

### **3.2.2. Dark field interference microscopy for 3D NPs tracking**

We tried to develop three-dimensional (3D) single-particle tracking methods which could provide fully resolved movement of NPs in their medium. Some of them are based on multifocal scanning [153, 154], calculation of radial symmetry centers [155, 156]. All of them have some limited range along the z axis ( $<5 \mu\text{m}$ ) because of the expanding Point Spread Function (PSF).

Some kind of hologram microscopes have been developed in order to achieve high resolution ( $3 \times 3 \times 10\text{nm}$ ) and a better range on the z axis (up to  $30 \mu\text{m}$ ) [157].

Herein, we present a dark field interference microscope we developed, which can track NPs with high resolution and range of z axis is up to  $100 \mu\text{m}$ . The algorithm we wrote is able to locate NPs in 3D with a single image.

**Image processing**

*Figure 3.15. Flow-charts for 3d NPs tracking analysis.*

We record with the EMCCD camera images of NPs moving in suspension. As previously explained, each image is then background subtracted. Then the positions of the nanoparticles are determined following the flow chart (Figure 3.15). With a sequence of positions data, the diffusion coefficient and sizes of the particles are then estimated.

### ***Background subtraction***

The background can be determined as the image of the reference beam. The result of background subtraction is shown in Figure 3.16.

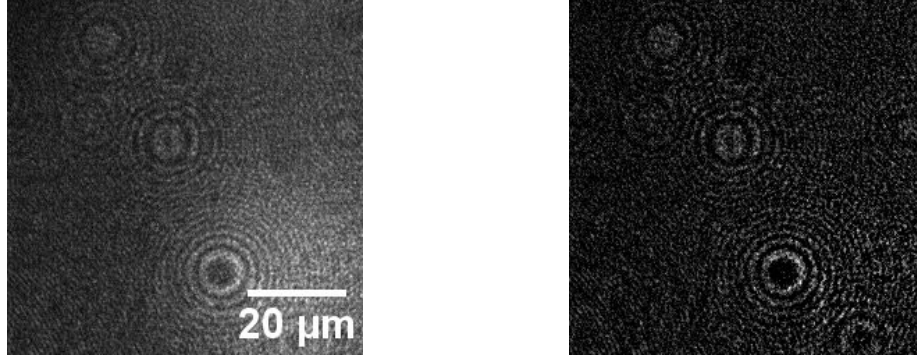


Figure 3.16. Dark field interference image before (left) and after (right) background subtraction.

### ***Image convolution***

From the interference image, the 3D location of NPs can be calculated by the following steps:

Step 1: Simulate the complex spherical wave at distance  $z$  from the observation plane.

$$\Psi(z) = \frac{e^{ikr}}{r} \quad (3.6)$$

where:  $r = \sqrt{(x - x_0)^2 + (y - y_0)^2 + (z - z_0)^2}$ ,

$k = \frac{2\pi}{\lambda}$  is the wavenumber.

Step 2: Compute 2-D fast Fourier transform (fft2) of spherical wave  $\Psi$  and Image IM recorded by EMCCD

$$\text{TF}\Psi = \text{fft2}(\Psi) \quad (3.7)$$

$$\text{TFIM} = \text{fft2}(\text{IM}) \quad (3.8)$$

Step 3: Convolve image with different planes at different distances from the objective focal plane ( $z$ )

$$\text{Co}(z) = \text{ifft2}(\text{TFIM} * \text{TF}\Psi(z)) \quad (3.9)$$

The intensity (I) of convolution image is calculated as follows:

$$I(z) = \text{Co}(z) \cdot \text{conj}(\text{Co}(z)) \quad (3.10)$$

Step 4: By scanning  $z$  value of the complex spherical wave, the position  $z$  of NPs is the value that gives the best contrast on the convolution image. The contrast of image is calculated as following:

$$\text{Contrast} = \frac{I_{\max} - I_{\min}}{I_{\text{avg}}} \quad (3.11)$$

Where:  $I_{\max}$  is the maximum value of image

$I_{\min}$  is the minimum value of image

$I_{\text{avg}}$  is the average value of image

The accuracy of 3D location algorithm is described in Appendix L.

## Results and discussion

### *Vertical limit*

In order to find the vertical limit of interference microscopy, the NPs were fixed on the glass slide. The maximum for the depth  $z$  is determined by the longest distance from focus plane to NPs which can be observed by the EMCCD. Figure 3.17 shows a NP at different distances from the focus plane, which gradually increase from the left to the right of the image.

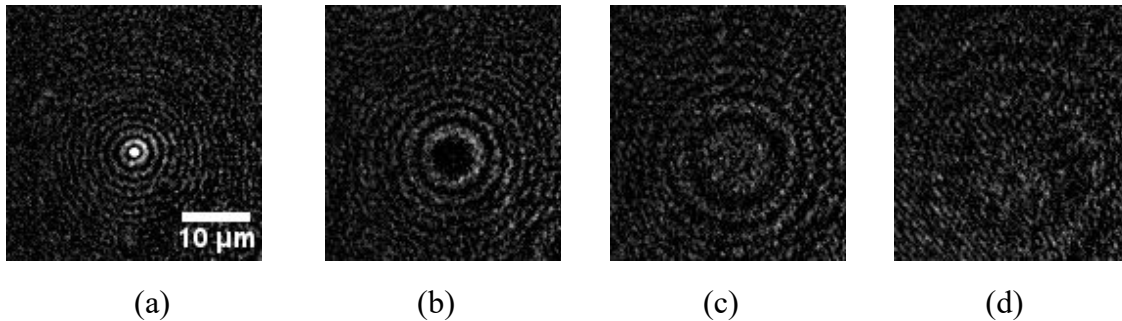


Figure 3.17. Interference images of NP as a function of  $z$ :  $0 \mu\text{m}$  (a),  $20 \mu\text{m}$  (b),  $40 \mu\text{m}$  (c), and  $100 \mu\text{m}$  (d).

From an interference image, the position of a NP can be estimated by using the image correction algorithm. For instance the reconstruction, with different values of  $z$ , of images from data of Figure 3.17d is described in Figure 3.18.

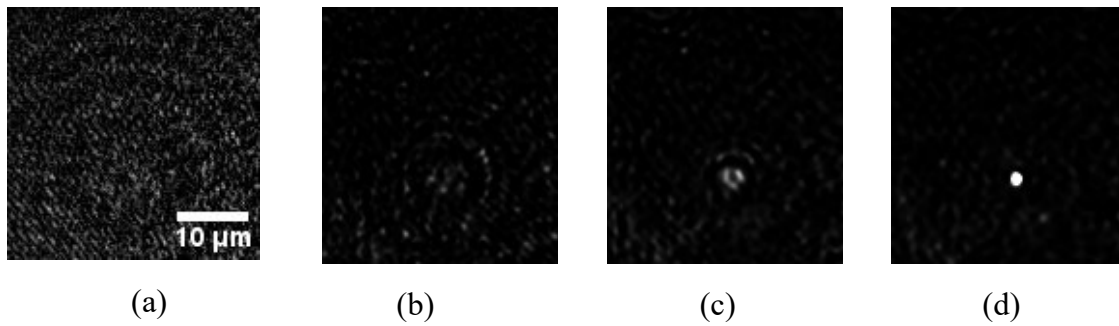


Figure 3.18. Original interference image (a) and its reconstruction images at different depths  $z$ :  $70 \mu\text{m}$  (b),  $80 \mu\text{m}$  (c), and  $95 \mu\text{m}$  (d).

After calculating a suitable value for  $z$  by determining the best contrast of the test images, the location  $x$  and  $y$  of NP can be calculated by the 2D Gaussian fitting method or the center of mass method.

Figure 3.19 shows contrast of reconstructed images as a function of  $z$ . The further the distance, the lower contrast we have on the interference rings. In this experiment, the results show that the longest distance from focus plane to the NPs we can track at this time is about  $100 \mu\text{m}$ . Farther than that, the interference rings are not strong enough for reconstruction.

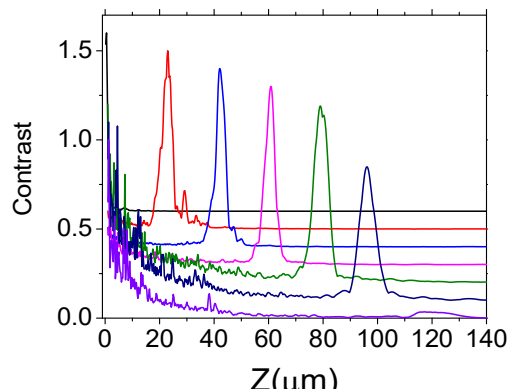
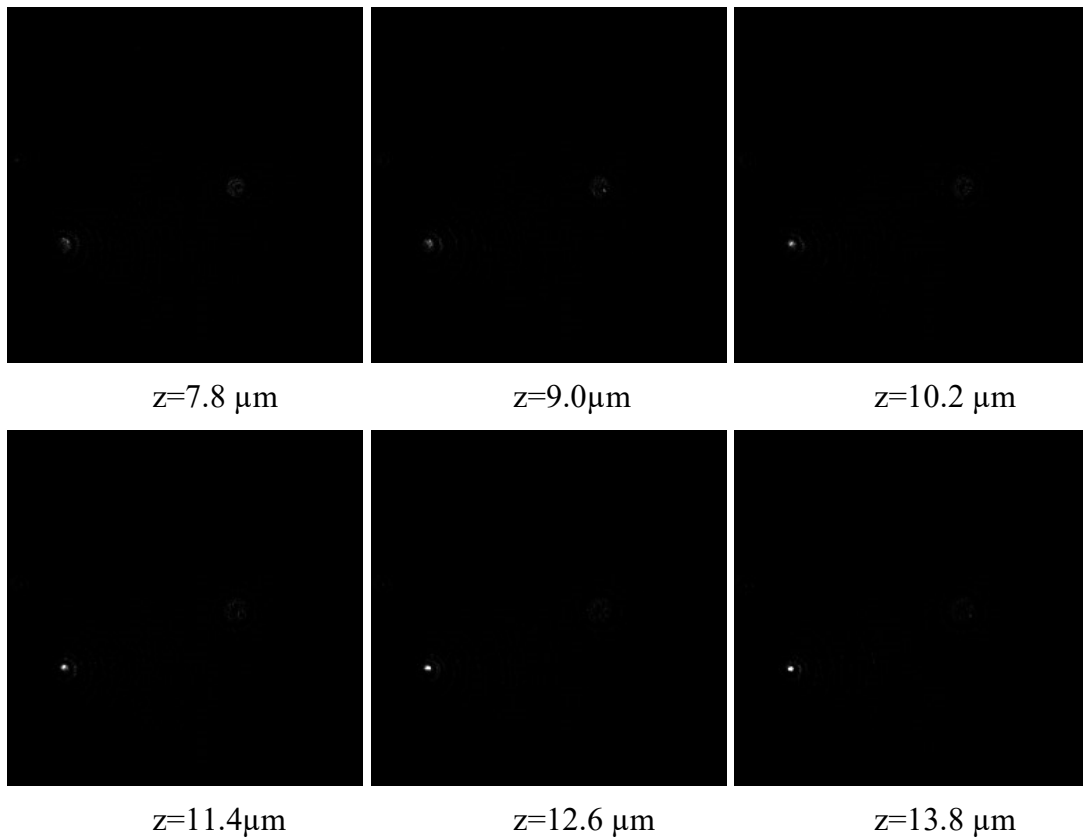


Figure 3.19. Contrast of reconstruct image versus  $z$ .

Figure 3.20 shows the use of a Gaussian fitting for better location. FWHM of the peak indicates that the resolution of  $Z$ -axis is approximately  $5 \mu\text{m}$ .





*Figure 3.21. Reconstruction image versus  $z$ .*

The interference images of moving uncoated NPs are convoluted with spherical wave with different depths  $z$  to get convolution images. From convolution images, the best value of  $z$  can be obtained from the image with the strongest contrast, where the NP's rings are converted into a single point, allowing 2D Gaussian fitting for super  $x, y$  resolution. Figure 3.21 shows convolution images of NPs in water with different  $z$  values. Using interference microscopy, the Brownian movement of NPs can be located in 3D.

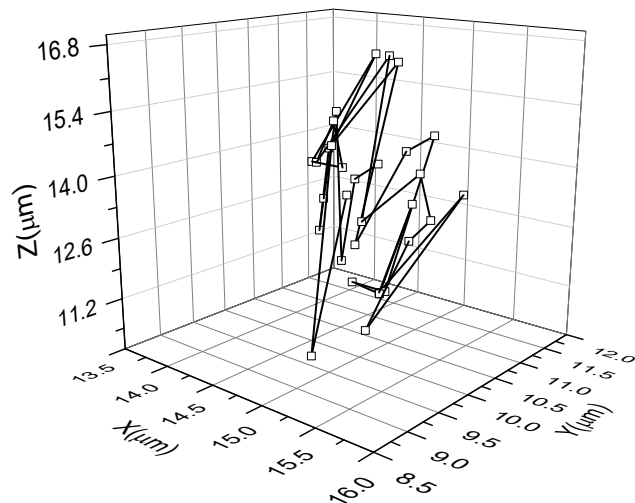


Figure 3.22. Brownian movement of NP in medium.

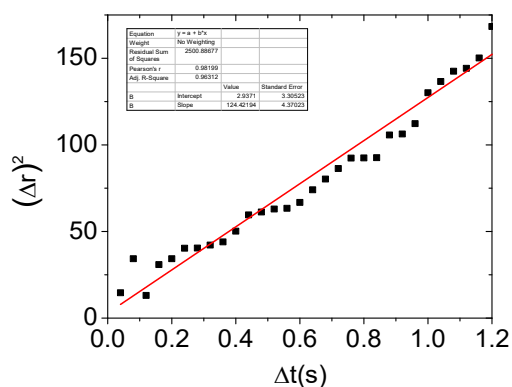


Figure 3.23. The diffusion coefficient estimation.

Brownian movement of NP in medium and the diffusion coefficient estimation are shown in Figure 3.22 and Figure 3.23. According to the Stokes-Einstein equation for the diffusion coefficient, the diameter of these NPs is about 22 nm. We have shown a dark field interference microscope is a useful tool for characterizing and tracking nanoparticle in suspensions. The technique can be used for tracking NPs as small as 20 nm in solution. For further studies, we expect that the nanoparticles, attached on with drugs or a biological label, which move in animal tissue, could be seen and could be tracked with our dark field interference microscope.

### 3.2.3. Dark field hyperspectral microscopy for locating NPs

#### Image processing

The most common algorithm used in hyperspectral imaging is the spectral angle mapper (SAM). SAM attempts to obtain the angles formed between the reference spectrum and the image spectrum, treating them as vectors in a space with dimensionality equal to the number of bands [158].

The angle  $\alpha$  between spectrum of each pixel in raw image and reference spectra is calculated by the equation 3.12:

$$\alpha = \cos^{-1} \left[ \frac{\sum_{i=1}^{nb} t_i r_i}{\sqrt{(\sum_{i=1}^{nb} t_i^2)} \sqrt{(\sum_{i=1}^{nb} r_i^2)}} \right] \quad (3.12)$$

where  $nb$ : number of bands in the image.

$r$ : reference spectrum

$t$ : spectrum of each pixel

This angle is a convenient way to express similarity or difference between optical spectra as a scalar value. In signal processing terms, it can be seen as a signal recognition process with a kind of fuzzy logic.

#### Results

We construct a synthetic image of the sample based on the spectral angle between each pixel spectrum and the reference spectrum, the latter being recorded on a known NP in the sample. The improvement of contrast can be seen clearly when comparing images obtained by dark field hyperspectral microscopy and conventional dark field microscopy.

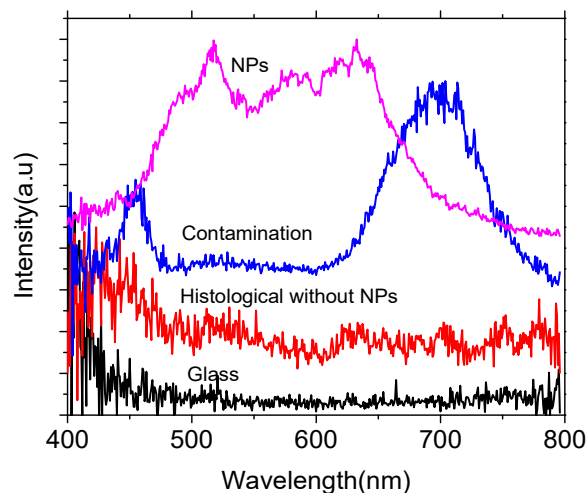


Figure 3.24. Reflection spectra of four materials present in a slice.

The intensity in the image obtained by dark field hyperspectral microscopy indicates the angle between the spectrum of that pixel and the reference spectrum. A bright pixel gets a small angle, corresponding to a good similarity to the reference spectrum, whereas a dark pixel has a large angle.

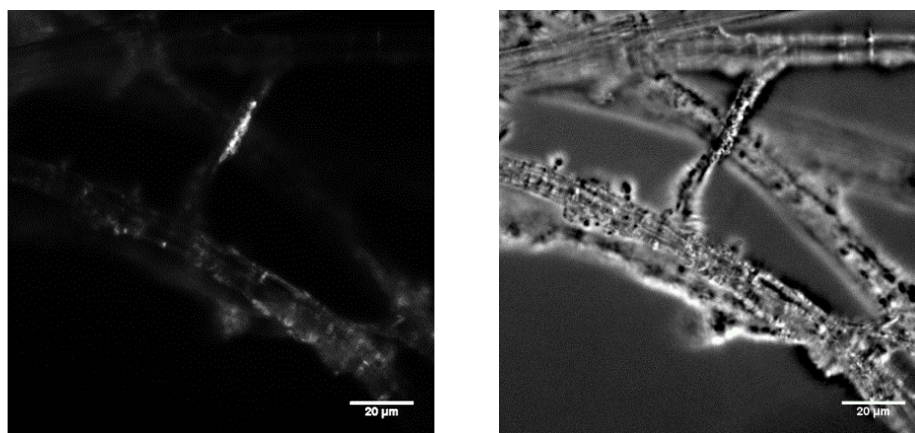


Figure 3.25. Image of histological sample exposed to nanoparticles obtained by conventional dark field (left) microscopy and dark field hyperspectral (right) microscopy.

In Figure 3.25, the image obtained by our dark field hyperspectral microscope indicates that the NPs are covering the surface of the histological sample. Some dark point bound to the histological sample comes from some unknown contamination. All these details are very difficult to observe by conventional dark field microscopy. We can distinguish different kinds of NPs, or some kinds of their properties, by selecting those possessing a suitable angle  $\alpha$  (Figure 3.26).

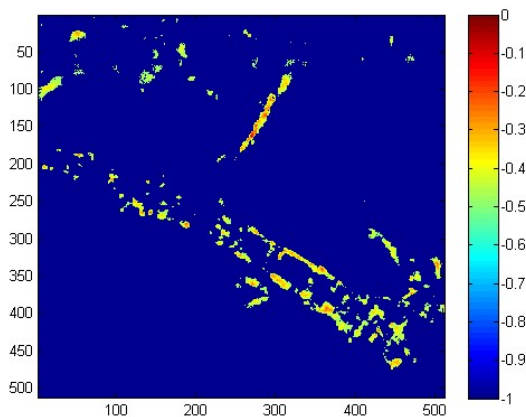


Figure 3.26. NPs in histological slices can be located by using suitable angle  $\alpha$ .

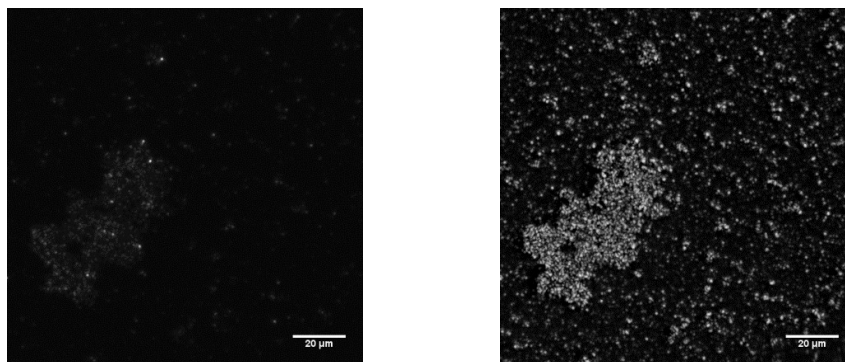


Figure 3.27. Image of NPs obtained via conventional dark field (left) microscopy and dark field hyperspectral (right) microscopy.

In Figure 3.27, the results show the improvement we can get for the image's contrast from a dark field hyperspectral microscope. This image obtained via dark field hyperspectral microscopy shows that this technique can detect the small NPs that cannot be detected by a conventional dark field microscope. With dark field hyperspectral microscopy, a single nanoparticle can be detected in a complex environment.

### 3.1. Conclusion

The combination of hyperspectral imaging and dark field microscopy made a new powerful tool, providing images with better contrast and higher signal-to-noise ratio than images obtained by conventional dark field microscopy. This combination can be used for locating NPs, tracking NPs, size estimation of NPs in liquid medium and histological tissues.

## Chapter 4. Imaging

In this chapter we present imaging experiments with NPs we have prepared in chapter two. NPs have been injected in a rat model of atherothrombosis formerly used in the laboratory [159, 160, 34]. The model is described in the experimental part below. We used fuco-0.5, CMD-0.5 and PEG-coated NPs-0.5 (namely PEG-0.5, see Appendix D). MRI allowed the localization of the diseased areas which were harvested after the sacrifice of the animals and histological sections were prepared for further optical imaging.

### 4.1. MRI

#### 4.1.1. Materials and methods

##### Animal model

A total of 12 male 7-week-old Wistar rats from CERJ (Le Genest, France) were prepared. To localize the treated segment during the MRI session, the distances between the upper and lower points of the perfused segment and the origin of the left renal artery were measured with the microscope eyepiece, and surgical wounds were closed. This model is characterized by the presence of an intra-luminal thrombus 1-3 weeks after aneurysm induction. In order to increase the size and the activity of the aneurysmal thrombus, injections of *Porphyromonas gingivalis* have been performed at day 8 and day 16.

##### MRI session

Rats were anesthetized with isoflurane before injection of the NPs in the vein of the penis. They were scanned with a 7 T small animal MRI (Bruker, Germany) before and after injection using a dedicated coil.

For black-blood high resolution imaging of the aortic vessel wall, a T<sub>2</sub> sequence with cardiac gating was used with the following parameter: minimum TR = 600 ms, TE = 8 ms, FOV= 5 cm and a matrix size of 256 x 256. Continuous slices (slice thickness = 1 mm) were made under the renal aorta bifurcation. Image analysis was performed using OsiriX software (DICOM reader v3.7). Maximum luminal narrowing was quantified by the percentage reduction ( $\Delta R\%$ ) of aortic luminal area as previously published [69]. Arterial wall contrast agent uptake analysis was performed on slices that corresponded to histological sections.

Intraluminal areas that evidenced visual intraluminal hypersignal from 30 min to 1 hour after injection of contrast agent were manually contoured for quantitative signal analysis. Regions of interest were pasted on all corresponding MR images. The signal-to-noise ratio (SNR) of aortic wall thrombus was measured by calculating the average signal intensity in the region of interest from MR images at each imaging point ( $SNR = [SI_{aortic\ wall} - SI_{muscle}] / SD_{noise\ signal}$ ). Normalized signal enhancement ( $\Delta NSE\% = (SNR_t - SNR_{before}) / SNR_{before} \times 100$ ) was calculated at 10, 30, 50, 75, 100 and 125 min after injection and analyses were performed between each scan time. At the end of the session, animals were sacrificed and the perfused portion of the aorta, including the dilatation, was harvested and flushed with PBS. Then the aorta was cut transversally into 2-mm width tissue rings which were frozen at  $-20^{\circ}C$  in cold isopentane. Healthy artery parts were used as standard samples.

### **PERLs staining**

Perls' iron staining was performed by incubating some histological sections (two of them) in a mixture containing equal ratio of 2% hydrochloric acid and 2% potassium ferrocyanide for 20 min, followed by counterstaining with nuclear fast red. Deposits of iron were stained as blue by Perl's Prussian blue staining, while cytoplasm and cellular nucleus were stained as pink and red, respectively.

### **4.1.2. Results and discussion**

In vivo MR imaging experiments were performed with fuco-0.50, CMD-0.50 and PEG-0.50, the two latter being considered as reference compounds devoid of biospecificity. The difference of MRI images between before and after injection with fuco-NPs was clear, appearing as a contrasted black area (see red circle on Figure 4.1). Fuco-NPs were likely linked to the thrombus through an interaction with P-selectin overexpressed by aggregated platelets [161]. As expected, CMD-NPs did not induce a contrast enhancement (figure 4.2). To confirm the active targeting of fuco-NPs, the third rat was injected with a same amount of CMD-NPs and fuco-NPs. In the first step, the rat was injected CMD-NPs. Two hours after CMD-coated NPs injection, the atherothrombosis area was not darkened on MR images. In the next step, fuco-NPs were injected into the rat. In MR images, atherothrombosis can be detected as dark areas because of the interaction between fucoidan and P-selectin. Figure 4.3 shows the mean value of MR signal on the diseased area (red

circle on figure 4.1 and 4.2), versus time after CMD-coated NPs and fucoidan-coated-NPs injection. The MR signal was nearly constant after CMD-coated NPs injection but it decreased fast after fucoidan-coated-NPs injection.

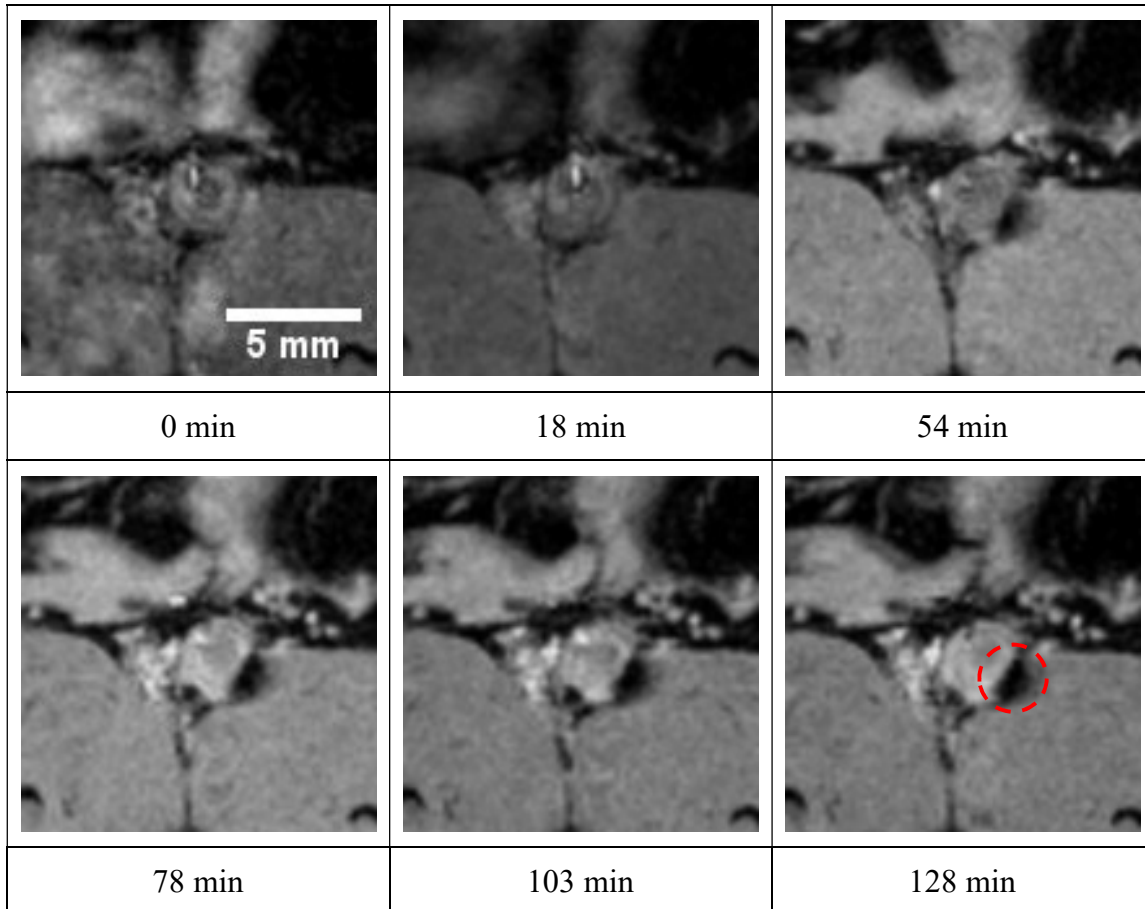


Figure 4.1. MRI of atherothrombosis after fuco-NPs injection.

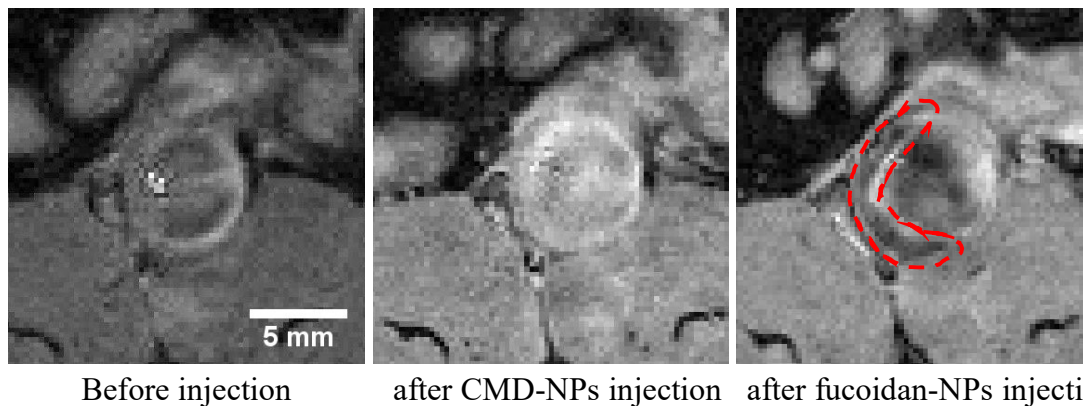


Figure 4.2. MRI of atherothrombosis after CMD-coated NPs and fucoidan-coated NPs injection.

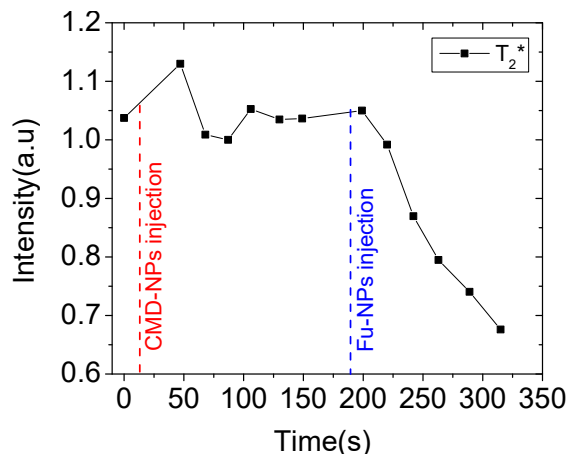


Figure 4.3. MR signal versus time after CMD-coated and fucoidan-coated NPs injection on  $T_2^*$  weighted MRI images.

PEG-coated NPs did not bear fucoidan but surprisingly, we observed the same behaviour as with fuco-NPs (figure 4.4). Indeed, two hours after injection, the concentration of PEG-NPs reached a maximum level, corresponding to a minimum of the MR signal as for fuco-NPs (figure 4.5). The difference in behaviour with CMD-NPs could not be explained by the only passive diffusion effect (Enhanced Permeation and Retention Effect) of the NPs [162, 163] since CMD-NPs which are similar in size to PEG-NPs did not induce a contrast enhancement. However the zeta-potential of PEG-coated NPs (-8.4 mV, see appendix G) was not so negative that the NPs could be quickly taken up by diseased tissues which cells have negative surface charge [164, 165, 166]. Because CMD-NPs have zeta-potential of -33.3 mV which was high enough to avoid absorption by the thrombus they were not expected to link to the thrombus.

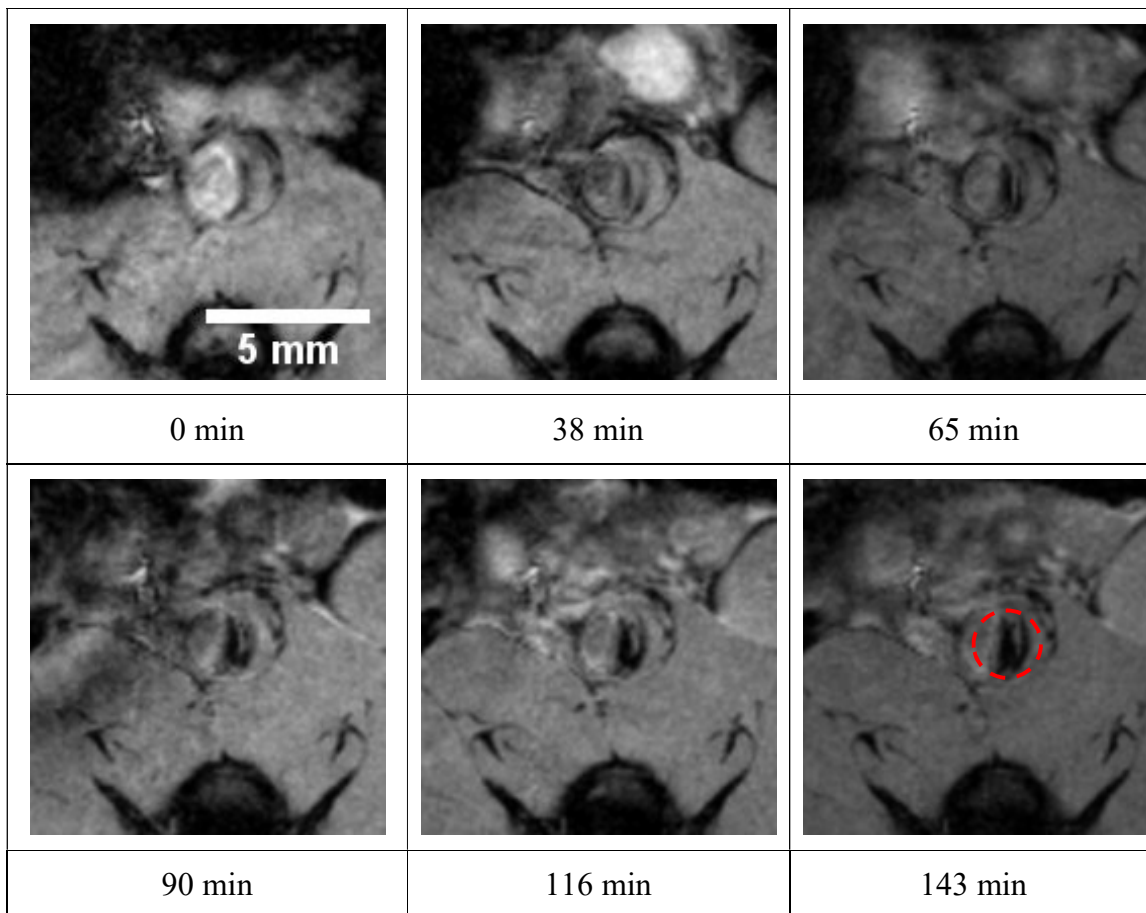


Figure 4.4. MRI of atherosclerosis after PEG-NPs injection.

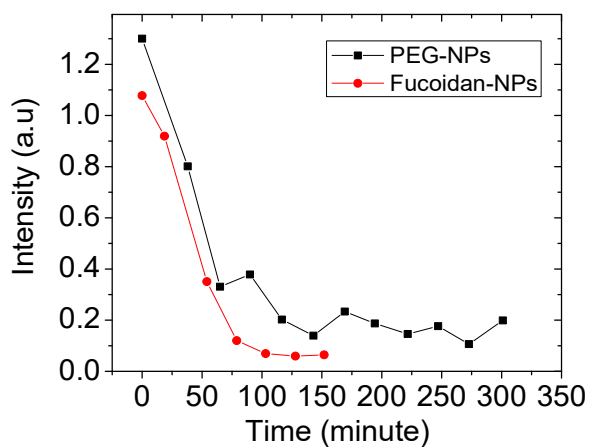


Figure 4.5. MR signal after NPs injection versus time.

All these results demonstrated the capability of Zn(Fe)O-based fucoidan-coated NPs to be used as a contrast agent biospecific of atherosclerosis.

## 4.2. Optical imaging

Structure of a healthy vessel and vessel with atherothrombosis were imaged by brightfield microscopy, dark field microscopy, hyperspectral microscopy, fluorescent microscopy, second-harmonic imaging microscopy and differential interference contrast microscopy. Each microscopy method gave some specific information about the structure of the atherothrombosis and the vessel.

### 4.2.1. Perls' Prussian Blue Staining

Perls' Prussian Blue Staining was performed on some histological slices of diseased tissues from animals which have been injected with fucoidan-coated NPs. The

Figure 4.2 evidenced the presence of NPs since Perls' reaction allows to colour iron ions (blue dots). This method can provide a proof of the presence of aggregated NPs. This is not a sensitive method, and it cannot be used to detect single NP.

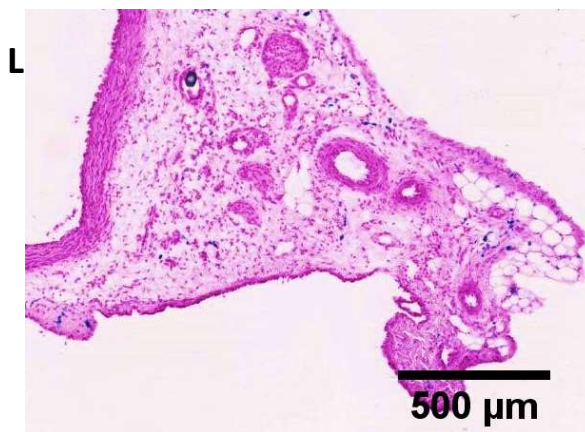


*Figure 4.2. Iron distribution (blue dots) in vessel wall. L = lumen of the vessel.*

### 4.2.2. Healthy vessel and diseased vessel

We compared images of a healthy vessel without atherothrombosis and a diseased vessel. Bright field and dark field imaging showed the difference of them. In autofluorescence images (Figure 4.5), the bright area inside the vessel wall, could evidence collagen, which has a strong fluorescence emission [171].

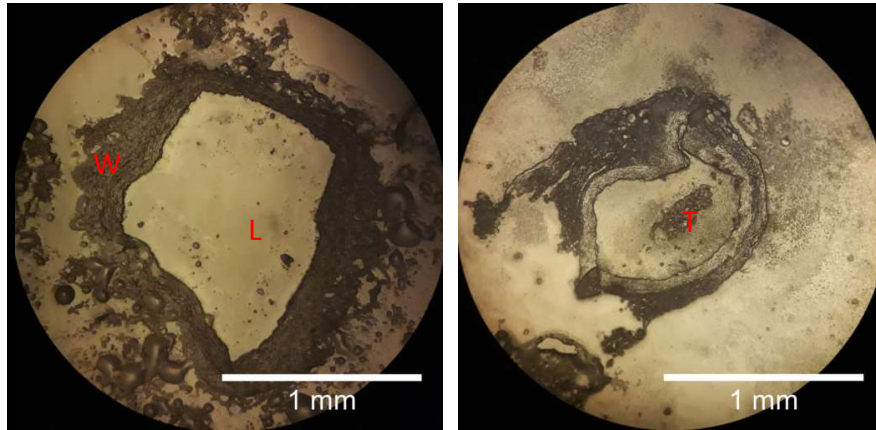


Figure 4.3. Bright field imaging of a healthy vessel (left) and a diseased vessel (right),  
*W= Wall; L=Lumen; T=Thrombosis.*

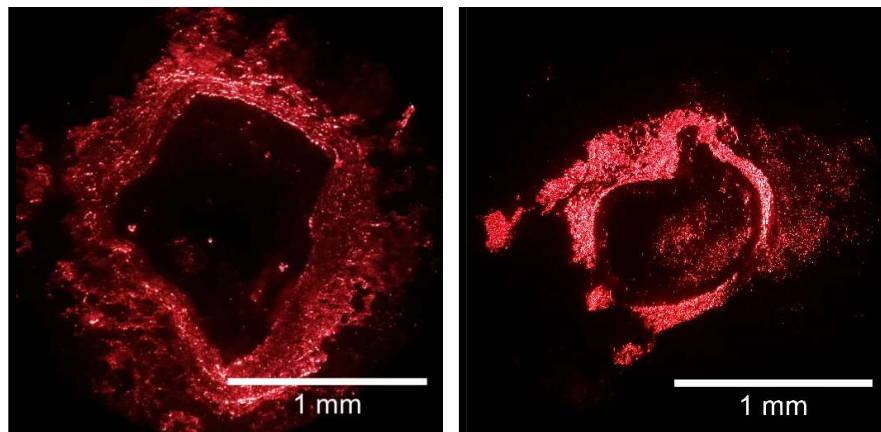


Figure 4.4. Dark field imaging of a healthy vessel (left) and a diseased vessel (right).

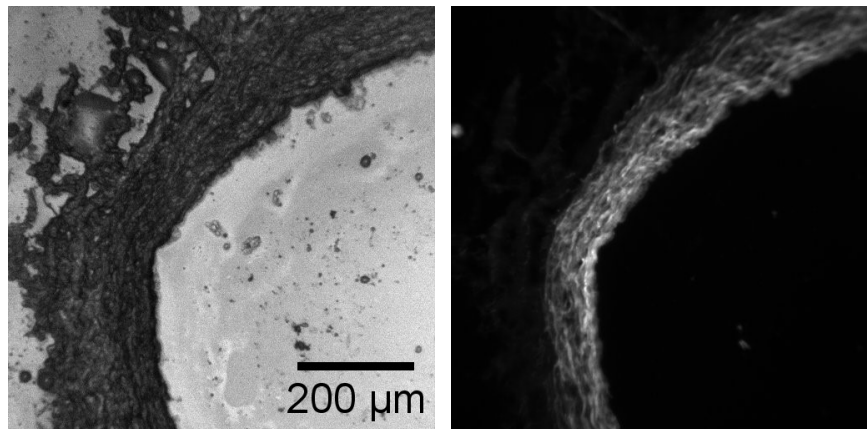


Figure 4.5. Bright field imaging (left) and fluorescence imaging (right) of a healthy vessel.

## 4.2.3. Images of atherothrombosis

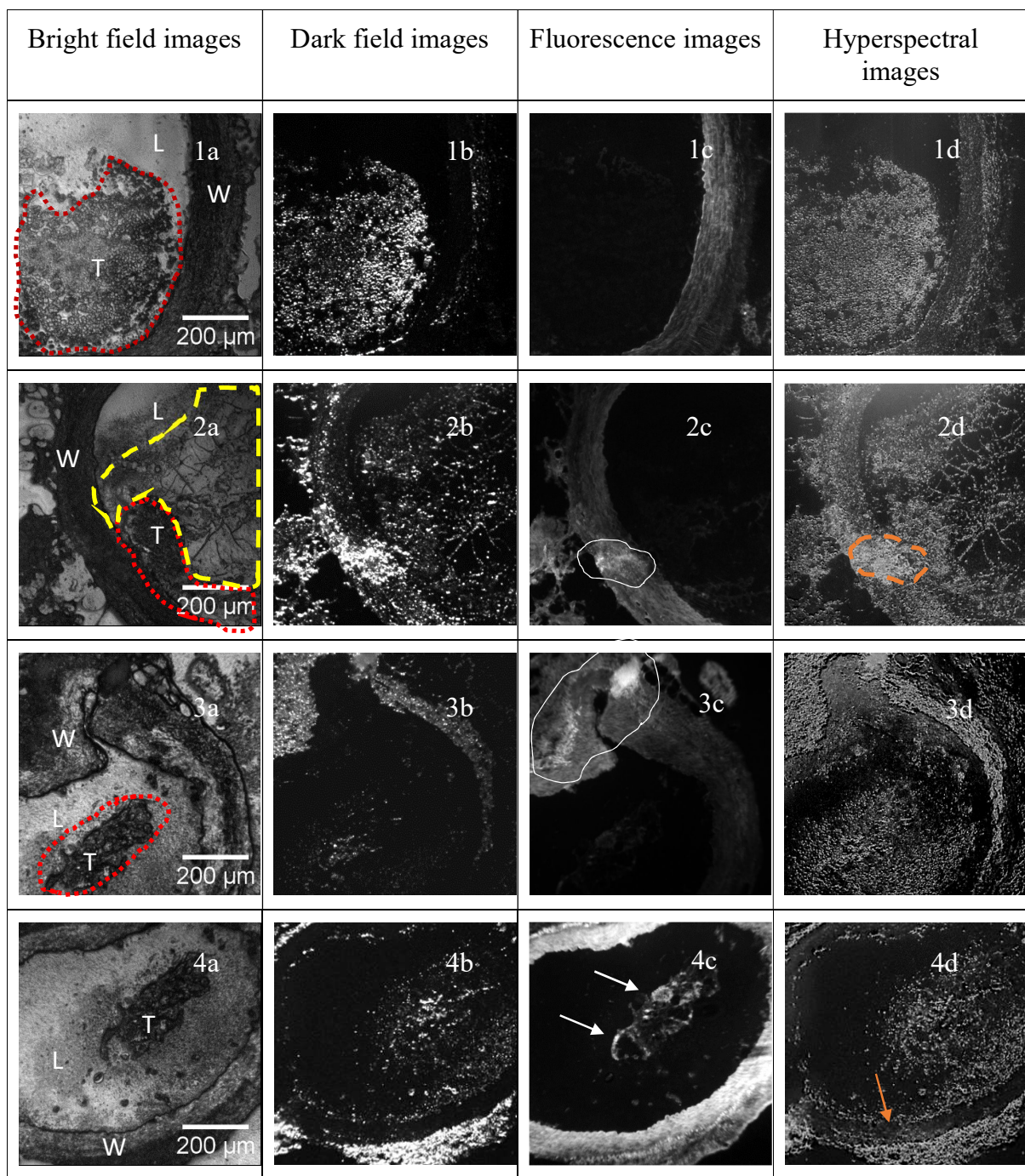


Figure 4.6. Bright field, dark field, fluorescence, hyperspectral images of atherothrombosis. The dotted lines encircle diseased areas, the yellow dash line could be fibrin, the white plain lines can be collagen fragments, and the white arrow is probably NPs, W= Wall; L= Lumen; T=Thrombosis.

While using bright field microscopy, we investigated histological structure of the tissue. The diseased areas are marked with a red-dotted line within a high density of blood

tissue. Fibrin rich area could be encircled by the yellow dash line as a sign of early atherothrombosis development (Figure 4.6.1a, 2a, 3a).

Dark field microscopy is also suitable to investigate structure of the tissue. Because the very high contrast of this method, dots could be detected whereas they could not be seen in bright field microscopy. The dots could be clusters of NPs or cell nucleus, which were both strongly scattering under laser light (Figure 4.8, Figure 4.6.1b, 2b, 4b).

Because fluorescence of NPs was weaker than that of tissues, the distribution of NPs in the histological tissues was rather difficult to obtain. However, autofluorescence images could detect weak points of the vessel or an inflammation area where one could find a high concentration of collagen fragments. Collagen fragments were strong fluorophores, so they could easily be seen on the fluorescence image (white plain line in Figure 4.6.2c, 3c).

In the fluorescence image of atherothrombosis, some bright area could be seen (white arrows in Figure 4.6.4c) as large concentrations of NPs. The total intensity was rather weak, but we could still distinguish something different from the neighbouring autofluorescence.

With hyperspectral microscopy, the image of atherothrombosis had a better contrast, and gave clues about different materials in the samples by analyzing the signal of tissue. The weak point of the vessel (orange dash line in Figure 4.6.2d) could be seen clearly by hyperspectral imaging. We could see different structures of the vessels and the atherothrombosis which could not be obtained by bright field images (orange dash line in Figure 4.6.2d, orange arrow in Figure 4.6.4d).

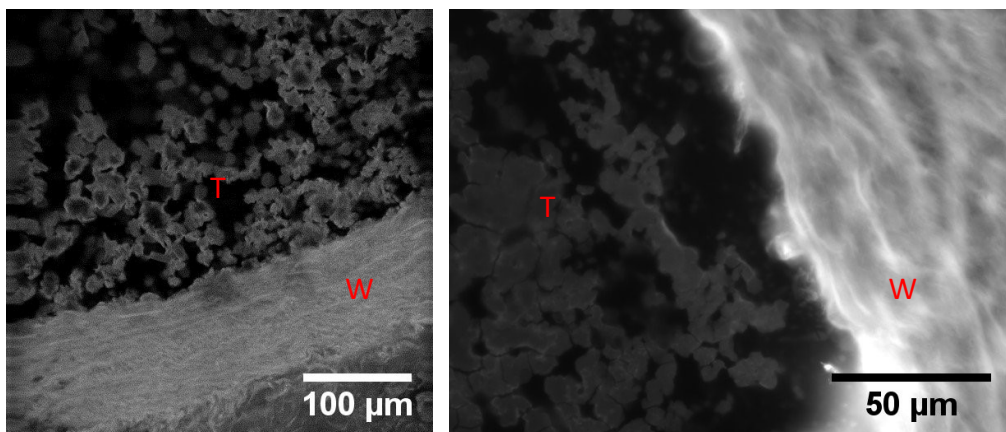
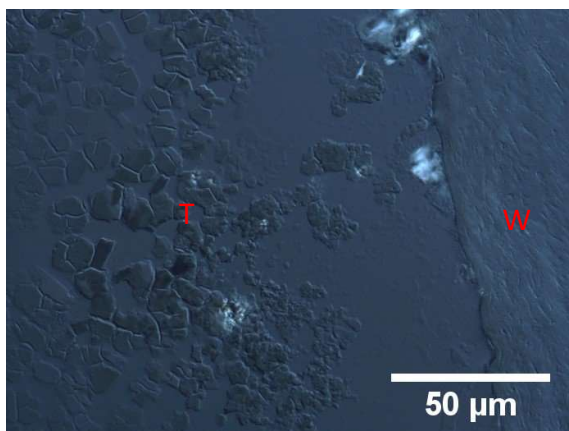


Figure 4.7. Second-harmonic images of atherothrombosis, W= Wall; T=Thrombosis.

To finish with, we also tested other imaging modalities in collaboration with the team of Marie-Claire Schanne-Klein at *Laboratoire d'Optique Biomédicale* (LOB), Ecole Polytechnique. We thus imaged samples with second-harmonic imaging microscopy (SHIM) and differential interference contrast (DIC) microscopy. Atherothrombosis could be clearly imaged. However NPs could not be evidenced because of strong autofluorescence of tissues and weak emission from NPs (Figure 4.7, Figure 4.8).



*Figure 4.8. DIC image of atherothrombosis, W= Wall; T=Thrombosis.*

### 4.3. Conclusion

The difference of MRI images between before and after injection with fuco-NPs and CMD- NPs, as a reference, confirmed that fuco-NPs were good  $T_2$  contrast agents. Although devoided of biospecificity, PEG--NPs behave as fuco- NPs, and we have no clear explanation to propose. Many different optical modalities were used to detect NPs in atherothrombosis but all the experiments did not succeed. The main reason was the weak fluorescence of NPs as compared to the strong autofluorescence of tissue. Because the NPs were interspersed among the tissue, so we could not distinguish signals from them.

In table Table 4.1, we compare all the optical imaging method we used. The ability to allow the detection of NPs and the main drawbacks are shown. Dark field, hyperspectral, fluorescence spectroscopy were able to detect NPs. However, equipment and software must be improved to get more relevant results. Eventually, according to my opinion, fluorescence remains the best tool for NPs detection.

Table 4.1. Comparing optical imaging method

	Bright field	Dark field	Hyperspectral	Fluorescence
Contrast	Low	High	High	High
Additional hardware	No	External light sources	Monochromator External light sources	Laser Filters
Additional Software	No	No	Yes	No
Speed	Real-time	Real-time	Non real-time	Real-time
Additional Labeling	No	No	No	Yes
Ability to detect NPs	No	Yes	Yes	Yes

## General discussion

The early diagnosis of atherothrombosis with clinical imaging would allow both a most suitable follow-up and the establishment of appropriate therapeutic strategies. Nowadays, the field boasts a plethora of nanoparticulate systems to improve the quality of the images (contrast agents) [172]. However, some key points must be addressed for the design of NPs for these purposes [173, 174]: (i) a hydrodynamic size below 100nm and a size distribution as narrow as possible due to the fundamental size dependent properties of NPs, (ii) good dispersion, stability and biocompatibility by means of robust hydrophilic coatings that induce a strong steric repulsion between NPs to extend the residence time in circulating blood and to limit endocytosis by macrophages, (iii) the specificity for the intended target. In parallel, the development of multimodal clinical imaging systems (for example PET/MRI and SPECT/CT) would improve diagnostic and the understanding of cell-scale and even molecular-scale events through high quality images in terms of sensitivity and resolution. Finally, the coupling of nanosystems with ligands of pathological biomarkers would considerably improve their action by limiting the side effects.

For the last 20 years some studies focused on the preparation ZnO-based NPs due to unique magneto-optic properties [1, 175, 176, 177, 178, 179] which were very attracting for biomedical applications [3, 180, 181, 182, 183]. In our study, we prepared Zn(Fe)O NPs combining fluorescent and magnetic properties in the same core [1, 2, 179, 184, 114] which were coated with fucoidan in order to perform bimodal magnetic resonance and optical imaging of atherothrombosis. Our main objective was thus to develop optical imaging protocols for the observation of the nanoparticles on tissue slices in order to further link their localization and their “behaviour” to the biological pathological environment. This was done in the continuity of the works of Nguyen Trong Nghia published in Journal of Biomedical Optics in 2017 [111].

We have performed numerous experiments to get inorganic nanocrystals endowed with the required properties, which efficient and easy obtainment remains a challenge [185, 111]. NPs have been quantitatively obtained from zinc acetate and iron acetate mixture in diethylene glycol with  $R_{Fe}=Fe/(Zn+Fe)$  (mol/mol) ranging from 0.05 up to 0.5 by a novel azeotropic method using toluene to remove water from the reaction mixture. The azeotropic

method allowed the formation of high crystalline quality nanocrystals with narrow polydispersity and size ranging from about 3 to 8 nm, much smaller than in previous studies with the presence of water in the reaction medium [3, 125, 126, 124, 127]. XRD evidenced high doping levels of wurtzite ZnO phase with iron ions up to  $R_{Fe}=0.35$  [186, 2] (namely DEG-0.35). However, NPs prepared with  $R_{Fe}=0.5$  (namely  $R_{Fe, I} = 0.5$ ) were corresponding to a mixture of nanocrystals of same size made of wurtzite phase (45% w/w) and spinel cubic phase (55% w/w), the latter likely corresponding to the formation of  $ZnFe_2O_4$  [144, 114, 146].  $R_{Fe, I} = 0.5$  NPs were coated with carboxymethyl dextran (CMD-0.5) and fucoidan (fuco-0.5) for further animal experiments; fucoidan was recently used as a molecular ligand in for SPECT imaging and MRI of atherothrombosis and heart ischemia [160, 34, 35, 161]. Coated NPs had size on the hundreds of nanometer scale and negative charge surface evidencing the coating with the anionic polymers. They were ferromagnetic with saturation magnetizations of about 22-25 emu/gram and were evidenced as  $T_2$  MR contrast agents. When excited at 370 nm, they exhibited a broad fluorescence emission at about 470 nm.

The animal experiments showed that fuco-NPs could be used as MR contrast agent for imaging atherothrombosis. Indeed, two hours after injection, a maximum contrast was obtained which was attributed to the interaction of fuco-NPs with P-selectin overexpressed by aggregated activated platelets [161, 34]. indicating that Zn(Fe)O-based NPs have the potential to be effective  $T_2$  contrast agents

The dark field microscopy allowed us to locate NPs, tracking their movements, estimate their size in a liquid medium. Using 15 mW focused He-Ne laser and an ultra-low noise, highly sensitive EMCCD camera, the bare NPs with hydrodynamic diameter near 30 nm could be seen by dark field microscope. This is nearly the limit of this method (10 nm) [150]. Some other groups report NPs could be tracked at a size of 60 nm [187, 188]. The Brownian motion of NPs can be followed and the size of the NPs is estimated in real-time with our homemade software. NTA have already been reported in some publications, where NPs can be tracked in a cell, but the NPs size was rather big: 50-100 nm [189, 190].

We have developed a three-dimensional (3D) single-particle tracking system using dark field interference microscopy. We have a high resolution in x and y, and the scanning depth along z axis is up to 100  $\mu$ m. The precise location of NPs can be determined with single shot image by using a convolution image algorithm.

Dark field hyperspectral microscopy is also a very good tool for locating NPs in the histological tissue. It collects and processes information from electromagnetic spectrum of the images. By analyzing the spectrum of every pixel and comparing to the spectrum of reference materials, hyperspectral microscopy can detect the presence of nanomaterial on exposed tissue slices, locate, identify, and characterize them. The combination of hyperspectral imaging and dark-field microscopy made a new powerful tool providing images with better contrast and higher signal-to-noise ratio than images obtained by conventional dark field microscopy. A homemade dark field hyperspectral microscope was built and a program for analyzing data was studied and developed.

We have performed experiments on histological slices of harvested diseased vascular tissue from rats. Structures of a healthy vessel and a vessel with atherothrombosis were imaged by brightfield microscopy, dark field microscopy, hyperspectral microscopy, fluorescent microscopy, second-harmonic imaging microscopy and differential interference contrast microscopy.

Although we used high quality equipment such as a good microscope, a powerful 370 nm – 20 mW UV diode laser, an ultra-low noise EMCCD camera, and special filters, we found it was very difficult to identify reliably the NPs in the tissue.

## General conclusion and perspectives

Nanoparticles (NPs) containing iron and zinc oxide which could be used as bimodal Magnetic resonance imaging (MRI)/optical contrast agents were synthesized by polyol method. Many experiments with different iron concentrations have been performed in order to get NPs from zinc and iron salts in polyol medium. An azeotropic method was developed which allowed the formation of Zn(Fe)O nanocrystals with sizes ranging from about 3.5 to 8 nm and low dispersity, in good yields. XRD diffractogram showed the crystalline quality of NPs and evidenced a mixture of nanocrystals made of wurtzite and cubic phase for the highest iron content, although it was not possible to distinguish one from the other by TEM. Due to their magnetic properties, these NPs could be considered as contrast agents for MRI and they exhibited a large emission spectrum above 450 nm when excited at 370 nm.

Fucoidan-coated NPs and carboxymethyl dextran-coated NPs were injected in a rat model of atherothrombosis. MR images evidenced the uptake of fucoidan-coated NPs into the diseased areas which were harvested and examined as histological sections by optical imaging modalities.

In our study, different types of optical microscopies have been optimized with NPs in vitro before attempting their detection on histological sections of animal tissues. The structure of atherothrombosis was imaged by brightfield microscopy, dark field microscopy, hyperspectral microscopy, fluorescent microscopy, second-harmonic imaging microscopy and differential interference contrast microscopy. However, although we used good equipment such as a good microscope, a powerful 370 nm – 20 mW UV diode laser, an ultra-low noise EMCCD camera, and special filters, some promising area were found but the presence of NPs cannot be confidently asserted. The fluorescence of NPs was too weak as compared to that of tissues, a weakness which was magnified by the small size of the inorganic cores.

Nevertheless, the new azeotropic method we have used in this work has made it possible to easily and quantitatively produce nanoparticles whose magnetic and optical properties make them potential contrast agents for bimodal imaging using MRI and optical microscopies. We consider our results as promising for further development of such nanomaterial if optical properties could be optimized. This optimization would implicate not

only to master the surface chemistry of the NPs but also the development of optical imaging setup such as dark field optical coherence tomography allowing 3D images reconstruction.

## Bibliography

- [1] I. Balti, A. Mezni, A. Dakhlaoui-Omrani, P. Léone, B. Viana, O. Brinza, L. S. Smiri and N. Jouini, «Comparative Study of Ni- and Co-Substituted ZnO Nanoparticles: Synthesis, Optical, and Magnetic Properties,» *J. Phys. Chem. C*, vol. 115, n. 32, pp. 15758-15766, 2011.
- [2] I. Balti, L. S. Smiri, P. Rabu, E. Gautron, B. Viana and N. Jouini, «Synthesis and characterization of rod-like ZnO decorated with  $\gamma$ -Fe<sub>2</sub>O<sub>3</sub>,» *Journal of Alloys and Compounds*, vol. 586, n. 1, pp. S476-S482, 2014.
- [3] I. Balti, P. Chevallier, C. Ménager, A. Michel, N. Jouini, M. A. Fortin and F. Chaubet, «Nanocrystals of Zn(Fe)O-based diluted magnetic semi-conductor as potential luminescent and magnetic bimodal bioimaging probes,» *RSC Advances*, vol. 4, n. 102, pp. 58145-58150, 2014.
- [4] I. Balti, A. Barrere, V. Gueguen, L. Poussard, G. Pavon-Djavid, A. Meddahi-Pelle, P. Rabu, L. S. Smiri, N. Jouini and F. Chaubet, «Preparation of cytocompatible luminescent and magnetic nanohybrids based on ZnO, Zn<sub>0.95</sub>Ni<sub>0.05</sub>O and core@shell ZnO@Fe<sub>2</sub>O<sub>3</sub> polymer grafted nanoparticles for biomedical imaging,» *J Nanopart Res*, vol. 14, n. 1266, 2012.
- [5] J. F. Viles-Gonzalez, V. Fuster and J. J. Badimon, «Atherothrombosis: A widespread disease with unpredictable and life-threatening consequences,» *Eur Heart J*, vol. 25, n. 14, pp. 1197-1207, 2004.
- [6] American Heart Association, «<http://www.heart.org>,» [Online]. Available: [http://www.heart.org/HEARTORG/Conditions/Cholesterol/AboutCholesterol/Atherosclerosis\\_UCM\\_305564\\_Article.jsp#.We4AlB82vIU](http://www.heart.org/HEARTORG/Conditions/Cholesterol/AboutCholesterol/Atherosclerosis_UCM_305564_Article.jsp#.We4AlB82vIU).
- [7] American Heart Association, «<http://www.heart.org>,» 2016. [Online]. Available: [http://www.heart.org/HEARTORG/Conditions/Cholesterol/WhyCholesterolMatters/Atherosclerosis\\_UCM\\_305564\\_Article.jsp#.WMgCnB\\_QfIU](http://www.heart.org/HEARTORG/Conditions/Cholesterol/WhyCholesterolMatters/Atherosclerosis_UCM_305564_Article.jsp#.WMgCnB_QfIU).
- [8] R. K. Noyd, J. A. Krueger and K. M. Hill, «The biology of chronic disease,» in *Biology: Organisms and Adaptations, Media Update, Enhanced Edition*, Cengage Learning, 2016, pp. 650-652.
- [9] A. J. Lusis, «Atherosclerosis,» *Nature*, vol. 407, n. 6801, pp. 233-241, 2000.
- [10] «<http://www.strokeassociation.org>,» [Online].
- [11] «<http://healthlifemedia.com>,» [Online]. Available: <http://healthlifemedia.com/healthy/what-is-atherothrombosis/>.

- [12] «<http://www.nagygeneracio.hu>,» [Online]. Available: [http://www.nagygeneracio.hu/Erelmeszesedes\\_ellen\\_helyes\\_etrend](http://www.nagygeneracio.hu/Erelmeszesedes_ellen_helyes_etrend).
- [13] H. C. Stary, A. B. Chandler, R. E. Dinsmore, V. Fuster, S. Glagov, W. Insull, M. E. Rosenfeld, C. J. Schwartz, W. D. Wagner and R. W. Wissler, «A Definition of Advanced Types of Atherosclerotic Lesions and a Histological Classification of Atherosclerosis: A Report From the Committee on Vascular Lesions of the Council on Arteriosclerosis, American Heart Association,» *Circulation*, vol. 92, n. 5, pp. 1355-1374, 1995.
- [14] «<http://www.strokeassociation.org>,» [Online]. Available: [http://www.strokeassociation.org/STROKEORG/LifeAfterStroke/HealthyLivingAfterStroke/UnderstandingRiskyConditions/Atherosclerosis-and-Stroke\\_UCM\\_310426\\_Article.jsp#.Wc2KOh82vIU](http://www.strokeassociation.org/STROKEORG/LifeAfterStroke/HealthyLivingAfterStroke/UnderstandingRiskyConditions/Atherosclerosis-and-Stroke_UCM_310426_Article.jsp#.Wc2KOh82vIU).
- [15] M. A. Haidekker, «Medical Imaging Technology,» Springer-Verlag New York, 2013, pp. 1-12.
- [16] L. K. Jennings, «Role of platelets in atherothrombosis,» *Am. J. Cardiol*, vol. 103, n. 3, pp. 4A-10A, 2009.
- [17] R. Ross, «Atherosclerosis is an inflammatory disease,» *Am Heart J.*, vol. 138, n. 5, pp. S419-S420, 1999.
- [18] R. P. McEver, «Adhesive interactions of leukocytes, platelets, and the vessel wall during hemostasis and inflammation,» *Thromb Haemost*, vol. 86, n. 3, pp. 746-756, 2001.
- [19] M. Gawaz, H. Langer and A. E. May, «Platelets in inflammation and atherogenesis,» *J. Clin. Invest.*, vol. 2, pp. 3378-3384, 2005.
- [20] D. D. Wagner, «New links between inflammation and thrombosis. Arterioscler,» *Thromb. Vasc. Biol*, vol. 7, pp. 1321-1324, 2005.
- [21] R. P. McEver, «Selectin-carbohydrate interactions during inflammation and metastasis,» *Glycoconj. J.*, vol. 5, pp. 585-591, 1997.
- [22] C. Blondin, I. Bataille and D. Letourneur, «Polysaccharides for vascular cell targeting,» *Crit. Rev. Ther. Drug Carrier Syst.*, vol. 4, pp. 327-375, 2000.
- [23] D. Vestweber and J. E. Blanks, «Mechanisms that regulate the function of the selectins and their ligands,» *Physiol. Rev.*, vol. 1, pp. 181-213, 1999.
- [24] Y. Hiramatsu, H. Tsujishita and H. Kondo, «Studies on selectin blocker. 3. Investigation of the carbohydrate ligand sialyl Lewis X recognition site of P-selectin,» *J. Med. Chem.*, vol. 39, n. 23, pp. 4547-4553, 1996.

- [25] J. Y. Ramphal, Z. L. Zheng, C. Perez, L. E. Walker, S. A. DeFrees and F. C. Gaeta, «Structure-Activity Relationships of Sialyl Lewis x-Containing Oligosaccharides. 1. Effect of Modifications of the Fucose Moiety,» *J Med Chem*, vol. 37, n. 21, pp. 3459-63, 1994.
- [26] B. K. Brandley, M. Kiso, S. Abbas, P. Nikrad, O. Srivasatava, C. Foxall, Y. Oda and A. Hasegawa, «Structure-function studies on selectin carbohydrate ligands. Modifications to fucose, sialic acid and sulphate as a sialic acid replacement,» *Glycobiology*, vol. 6, pp. 633-641, 1993.
- [27] L. Bachelet, I. Bertholon, D. Lavigne, R. Vassy, M. Jandrot-Perrus, F. Chaubet and D. Letourneur, «Affinity of low molecular weight fucoidan for P-selectin triggers its binding to activated human platelets,» *Biochim. Biophys. Acta*, vol. 1790, pp. 141-146, 2009.
- [28] T. V. Pochechueva, O. E. Galanina, N. A. Ushakova, M. E. Preobrazhenskaya, M. A. Sablina, N. E. Nifantiev, Y. V. Tsvetkov, Y. V. Vozney, A. Imberty and N. V. Bovin, «Uncharged P-selectin blockers,» *Glycoconj. J*, vol. 20, pp. 91-97, 2004.
- [29] A. Koenig, R. Jain, R. Vig, K. E. Norgard-Sumnicht, K. L. Matta and A. Varki, «Selectin inhibition: synthesis and evaluation of novel sialylated, sulfated and fucosylated oligosaccharides, including the major capping group of GlyCAM-1,» *Glycobiology*, vol. 7, n. 1, pp. 79-93, 1997.
- [30] A Varki, «Selectin ligands,» *Proc. Natl. Acad. Sci. U S A*, vol. 91, pp. 7390-7397, 1994.
- [31] A. C. Lake, R. Vassy, M. D. Benedetto, D. Lavigne, C. Le Visage, G. Y. Perret and D. Letourneur, «Low molecular weight fucoidan increases VEGF165-induced endothelial cell migration by enhancing VEGF165 binding to VEGFR-2 and NRP1,» *J. Biol. Chem.*, vol. 281, pp. 37844-37852, 2006.
- [32] C. E. Luyt, A. Meddahi-Pelle, B. Ho-Tin-Noe, S. Collic-Jouault, J. Guezennec, L. Louedec, H. Prats, M. P. Jacob, M. Osborne-Pellegrin, D. Letourneur and J. B. Michel, «Low-molecular-weight fucoidan promotes therapeutic revascularization in a rat model of critical hindlimb ischemia,» *J Pharmacol Exp Ther. Apr;305(1):.*, vol. 305, n. 1, pp. 24-30, 2003.
- [33] J. F. Deux, A. Meddahi-Pelle, A. F. Le Blanche, L. J. Feldman, S. Collic-Jouault, F. Bree, F. Boudghene, J. B. Michel and D. Letourneur, «Low Molecular Weight Fucoidan Prevents Neointimal Hyperplasia in Rabbit Iliac Artery In-Stent Restenosis Model,» *Arterioscler. Thromb. Vasc. Biol.*, vol. 22, pp. 1604-1609, 2002.
- [34] M. Suzuki, L. Bachelet-Violette, F. Rouzet, A. Beilvert, G. Autret, M. Maire, C. Menager, L. Louedec, C. Choqueux, P. Saboural, O. Haddad, C. Chauvierre, F. Chaubet, J. B. Michel, J. M. Serfaty and D. Letourneur, «Ultrasml

superparamagnetic iron oxide nanoparticles coated with fucoidan for molecular MRI of intraluminal thrombus,» *Nanomedicine*, vol. 10, n. 1, pp. 73-87, 2015.

- [35] L. Bachelet-Violette, A. K. A. Silva, M. Maire, A. Michel, O. Brinza, P. Ou, V. Ollivier, A. Nicoletti, C. Wilhelm, D. Letourneur, C. Ménagerd and F. Chaubet, «Strong and specific interaction of ultra small superparamagnetic iron oxide nanoparticles and human activated platelets mediated by fucoidan coating,» *RSC Advances*, vol. 4, n. 10, pp. 4864-4871, 2014.
- [36] P. Saboural, F. Chaubet, F. Rouzet, F. Al-Shoukr, R. B. Azzouna, N. Bouchemal, L. Picton, L. Louedec, M. Maire, L. Rolland, G. Potier, D. L. Guludec, D. Letourneur and C. Chauvierre, «Purification of a Low Molecular Weight Fucoidan for SPECT Molecular Imaging of Myocardial Infarction,» *Mar Drugs*, vol. 12, n. 9, pp. 4851-4867, 2014.
- [37] B. Li, M. Juenet, R. Aid-Launais, M. Maire, V. Ollivier, D. Letourneur and C. Chauvierre, «Development of Polymer Microcapsules Functionalized with Fucoidan to Target P-Selectin Overexpressed in Cardiovascular Diseases,» *Adv Healthc Mater.*, vol. 6, n. 4, 2017.
- [38] Ch. W. Sensen and B. Hallgrimsson, «Medical imaging modalities - An Introduction,» in *Advanced Imaging in Biology and Medicine: Technology, Software Environments, Applications*, Springer Science & Business Media, 2008, pp. 225-254.
- [39] W. A. Kalender, «Principles of Computed Tomography,» in *Computed Tomography: Fundamentals, System Technology, Image Quality, Applications*, Publicis, 2011, p. 21.
- [40] E. Iadanza and J. Dyro, «History of Engineering and Technology in Health Care,» in *Clinical Engineering Handbook*, Academic Press, 2004, p. 8.
- [41] J. G. Fujimoto and D. Farkas, «Biomedical Optical Imaging,» Oxford University, 2009, p. 164.
- [42] C. M. Moran, S. D. Pye, W. Ellis, A. Janeczko, K. D. Morris, A. S. McNeilly and H. M. Fraser, «A Comparison of the Imaging Performance of High Resolution Ultrasound Scanners for Preclinical Imaging,» *Ultrasound in Medicine & Biology*, vol. 37, n. 3, pp. 493-501, 2011.
- [43] «wikipedia,» [Online]. Available: [https://en.wikipedia.org/wiki/Magnetic\\_resonance\\_imaging](https://en.wikipedia.org/wiki/Magnetic_resonance_imaging).
- [44] «nationalmaglab,» [Online]. Available: <https://nationalmaglab.org/about/around-the-lab/meet-the-magnets/meet-the-900-mhz-nmr-magnet>.
- [45] S. W. Hell and J. Wichmann, «Breaking the diffraction resolution limit by

- stimulated-emission: stimulated emission- depletion fluorescence microscopy,» *Opt. Lett.*, vol. 19, pp. 780-782, 1994.
- [46] T. A. Klar and S. W. Hell, «Subdiffraction resolution in far-field fluorescence microscopy,» *Opt. Lett.*, vol. 24, pp. 954-956, 1999.
- [47] M. J. Rust, M. Bates and X. Zhuang, «Sub-diffraction-limit imaging by stochastic optical reconstruction microscopy (STORM),» *Nat. Methods.*, vol. 3, pp. 793-795, 2006.
- [48] S. T. Hess, T. P. K. Girirajan and M. D. Mason, «Ultra-high resolution imaging by fluorescence photoactivation localization microscopy,» *Biophys. J.*, vol. 91, pp. 4258-4272, 2006.
- [49] J. Dowden and W. Schulz, «The Theory of Laser Materials Processing: Heat and Mass Transfer in Modern Technology,» Springer, 2017, p. 342.
- [50] M. C. Schanne-Klein, «Second harmonic imaging of collagen organization in connective tissues,» *European Microscopy Congress 2016: Proceedings*, pp. 197-198, 2016.
- [51] T. A. Theodossiou, C. Thrasivoulou, C. Ekwobi and D. L. Becker, «Second Harmonic Generation Confocal Microscopy of Collagen Type I from Rat Tendon Cryosections,» *Biophys J.*, vol. 91, n. 12, pp. 4665-4677, 2006.
- [52] C. Teulon, A. Tidu, F. Portier and M. C. Schanne-Klein, «Probing the 3D structure of cornea-like collagen liquid crystals with polarization-resolved SHG microscopy,» *Optics Express*, vol. 24, n. 14, pp. 16084-16098, 2016.
- [53] P. J. Campagnola, A. C. Millard, M. Terasaki, P. E. Hoppe, C. J. Malone and W. A. Mohler, «Three-Dimensional High-Resolution Second-Harmonic Generation Imaging of Endogenous Structural Proteins in Biological Tissues,» *Biophysical Journal*, vol. 82, n. 1, pp. 493-508, 2002.
- [54] A. F. Fercher, K. Mengedoht and W. Werner, «Eye-length measurement by interferometry with partially coherent light,» *Optics Letters*, vol. 13, n. 3, pp. 186-188, 1988.
- [55] W. Drexler, «Cellular and functional optical coherence tomography of the human retina: the cogan lecture,» *Investigative Ophthalmology and Visual Science*, vol. 48, n. 12, pp. 5340-5351, 2007.
- [56] M. Wojtkowski, R. Leitgeb, A. Kowalczyk, T. Bajraszewski and A. F. Fercher, «In vivo human retinal imaging by Fourier domain optical coherence tomography,» *Journal of Biomedical Optics*, vol. 7, n. 3, pp. 457-463, 2002.
- [57] D. A. Dartt, P. Bex, P. D'Amore, R. Dana, L. Mcloon and J. Niederkorn, «Ocular

Periphery and Disorders,» Academic Press, 2011, p. 238.

- [58] D. Malcius, M. Jonkus, G. Kuprionis, A. Maleckas, E. Monastyreckiene, R. Uktveris, S. Rinkevicius and V. Barauskas, «The accuracy of different imaging techniques in diagnosis of acute hematogenous osteomyelitis,» *Medicina (Kaunas)*, vol. 45, n. 8, pp. 624-31, 2009.
- [59] W. C. Lavelly, S. Goetze, K. P. Friedman, J. P. Leal, Z. Zhang, E. Garret-Mayer, A. P. Dackiw, R. P. Tufano, M. A. Zeiger and H. A. Ziessman, «Comparison of SPECT/CT, SPECT, and Planar Imaging with Single- and Dual-Phase 99mTc-Sestamibi Parathyroid Scintigraphy,» *J Nucl Med*, vol. 48, p. 1084–1089, 2007.
- [60] L. Cheng, J. Li, M. Liu, S. Wang, H. C. Jiang and D. Q. Yang, «Comparison of dynamic optical breast imaging (DOBI) and mammography in sensitivity, specificity and safety of breast cancer diagnosis: a prospective analysis of 62 patients in two centers,» *Beijing Da Xue Xue Bao Yi Xue Ban*, vol. 43, n. 3, pp. 467-71, 2011.
- [61] V. Jacques, S. Dumas, W.-C. Sun, J. S. Troughton, M. T. Greenfield and P. Caravana, «High relaxivity MRI contrast agents part 2: Optimization of inner- and second-sphere relaxivity,» *Invest Radiol*, vol. 45, n. 10, pp. 613-624, 2010.
- [62] S. Dumas, V. Jacques, W. -C. Sun, J. S. Troughton, J. T. Welch, J. M. Chasse, H. Schmitt-Willich and P. Caravana, «High relaxivity MRI contrast agents part 1: Impact of single donor atom substitution on relaxivity of serum albumin-bound gadolinium complexes,» *Invest Radiol*, vol. 45, n. 10, pp. 600-612, 2010.
- [63] M. Rohrer, H. Bauer and J. Mintorovitch, «Comparison of Magnetic Properties of MRI Contrast Media Solutions at Different Magnetic Field Strengths,» *Investigative Radiology*, vol. 40, n. 11, pp. 715-724, 2005.
- [64] I. Solomon, «Relaxation Processes in a System of Two Spins,» *Physical Review*, vol. 99, n. 2, pp. 559-565, 1955.
- [65] N. Bloembergen, «Proton Relaxation Times in Paramagnetic Solutions,» *The Journal of Chemical Physics*, vol. 27, n. 2, p. 572, 1957.
- [66] N. Bloembergen and L. O. Morgan, «Proton Relaxation Times in Paramagnetic Solutions. Effects of Electron Spin Relaxation,» *The Journal of Chemical Physics*, vol. 34, n. 3, p. 842, 1961.
- [67] N. T. Nghia, «Development of microscopy system for time-resolved fluorescence detection of gadolinium/terbium hybrid macromolecular complexes for bimodal imaging of atherothrombosis,» Universite Paris-Nord - Paris XIII, 2014.
- [68] A. Bjornerud and L. Johansson, «The utility of superparamagnetic contrast agents

- in MRI: theoretical consideration and applications in the cardiovascular system,» *NMR in Biomedicine*, vol. 17, n. 7, pp. 465-477, 2004.
- [69] G. Strijkers, W. M. Mulder, G. F. V. Tilborg and K. Nicolay, «MRI Contrast Agents: Current Status and Future Perspectives,» *Anti-Cancer Agents in Medicinal Chemistry*, vol. 7, n. 3, pp. 291-305, 2007.
- [70] C. V. Bowen, X. Zhang, G. Saab, P. J. Gareau and B. K. Rutt, «Application of the static dephasing regime theory to superparamagnetic iron-oxide loaded cells,» *Magn Reson Med*, vol. 48, n. 1, pp. 52-61, 2002.
- [71] Y. X. Wang, S. M. Hussain and G. P. Krestin, «Superparamagnetic iron oxide contrast agents: physicochemical characteristics and applications in MR imaging,» *Eur Radiol*, vol. 11, n. 11, pp. 2319-2331, 2001.
- [72] R. Weissleder, G. Elizondo, J. Wittenberg, C. A. Rabito, H. H. Bengel and L. Josephson, «Ultrasmall superparamagnetic iron oxide: characterization of a new class of contrast agents for MR imaging,» *Radiology*, vol. 175, n. 2, pp. 489-493, 1990.
- [73] R. Weissleder, A. Bogdanov, E. A. Neuwelt and M. Papisov, «Long-circulating iron oxides for MR imaging,» *Advanced Drug Delivery Reviews*, vol. 16, n. 2-3, pp. 321-334, 1995.
- [74] P. Wunderbaldinger, L. Josephson and R. Weissleder, «Crosslinked iron oxides (CLIO): a new platform for the development of targeted MR contrast agents,» *Acad Radiol*, vol. 9, n. 2, pp. S304-306, 2002.
- [75] H. Nakamura, N. Ito, F. Kotake, Y. Mizokami and T. Matsuoka, «Tumor-detecting capacity and clinical usefulness of SPIO-MRI in patients with hepatocellular carcinoma,» *J Gastroenterol*, vol. 35, n. 11, pp. 849-855, 2000.
- [76] S. Richard , V. Eder , G. Caputo , C. Journé , P. Ou , J. Bolley , L. Louedec , E. Guenin , L. Motte , N. Pinna and Y. Lalatonne, «USPIO size control through microwave nonaqueous sol-gel method for neoangiogenesis T2 MRI contrast agent,» *Nanomedicine*, vol. 11, n. 21, 2016.
- [77] A. Moezzi, A. M. McDonagh and M. B. Cortie, «Zinc oxide particles: Synthesis, properties and applications,» *Chemical Engineering Journal*, Vol. 218, pp. 1-22, 2012.
- [78] K. M. Lee, C. W. Lai, K. S. Ngai and J. C. Juan, «Recent Developments of Zinc Oxide Based Photocatalyst in Water Treatment Technology: A Review,» *Water Research*, vol. 88, pp. 428-488, 2016.
- [79] V. Sivasubramanian, «Environmental Sustainability Using Green Technologies,» CRC Press, 2016, p. 85.

- [80] K. Vanheusden, C. H. Seager, W. L. Warren, D. R. Tallant and J. A. Voigt, «Correlation between photoluminescence and oxygen vacancies in ZnO phosphors,» *Appl. Phys. Lett.*, vol. 68, pp. 403-405, 1996.
- [81] S. Monticone, R. Tufeu and A. V. Kanaev, «Complex Nature of the UV and Visible Fluorescence of Colloidal ZnO Nanoparticles,» *J. Phys. Chem. B*, vol. 102, n. 16, pp. 2854-2862, 1998.
- [82] A. V. Dijken, E. A. Meulenkamp, D. Vanmaekelbergh and A. Meijerink, «The Kinetics of the Radiative and Nonradiative Processes in Nanocrystalline ZnO Particles upon Photoexcitation,» *J. Phys. Chem. B*, vol. 104, pp. 1715-1723, 2000.
- [83] Ü. Özgür, Ya. I. Alivov, C. Liu, A. Teke, M. A. Reshchikov, S. Doğan, V. Avrutin, S. J. Cho and H. Morkoç, «A comprehensive review of ZnO materials and devices,» *Journal of Applied Physics* 98, vol. 98, n. 4, 2005.
- [84] A. van Dijken, E. A. Meulenkamp, D. Vanmaekelbergh and A. Meijerink, «Identification of the transition responsible for the visible emission in ZnO using quantum size effects,» *J. Lumin.*, vol. 90, pp. 123-128, 2000.
- [85] L. Zhang, L. Yin, C. Wang, N. lun, Y. Qi and D. Xiang, «Origin of Visible Photoluminescence of ZnO Quantum Dots: Defect-Dependent and Size-Dependent,» *J. Phys. Chem. C*, vol. 114, n. 21, pp. 9651-9658, 2010.
- [86] M. Jr. Bruchez, M. Moronne, P. Gin, S. Weiss and A. P. Alivisatos, «Semiconductor nanocrystals as fluorescent biological labels,» *Science*, vol. 28, n. 5385, pp. 2013-2016, 1998.
- [87] W. C. Chan and S. Nie, «Quantum Dot Bioconjugates for Ultrasensitive Nonisotopic Detection,» *Science*, vol. 281, n. 5385, pp. 2016-2018, 1998.
- [88] T. Jamieson, R. Bakhshi, D. Petrova, R. Pocock, M. Imani and A. M. Seifalian, «Biological applications of quantum dots,» *Biomaterials*, vol. 28, pp. 4717-4732, 2007.
- [89] F. M. Winnik and D. Maysinger, «Quantum dot cytotoxicity and ways to reduce it,» *Acc Chem Res.*, vol. 46, n. 3, pp. 672-680, 2013.
- [90] C. E. Bradburne, J. B. Delehanty, G. K. Boeneman, B. C. Mei, H. Mattoussi, K. Susumu, J. B. Blanco-Canosa, P. E. Dawson and I. L. Medintz, «Cytotoxicity of quantum dots used for in vitro cellular labeling: role of QD surface ligand, delivery modality, cell type, and direct comparison to organic fluorophores,» *Bioconjug Chem.*, vol. 24, n. 9, pp. 1570-1583, 2013.
- [91] G. Auer, W.D. Griebler and B. Jahn, «Industrial Inorganic Pigments,» in *White pigments*, Wiley-VCH Verlag GmbH & Co. KGaA, Weinheim, 2005, p. 82.

- [92] W. Wu, J. Shen, P. Banerjee and S. Zhou, «A Multifunctional Nanoplatfrom Based on Responsive Fluorescent Plasmonic ZnO-Au@PEG Hybrid Nanogels,» *Adv. Funct. Mater.*, vol. 21, n. 5, pp. 2830-2839, 2011.
- [93] X. Tang, E. S. G. Choo, L. Li, J. Ding and J. Xue, «One-Pot Synthesis of Water-Stable ZnO Nanoparticles via a Polyol Hydrolysis Route and Their Cell Labeling Applications,» *Langmuir*, vol. 25, n. 9, pp. 5271-5275, 2009.
- [94] H. M. Xiong, Y. Xu, Q. G. Ren and Y. Y. Xia, «Stable Aqueous ZnO@Polymer Core-Shell Nanoparticles with Tunable Photoluminescence and Their Application in Cell Imaging,» *J. Am. Chem. Soc.*, vol. 130, n. 24, pp. 7522-7523, 2008.
- [95] H. M. Xiong, «ZnO nanoparticles applied to bioimaging and drug delivery,» *Adv. Mater.*, vol. 25, pp. 5329-5335, 2013.
- [96] Z. Song, T. A. Kelf, W. H. Sanchez, M. S. Roberts, J. Rička, M. Frenz and A. V. Zvyagin, «Characterization of optical properties of ZnO nanoparticles for quantitative imaging of transdermal transport,» *Biomed Opt Express*, vol. 2, n. 12, pp. 3321-3333, 2011.
- [97] J. Drbohlavova, V. Adam, R. Kizek and J. Hubalek, «Quantum Dots - Characterization, Preparation and Usage in Biological Systems,» *Int. J. Mol. Sci.*, vol. 10, n. 2, pp. 656-673, 2009.
- [98] T. R. Dunkern, G. Fritz and B. Kaina, «Ultraviolet light-induced DNA damage triggers apoptosis in nucleotide excision repair-deficient cells via Bcl-2 decline and caspase-3/-8 activation,» *Oncogene*, vol. 20, pp. 6026-6038, 2001.
- [99] N. Goosen and G. F. Moolenaar, «Repair of UV damage in bacteria,» *DNA Repair (Amst)*, vol. 7, n. 3, pp. 353-379, 2008.
- [100] K. Hikishima, Y. Komaki, F. Seki, Y. Ohnishi, H. J. Okano and H. Okano, «In vivo microscopic voxel-based morphometry with a brain template to characterize strain-specific structures in the mouse brain,» *Scientific Reports*, vol. 7, n. 85, 2017.
- [101] D. Stucht, K. A. Danishad, P. Schulze, F. Godenschweger, M. Zaitsev and O. Speck, «Highest Resolution In Vivo Human Brain MRI Using Prospective Motion Correction,» *PLoS One*, vol. 10, n. 7, 2015.
- [102] H. Bridge and S. Clare, «High-resolution MRI: in vivo histology?,» *Philosophical Transactions of the Royal Society B: Biological Sciences*, vol. 361, n. 1465, pp. 137-146, 2006.
- [103] P. Eghbali, H. Fattahi, S. Laurent, R. N. Muller and Y. M. Oskoei, «Fluorophore-tagged superparamagnetic iron oxide nanoparticles as bimodal contrast agents for MR/optical imaging,» *Journal of the Iranian Chemical Society*, vol. 13, n. 1, pp.

87-93, 2016.

- [104] A. Beilvert, D. P. Cormode, F. Chaubet, K. C. Briley-Saebo, V. Mani, W. J. M. Mulder, E. Vucic, J. F. Toussaint, D. Letourneur and Z. A. Fayad, «Tyrosine polyethylene glycol (PEG)-micelle magnetic resonance contrast agent for the detection of lipid rich areas in atherosclerotic plaque,» *Magnetic Resonance in Medicine*, vol. 62, n. 5, pp. 1195-1201, 2009.
- [105] C. Bremer, V. Ntziachristos and R. Weissleder, «Optical-based molecular imaging: contrast agents and potential medical applications,» *Eur Radio*, vol. 13, n. 2, pp. 231-243, 2003.
- [106] I. Hemmilä, S. Dakubu, V. M. Mukkala, H. Siitari and T. Lövgren, «Europium as a label in time-resolved immunofluorometric assays,» *Anal. Biochem.*, vol. 137, n. 2, pp. 335-343, 1984.
- [107] W. L. Scaff, D. L. Dyer and K. Mor, «Fluorescent europium chelate stain,» *Journal of bacteriology*, vol. 98, n. 1, pp. 246-248, 1969.
- [108] J. C. G. Bünzli, «Lanthanide Luminescent Bioprobes,» *Chemistry Letters*, vol. 38, n. 2, pp. 104-109, 2009.
- [109] J. Yuan and G. Wang, «Lanthanide complex-based fluorescence label,» *J Fluoresc.*, vol. 15, n. 4, pp. 559-568, 2005.
- [110] M. Ceulemans, K. Nuyts, W. M. De Borggraeve and T. N. Parac-Vogt, «Gadolinium(III)-DOTA Complex Functionalized with BODIPY as a Potential Bimodal Contrast Agent for MRI and Optical Imaging,» *Inorganics*, vol. 3, n. 4, pp. 516-533, 2015.
- [111] N. T. Nghia, E. Tinet, D. Etori, A. Beilvert, G. Pavon-Djavid, M. Maire, P. Ou, J. M. Tualle, F. Chaubet, «Gadolinium/terbium hybrid macromolecular complexes for bimodal imaging of atherothrombosis,» *J Biomed Opt.*, vol. 22, n. 7, p. 76004, 2017.
- [112] J. Cao, W. Fu, H. Yang, Q. Yu, Y. Zhang, S. Wang, H. Zhao, Y. Sui, X. Zhou, W. Zhao, Y. Leng, H. Zhao, H. Chen and X. Qi, «Fabrication, characterization and application in electromagnetic wave absorption of flower-like ZnO/Fe<sub>3</sub>O<sub>4</sub> nanocomposites,» *Materials Science and Engineering: B*, vol. 175, n. 1, pp. 56-59, 2010.
- [113] H. L. Liu, J. H. Wu, J. H. Min, X. Y. Zhang and Y. K. Kim, «Tunable synthesis and multifunctionalities of Fe<sub>3</sub>O<sub>4</sub>-ZnO hybrid core-shell nanocrystals,» *Materials Research Bulletin*, vol. 48, n. 2, pp. 551-558, 2013.
- [114] J. Wan, H. Li and K. Chen, «Synthesis and characterization of Fe<sub>3</sub>O<sub>4</sub>@ZnO core-shell structured nanoparticles,» *Materials Chemistry and Physics*, vol. 114, n. 1, pp.

30-32, 2009.

- [115] S. V. Vinogradov, T. K. Bronich and A. V. Kabanov, «Nanosized cationic hydrogels for drug delivery: preparation, properties and interactions with cells,» *Adv Drug Deliv Rev.*, vol. 54, n. 1, pp. 135-147, 2002.
- [116] H. S. Choi, W. Liu, P. Misra, E. Tanaka, J. P. Zimmer, B. I. Ipe, M. G. Bawendi and J. V. Frangioni, «Renal clearance of quantum dots,» *Nature Biotechnology*, vol. 25, pp. 1165-1170, 2007.
- [117] E. Casals, T. Pfaller, A. Duschl, G. J. Oostingh and V. Puentes, «Time Evolution of the Nanoparticle Protein Corona,» *ACS Nano*, vol. 4, pp. 3623-3632, 2010.
- [118] T. Cedervall, I. Lynch, M. Foy, T. Berggard, S. Donnelly, G. Cagney, S. Linse and K. Dawson, «Detailed identification of plasma proteins adsorbed on copolymer nanoparticles,» *Angew Chem Int Ed.*, vol. 46, pp. 5754-5756, 2007.
- [119] J. V. Jokerst, T. Lobovkina, R. N. Zare and S. S. Gambhi, «Nanoparticle PEGylation for imaging and therapy,» *Nanomedicine (Lond.)*, vol. 6, n. 4, pp. 715-728, 2011.
- [120] L. Lutterotti, S. Matthies and H. R. Wenk, «Maud: a friendly java program for material analysis using diffraction,» *Newsletter of the CPD*, vol. 21, pp. 14-15, 1999.
- [121] D. Fikai and A. M. Grumezescu, «Synthetic methods for preparation of metal nanoparticles,» in *Nanostructures for Novel Therapy: Synthesis, Characterization and Applications*, Technology & Engineering, 2017, p. 15.
- [122] M. L. D. L. Chapelle and A. Pucci, «Nanoparticle synthesis,» in *Nanoantenna: Plasmon-Enhanced Spectroscopies for Biotechnological Applications*, Science, 2013, p. 107.
- [123] «Wikipedia,» [Online]. Available: [https://en.wikipedia.org/wiki/Wurtzite\\_crystal\\_structure](https://en.wikipedia.org/wiki/Wurtzite_crystal_structure).
- [124] M. L. Dinesha, G. D. Prasanna, C. S. Naveen and H. S. Jayanna, «Structural and dielectric properties of Fe doped ZnO nanoparticles,» *Indian J Phys*, vol. 87, n. 2, pp. 147-153, 2013.
- [125] M. A. Ciciliati, M. F. Silva, D. M. Fernandes, M. A. C. D. Melo, A. Adelin, W. Hechenleitner and E. A. G. Pineda, «Fe-doped ZnO nanoparticles: Synthesis by a modified sol-gel method and characterization,» *Materials Letters*, vol. 159, pp. 84-86, 2015.
- [126] V. G. Il'ves, S. Yu. Sokovnin and A. M. Murzakaev, «Influence of Fe-Doping on the Structural and Magnetic Properties of ZnO Nanopowders, Produced by the

- Method of Pulsed Electron Beam Evaporation,» *Journal of Nanotechnology*, vol. 2016, 2016.
- [127] P. A. Arciniegas-Grijalba, M. C. Patiño-Portela, L. P. Mosquera-Sánchez, J. A. Guerrero-Vargas and J. E. Rodríguez-Páez, «ZnO nanoparticles (ZnO-NPs) and their antifungal activity against coffee fungus *Erythricium salmonicolor*,» *Applied Nanoscience*, vol. 7, n. 5, pp. 225-241, 2017.
- [128] A. Mezni, F. Kouki, S. Romdhane, B. Warot-Fonrose, S. Joulie, A. Mlayah and L. S. Smiri, «Facile synthesis of ZnO nanocrystals in polyol,» *Materials Letters*, vol. 86, pp. 153-156, 2012.
- [129] P. Guo, L. Cui, Y. Wang, M. Lv, B. Wang and X. S. Zhao, «Facile synthesis of ZnFe<sub>2</sub>O<sub>4</sub> nanoparticles with tunable magnetic and sensing properties,» *Langmuir*, vol. 29, n. 28, pp. 8997-9003, 2013.
- [130] C. Yao, Q. Zeng, G. F. Goya, T. Torres, J. Liu, H. Wu, M. Ge, Y. Zeng, Y. Wang and J. Z. Jiang, «ZnFe<sub>2</sub>O<sub>4</sub> Nanocrystals: Synthesis and Magnetic Properties,» *J. Phys. Chem. C*, vol. 111, pp. 12274-12278, 2007.
- [131] E. G. Bylander, «Surface effects on the low-energy cathodoluminescence of zinc oxide,» *Journal of Applied Physics*, vol. 49, n. 3, pp. 1188-1196, 1978.
- [132] U. Ozgur, Y. I. Alivov, C. Liu, A. Teke, M. A. Reshchikov, S. Dogan, V. Avrutin, S. J. Cho and H. Morkoc, «A comprehensive review of ZnO materials and devices,» *J. Appl. Phys.*, vol. 98, pp. 041301-041403, 2005.
- [133] K. Vanheusden, W. L. Warren, C. H. Seager, D. R. Tallant, J. A. Voigt and B. E. Gnade, «Mechanisms behind green photoluminescence in ZnO phosphor powders,» *J. Appl. Phys.*, vol. 79, pp. 7983-7990, 1996.
- [134] N. Lee, D. Yoo, D. Ling, M. H. Cho, T. Hyeon and J. Cheon, «Iron Oxide Based Nanoparticles for Multimodal Imaging and Magnetoresponse Therapy,» *Chem. Rev.*, vol. 115, pp. 10637-10689, 2015.
- [135] M. Leclerc and R. Gauvin, «New trends in sustainable development and biomedical applications,» in *Functional Materials: For Energy, Sustainable Development and Biomedical Sciences*, Technology & Engineering, 2014, p. 340.
- [136] L. M. Parkes, R. Hodgson, T. L. Lu, D. L. Tung, I. Robinson, D. G. Fernig and N. T. Thanh, «Cobalt nanoparticles as a novel magnetic resonance contrast agent--relaxivities at 1.5 and 3 Tesla,» *Contrast Media Mol Imaging*, vol. 3, n. 4, pp. 150-156, 2008.
- [137] D. L. Thorek, A. K. Chen, J. Czupryna and A. Tsourkas, «Superparamagnetic iron oxide nanoparticle probes for molecular imaging,» *Ann Biomed Eng.*, vol. 34, n. 1, pp. 23-38, 2006.

- [138] N. Chan, M. Laprise-Pelletier, P. Chevallier, A. Bianchi, M. A. Fortin and J. K. Oh, «Multidentate Block-Copolymer-Stabilized Ultrasmall Superparamagnetic Iron Oxide Nanoparticles with Enhanced Colloidal Stability for Magnetic Resonance Imaging,» *Biomacromolecules*, vol. 15, pp. 2146-2156, 2014.
- [139] M. F. Casula, P. Floris, C. Innocenti, A. Lascialfari, M. Marinone, M. Corti, R. A. Sperling, W. J. Parak and C. Sangregorio, «Magnetic Resonance Imaging Contrast Agents Based on Iron Oxide Superparamagnetic Ferrofluids,» *Chem. Mater.*, vol. 22, n. 5, pp. 1739-1748, 2010.
- [140] B. H. Kim, N. Lee, H. Kim, K. An, Y. I. Park, Y. Choi, K. Shin, Y. Lee, S. G. Kwon, H. B. Na, J. G. Park, T. Y. Ahn, Y. W. Kim, W. K. Moon, S. H. Choi and T. Hyeon, «Large-Scale Synthesis of Uniform and Extremely Small-Sized Iron Oxide Nanoparticles for High-Resolution T1 Magnetic Resonance Imaging Contrast Agents,» *J. Am. Chem. Soc.*, vol. 133, n. 32, pp. 12624-12631, 2011.
- [141] P. Kucheryavy, J. He, V. T. John, P. Maharjan, L. Spinu, G. Z. Goloverda and V. L. Kolesnichenko, «Superparamagnetic Iron Oxide Nanoparticles with Variable Size and an Iron Oxidation State as Prospective Imaging Agents,» *Langmuir*, vol. 29, n. 2, p. 710–716, 2013.
- [142] U. I. Tromsdorf, O. T. Bruns, S. C. Salmen, U. Beisiegel and H. Weller, «A Highly Effective, Nontoxic T1 MR Contrast Agent Based on Ultrasmall PEGylated Iron Oxide Nanoparticles,» *Nano Lett.*, vol. 9, n. 12, pp. 4434-4440, 2009.
- [143] G. Wang, X. Zhang, A. Skallberg, Y. Liu, Z. Hu, X. Mei and K. Uvdal, «One-step synthesis of water-dispersible ultra-small Fe<sub>3</sub>O<sub>4</sub> nanoparticles as contrast agents for T1 and T2 magnetic resonance imaging,» *Nanoscale*, vol. 6, n. 5, pp. 2953-2963, 2014.
- [144] S. M. Hoque, M. S. Hossain, S. Choudhury, S. Akhter and F. Hyder, «Synthesis and characterization of ZnFe<sub>2</sub>O<sub>4</sub> nanoparticles and its biomedical applications,» *Mater Lett.*, vol. 12, p. 60–63, 2016.
- [145] J. Wan, X. Jiang, H. Li and K. Chen, «Facile synthesis of zinc ferrite nanoparticles as non-lanthanide T1 MRI contrast agents,» *Royal Society of Chemistry*, vol. 22, pp. 13500-13505, 2012.
- [146] A. Banerjee, B. Blasiak, E. Pasquier, B. Tomanek and S. Trudel, «Synthesis, characterization, and evaluation of PEGylated first-row transition metal ferrite nanoparticles as T2 contrast agents for high-field MRI,» *RSC Adv.*, vol. 7, pp. 38125-38134, 2017.
- [147] J. W. Uhr, M. L. Huebschman, E. P. Frenkel, N. L. Lane, R. Ashfaq, H. Liu, D. R. Rana, L. Cheng, A. T. Lin, G. A. Hughes, X. J. Zhang and H. R. Garner, «Molecular profiling of individual tumor cells by hyperspectral microscopic

- imaging,» *Translational Research*, vol. 159, pp. 366-375, 2011.
- [148] D. Zopf, J. Jatschka, A. Dathe, N. Jahr, W. Fritzsche and O. Stranik, «Hyperspectral imaging of plasmon resonances in metallic nanoparticles Biosensors and Bioelectronics,» *Biosens Bioelectron.*, vol. 81, pp. 287-293, 2016.
- [149] M. D. P. S. Peña, A. Gottipati, S. Tahiliani, N. M. Neu-Baker, M. D. Frame, A. J. Friedman and S. A. Brenner, «Hyperspectral imaging of nanoparticles in biological samples: Simultaneous visualization and elemental identification,» *Microscopy Research and Technique*, vol. 79, n. 5, p. 349–358, 2016.
- [150] «<http://www.malvern.com/>,» Malvern, 2017. [Online]. Available: <http://www.malvern.com/en/products/technology/nanoparticle-tracking-analysis/>.
- [151] R. E. Thompson, D. R. Larson and W. W. Webb, «Precise Nanometer Localization Analysis for Individual Fluorescent Probes,» *Biophysical Journal*, vol. 82, pp. 2775-2783, 2002.
- [152] S. Wieser and G. J. Schütz, «Tracking single molecules in the live cell plasma membrane-Do's and Don't's,» *Methods*, vol. 46, n. 2, pp. 131-140, 2008.
- [153] B. V. D. Broek, B. Ashcroft, T. H. Oosterkamp and J. V. Noort, «Parallel Nanometric 3D Tracking of Intracellular Gold Nanorods Using Multifocal Two-Photon Microscopy,» *Nano Letter*, vol. 13, n. 3, p. 980–986, 2013.
- [154] Y. Katayama, O. Burkacky, M. Meyer, C. Bräuchle, E. Gratton and D. C. Lamb, «Real-time nanomicroscopy via three-dimensional single-particle tracking,» *Chemphyschem*, vol. 10, n. 14, pp. 2458-2464, 2009.
- [155] R. Parthasarathy, «Rapid, accurate particle tracking by calculation of radial symmetry centers,» *Nature Methods*, vol. 9, p. 724–726, 2012.
- [156] S. L. Liu, J. Li, Z. L. Zhang, Z. G. Wang, Z. Q. Tian, G. P. Wang and D. W. Pang, «Fast and High-Accuracy Localization for Three-Dimensional Single-Particle Tracking,» *Scientific Reports*, vol. 3, n. 2462, pp. 1-5, 2013.
- [157] A. Martinez-Marrades, J. F. Rupprecht, M. Gross and G. Tessier, «Stochastic 3D optical mapping by holographic localization of Brownian scatterers,» *Optics Express*, vol. 22, n. 23, pp. 29191-29203, 2014.
- [158] F. A. Kruse, A. B. Lefkoff, J. W. Boardman, K. B. Heidebrecht, A. T. Shapiro, P. J. Barloon and A. F. H. Goetz, «The Spectral Image Processing System (SIPS)-Interactive Visualization and Analysis of Imaging Spectrometer Data,» *Remote Sensing of Environment*, vol. 44, n. 2-3, pp. 145-163, 1993.
- [159] S. Anidjar, J. L. Salzmann, D. Gentric, P. Lagneau, J. P. Camilleri and J. B. Michel, «Elastase-induced experimental aneurysms in rats,» *Circulation*, vol. 82, n. 3, pp.

973-981, 1990.

- [160] F. Rouzet, L. Bachelet-Violette, J. M. Alsac, M. Suzuki, A. Meulemans, L. Louedec, A. Petiet, M. Jandrot-Perrus, F. Chaubet, J. B. Michel, D. L. Guludec and D. Letourneur, «Radiolabeled fucoidan as a p-selectin targeting agent for in vivo imaging of platelet-rich thrombus and endothelial activation,» *J Nucl Med.*, vol. 52, n. 9, pp. 1433-1440, 2011.
- [161] L. Bachelet, I. Bertholon, D. Lavigne, R. Vassy, M. Jandrot-Perrus, F. Chaubet and D. Letourneur, «Affinity of low molecular weight fucoidan for P-selectin triggers its binding to activated human platelets,» *Biochimica et Biophysica Acta (BBA) - General Subjects*, vol. 1790, n. 2, pp. 141-146, 2009.
- [162] Sophie Richard , Véronique Eder , Gianvito Caputo , Clément Journé , Phalla Ou , Julie Bolley , Liliane Louedec , Erwann Guenin , Laurence Motte , Nicola Pinna & Yoann Lalatonne, «USPIO size control through microwave nonaqueous sol-gel method for neoangiogenesis T2 MRI contrast agent,» *Nanomedicine*, vol. 11, n. 21, 2016.
- [163] H. Maeda , J. Wu , T. Sawa , Y. Matsumura , K. Hori, «Tumor vascular permeability and the EPR effect in macromolecular therapeutics: a review,» *Journal of Controlled Release*, vol. 65, p. 271–284, 2000.
- [164] A. Varki, «Sialic acids in human health and disease,» *Trends Mol Med*, vol. 14, n. 8, p. 351–360, 2008.
- [165] H. Maeda, T. Sawa and T. Konno, « Maeda H, Sawa T, Konno T. Mechanism of tumor-targeted delivery of macromolecular drugs, including the EPR effect in solid tumor and clinical overview of the prototype polymeric drug SMANCS,» *J Control Release*, vol. 74, pp. 47-61, 2001.
- [166] N. Bertrand, J. Wu, X. Xu, N. Kamaly and O. C. Farokhzad, «Cancer nanotechnology: the impact of passive and active targeting in the era of modern cancer biology,» *Adv. Drug Deliv*, vol. 66, pp. 2-25, 2014.
- [167] X. Yu, I. Trase, M. Ren, K. Duval, X. Guo and Z. Chen, «Design of Nanoparticle-Based Carriers for Targeted Drug Delivery,» *J Nanomater*, 2016.
- [168] L. Y. Chou, K. Ming and W. C. Chan, «Strategies for the intracellular delivery of nanoparticles,» *Chem. Soc. Rev.*, vol. 40, p. 233–245, 2011.
- [169] A. Albanese, P. S. Tang and W. C. Chan , «The effect of nanoparticle size, shape, and surface chemistry on biological systems,» *Annu. Rev. Biomed. Eng.*, vol. 14, p. 1–16, 2012.
- [170] Y. Li, M. Kröger and W. K. Liu, «Shape effect in cellular uptake of pegylated nanoparticles: comparison between sphere, rod, cube and disk,» *Nanoscale*, vol. 7,

- p. 16631–16646, 2015.
- [171] A.C. Croce and G. Bottioli, «Autofluorescence Spectroscopy and Imaging: A Tool for Biomedical Research and Diagnosis,» *Eur J Histochem.*, vol. 58, n. 4, p. 2461, 2014.
- [172] P. A. Jarzyna, A. Gianella, T. Skajaa, G. Knudsen, L. H. Deddens, D. P. Cormode, Z. A. Fayad and W. J. Mulder, «Multifunctional imaging nanoprobe,» *Wiley Interdiscip Rev Nanomed Nanobiotechnol*, vol. 2, n. 2, pp. 138-150, 2010.
- [173] S. Mitragotri and J. Lahann, «Physical approaches to biomaterial design,» *Nature Materials*, vol. 8, pp. 15-23, 2009.
- [174] G. Wu, P. Li, H. Feng, X. Zhang and P. K. Chu, «Engineering and functionalization of biomaterials via surface modification,» *J. Mater. Chem. B*, vol. 3, pp. 2024-2042, 2015.
- [175] M. A. Garcia, J. M. Merino, E. F. Pinel, A. Quesada, J. D. L. Venta, M. L. R. Gonzalez, G. R. Castro, P. Crespo, J. Liopis, J. M. Gonzalez-Calbet and A. Hernando, «Magnetic Properties of ZnO Nanoparticles,» *Nano Letters*, vol. 7, pp. 1489-1494, 2007.
- [176] T. T. John, K. R. Priolkar, A. Bessiere, P. R. Sarode and B. Viana, «Effect of [OH-] Linkages on Luminescent Properties of ZnO Nanoparticles,» *Journal of Physical Chemistry C*, vol. 115, pp. 18070-18075, 2011.
- [177] O. Lupan, T. Pauporté, T. L. Bahers, I. Ciofini and B. Viana, «High Aspect Ratio Ternary Zn<sub>1-x</sub>Cd<sub>x</sub>O Nanowires by Electrodeposition for Light-Emitting Diode Applications,» *Journal of Physical Chemistry C*, vol. 115, n. 30, pp. 14548-14558, 2011.
- [178] O. Lupan, T. Pauporte, L. Chow, B. Viana, F. Pelle, L. K. Ono, B. R. Cuenya and H. Heinrich, «Effects of annealing on properties of ZnO thin films prepared by electrochemical deposition in chloride medium,» *Applied Surface Science*, vol. 256, pp. 1895-1907, 2010.
- [179] Z. Y. Zhang and H. M. Xiong, «Photoluminescent ZnO Nanoparticles and Their Biological Applications,» *Materials*, vol. 8, n. 6, pp. 3101-3127, 2015.
- [180] J. Cheon and J. H. Lee, «Synergistically Integrated Nanoparticles as Multimodal Probes for Nanobiotechnology,» *Accounts of Chemical Research*, vol. 41, n. 12, pp. 1630-1640, 2008.
- [181] V. J. Pansare, S. Hejazi, W. J. Faenza and R. K. Prud'homme, «Review of Long-Wavelength Optical and NIR Imaging Materials: Contrast Agents, Fluorophores, and Multifunctional Nano Carriers,» *Chemistry of Materials*, vol. 24, n. 5, pp. 812-827, 2012.

- [182] P. Wunderbaldinger, L. Josephson and R. Weissleder, «Tat Peptide Directs Enhanced Clearance and Hepatic Permeability of Magnetic Nanoparticles,» *Bioconjugate Chemistry*, vol. 13, n. 2, pp. 264-268, 2002.
- [183] Y. Wu, J. Guo, W. Yang, C. Wang and S. Fu, «Preparation and characterization of chitosan–poly(acrylic acid) polymer magnetic microspheres,» *Polymer*, vol. 47, n. 15, pp. 5287-5294, 2006.
- [184] I. L. Hsiao and Y. J. Huang, «Titanium Oxide Shell Coatings Decrease the Cytotoxicity of ZnO Nanoparticles,» *Chemical Research in Toxicology*, vol. 24, n. 3, pp. 303-313, 2013.
- [185] N. H. Cho, T. C. Cheong, J. H. Min, J. H. Wu, S. J. Lee, D. Kim, J. S. Yang, S. Kim, Y. K. Kim and S. Y. Seong, «A multifunctional core–shell nanoparticle for dendritic cell-based cancer immunotherapy,» *Nature Nanotechnology*, vol. 6, pp. 675-682, 2011.
- [186] T. Dietl, H. Ohno, F. Matsukura, J. Cibert and D. Ferrand, «Zener model description of ferromagnetism in zinc-blende magnetic semiconductors,» *Science*, vol. 287, n. 5455, pp. 1019-22, 2000.
- [187] V. Filipe, A. Hawe and W. Jiskoot, «Critical Evaluation of Nanoparticle Tracking Analysis (NTA) by NanoSight for the Measurement of Nanoparticles and Protein Aggregates,» *Pharm Res.*, vol. 27, n. 5, pp. 796-810, 2010.
- [188] T. Wagner, H. G. Lipinski and M. Wiemann, «Dark field nanoparticle tracking analysis for size characterization of plasmonic and non-plasmonic particles,» *J Nanopart Res*, vol. 16, n. 2419, 2014.
- [189] C. Y. Soo, Y. Song, Y. Zheng, E. C. Campbell, A. C. Riches, F. Gunn-Moore and S. J. Powis, «Nanoparticle tracking analysis monitors microvesicle and exosome secretion from immune cells,» *Immunology*, vol. 136, n. 2, p. 192–197, 2012.
- [190] R. A. Dragovic, C. Gardiner, A. S. Brooks, D. S. Tannetta, D. J. P. Ferguson, P. Hole, B. Carr, C. W. G. Redman, A. L. Harris, P. J. Dobson, P. Harrison and I. L. Sargent, «Sizing and phenotyping of cellular vesicles using Nanoparticle Tracking Analysis,» *Nanomedicine*, vol. 7, n. 6, pp. 780-788, 2011.
- [191] Gringer, 2009. [Online]. Available: [https://en.wikipedia.org/wiki/Transmission\\_electron\\_microscopy](https://en.wikipedia.org/wiki/Transmission_electron_microscopy).
- [192] B. Chu, «Laser Light Scattering: Basic Principles and Practice,» in *Optical mixing spectrometers*, Academic Press, Inc, 1991, p. 83.
- [193] M. W. Davidson, «microscopyu.com,» National High Magnetic Field Laboratory, 2016. [Online]. Available: <https://www.microscopyu.com/microscopy->

basics/resolution.

- [194] M. Kass and A. Ivaska, «Spectrophotometric determination of iron(III) and total iron by sequential injection analysis technique,» *Talanta*, vol. 58, n. 6, pp. 1131-1137, 2002.

## **Appendix A. Characterization techniques**

### **Transmission electron microscopy**

Transmission electron microscopy (TEM) is a very useful tool for materials nanotechnology, semiconductor and medicine research because of its extremely high resolution. The shape and average size of the NPs can be determined quickly. Compared to optical microscopy, TEM has a much better in resolution because the wavelength of the electron beam, used as a wave, is much shorter than that of the visible light. The resolution of a TEM is about 0.2 nm.

An electron gun uses a high voltage source (typically ~100-300 kV) to emit electrons either by thermionic or field electron emission into the vacuum. Electrons are selected to have a relatively narrow energy distribution, which is to have a beam reasonably monochromatic. Similarly to an optical microscope, the incident beam is shaped by a condenser. It then hits and passes through the sample. Other lenses play the role of the objective and the scattered electrons excite a fluorescent screen which produces a visible image. This visible image is recorded by a CCD camera. The layout of optical components in a basic TEM is shown in Figure A.1 [191]. The electron microscope is a lot more complex than the optical microscope. The electron beam needs a good vacuum to propagate into. Electrons interact and repulsion makes the beam self-defocusing. The lenses are in fact magnetic fields whose shapes are controlled by electrical currents. Good lenses are a lot more difficult to obtain than the polished glass lenses used in optical microscopes and TEM usually suffer from spherical aberration. However, since everything is defined through electrical currents, microcontrollers and good software can make the instrument extremely versatile.

The main drawback is that samples must be very thin in order not to intercept the beam too much, about 100 nm thick, which is difficult to attain with biological samples. On the other side, if the sample is too clear, one must enhance the contrast with heavy atoms.

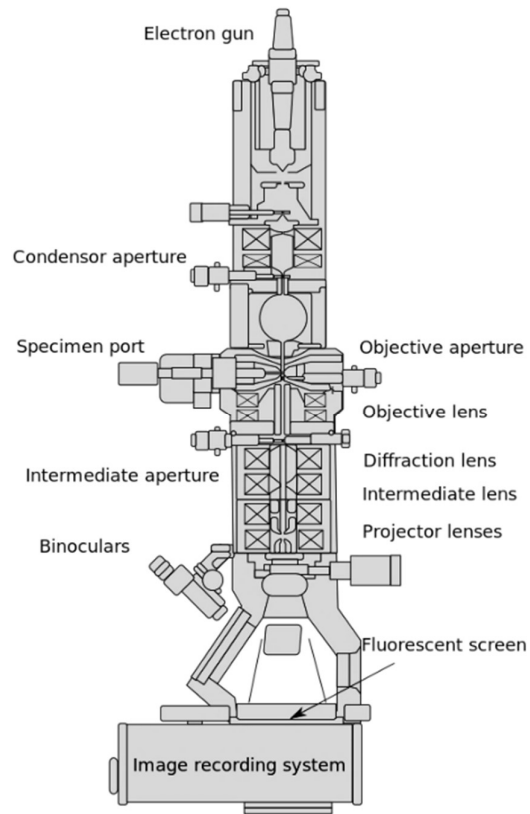


Figure A.1. Layout of optical components in a basic TEM.

### X-ray diffraction

X-ray diffraction (XRD) is an analytical technique used for phase identification of a crystalline material and collecting information on unit cell dimensions. When an incident beam of monochromatic X-rays interacts with a target material, those X-rays are scattered from atoms in the target material. If the target materials have regular structure (i.e. crystalline, see Figure A.2), there are constructive interference in some specific directions when Bragg's law is satisfied:

$$2d \sin \theta = n\lambda \quad (\text{A.1})$$

where:  $n$  is an integer,

$d$  is the spacing between diffracting planes,

$\theta$  is the incident angle,

$\lambda$  is the wavelength of the beam.

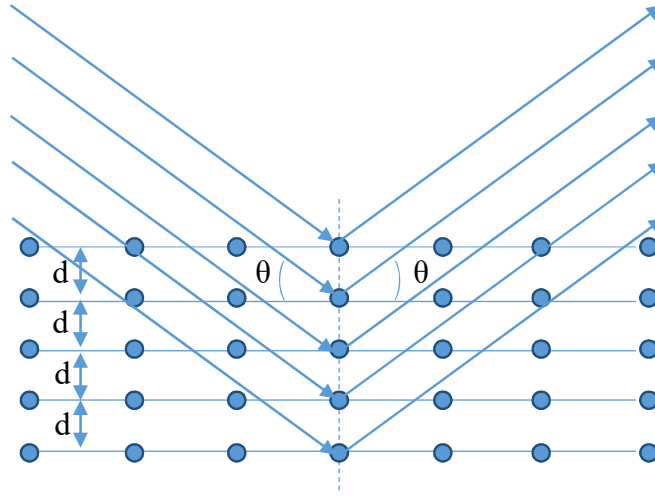


Figure A.2. X-rays scattered by crystal.

A powder X-ray diffractometer consists of an X-ray source, a sample holder, a detector and a way to vary angle  $\theta$ . A narrow parallel monochrome X-ray beam is focused on the sample at angle  $\theta$ , while the detector reads the intensity of the diffracted X-ray at angle  $2\theta$  (see Figure A.3). For typical powder diffractograms, data is collected at  $2\theta$  from  $\sim 5^\circ$  to  $70^\circ$ .

The crystalline size of NPs is calculated using the most intense peak by Scherrer's formula.

$$D = \frac{K\lambda}{\beta_{hkl} \cos \theta} \tag{A.2}$$

- where:
- $D$  is the size of the axis parallel to Bragg plane (hkl),
  - $K$  is a constant with a typical value of 0.9 for spherical particle,
  - $\lambda$  is the wavelength of radiation,
  - $\beta_{hkl}$  is the full width half maximum (FWHM) in radians,
  - $\theta$  is the position of the diffraction peak maximum.

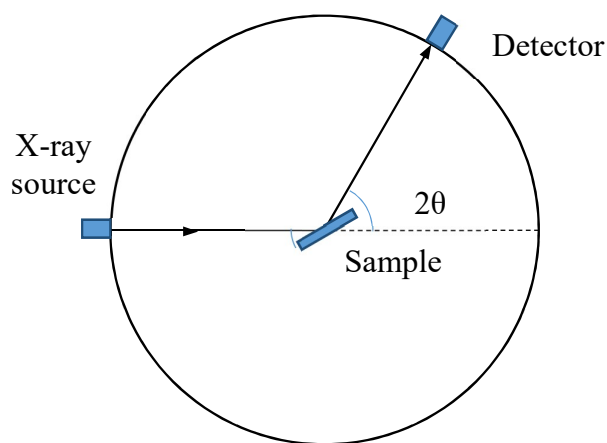


Figure A.3. Schematic diagram of X-ray diffractometer.

### Fluorescence spectroscopy

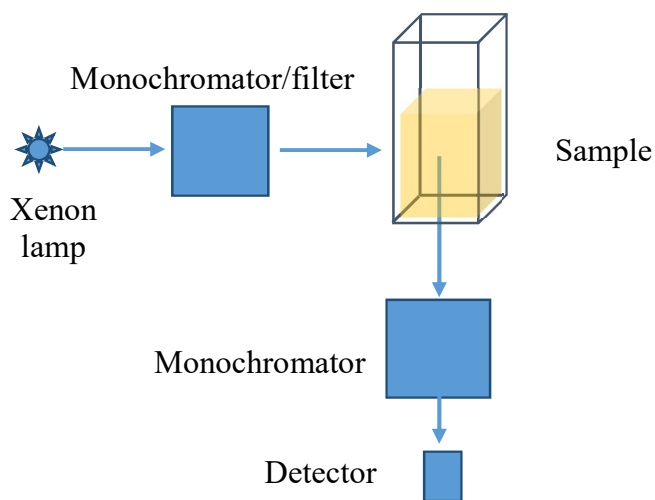


Figure A.4. Schematic diagram of fluorescence spectrophotometer.

Fluorescence spectroscopy analyses fluorescence from a sample. The sample is excited by an excitation light beam and it emits fluorescent light. Schematic diagram of fluorescence spectrophotometer is shown in Figure A.4. All fluorescence instruments contain three basic items: a source of light, one or more monochromators and a detector. The light source has often a broad emission spectrum. It can be a xenon lamp or a halogen lamp. The light emitted by the broad spectrum lamp passes through a monochromator (or filters) for selecting the excitation light. A monochromatic laser beam can be used as a high intensity excitation source, with a very narrow spectral width. Another monochromator analyses the emission spectrum of the sample.

The light source is in a 90-degree angle with the detector to avoid light from excitation beam from hitting directly the detector with high power. Linear scattering occurs in the sample, but can easily be dealt with by the use of rejection filters. Sensitive detectors such as a photomultiplier tube, an avalanche photodiode or a CCD camera record the fluorescence light from the sample.

### Dynamic light scattering

Dynamic Light Scattering (DLS, also known as Photon Correlation Spectroscopy) is a light scattering technique which allows NPs sizing down to 1 nm diameter. The basic principle is simple: The sample is illuminated by a laser beam and the fluctuations of the scattered light are detected at a known scattering angle  $\theta$  by a fast photon detector (Figure A.5).

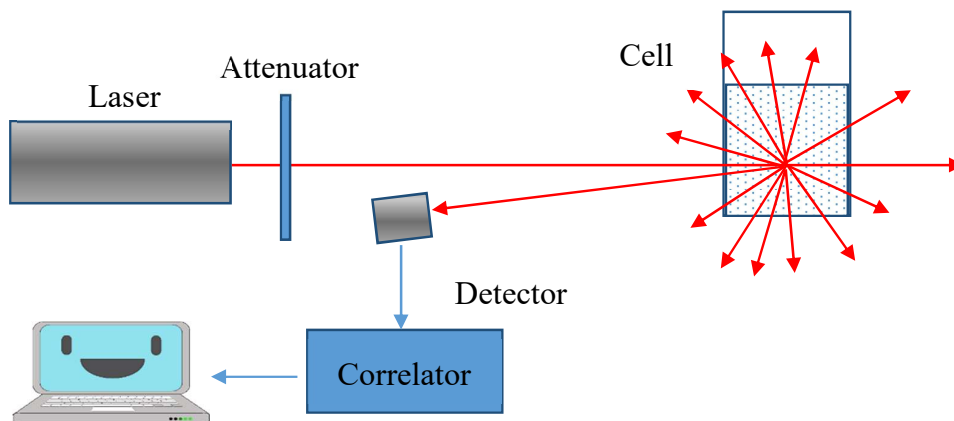


Figure A.5. Schematic diagram of DLS.

Simple DLS instruments that measure at a fixed angle can determine the average size of NPs in a limited size range. More sophisticated instruments which combine multi-angle detectors can determine a large range of particle size distributions.

By analysing the fluctuation of the scattered light, intensity correlation function  $g^{(2)}(t)$  can be calculated as equation A.3 [192].

$$g^{(2)}(\tau) = \frac{\langle I(t)I(t+\tau) \rangle}{\langle I(t) \rangle^2} \quad (\text{A.3})$$

where  $I(t)$  and  $I(t + \tau)$  are the intensities of the scattered light at time  $t$  and at a delayed time  $t + \tau$ . The braces indicate averaging over  $t$ .

If the sample is monodisperse then the decay is simply a single exponential:

$$g^{(2)}(\tau) = B + \beta \exp(-2\Gamma\tau) \quad (\text{A.4})$$

where:  $B$  is the baseline of the correlation function at infinite delay,  
 $\beta$  is the correlation function amplitude at zero delay,  
 $\Gamma = q^2D$  is the decay rate.

The diffusion coefficient  $D$  can be derived from the decay rate  $\Gamma$  at a single angle (or at a range of angles) depending on the wave vector  $q$ :

$$q = \frac{4\pi n_0}{\lambda} \sin \frac{\theta}{2} \quad (\text{A.5})$$

where:  $n_0$  is the refractive index of the sample.

Using diffusion coefficient  $D$  measurement, a particle size distribution can be determined via the Stokes-Einstein formula:

$$D = \frac{k_B T}{3\pi\eta d} \quad (\text{A.6})$$

where:  $D$  is the diffusion coefficient,  
 $k_B$  is the Boltzmann constant ( $1.38 \times 10^{-23}$  J/K),  
 $T$  is the temperature,  
 $\eta$  is the viscosity of the dispersion medium,  
 $d$  is a hydrodynamic diameter.

Hydrodynamic diameter is an effective diameter including both the diameter of the core particle and the diameter of layers on its surface. These layers can include polymers, electrical charges, actively interacting with the particle. In general, it will be larger than the TEM measured diameter.

### **Vibrating sample magnetometer**

A vibrating sample magnetometer (VSM) is a scientific instrument that measures magnetic properties of a material, invented in 1955 by Simon Foner at Lincoln Laboratory of the MIT.

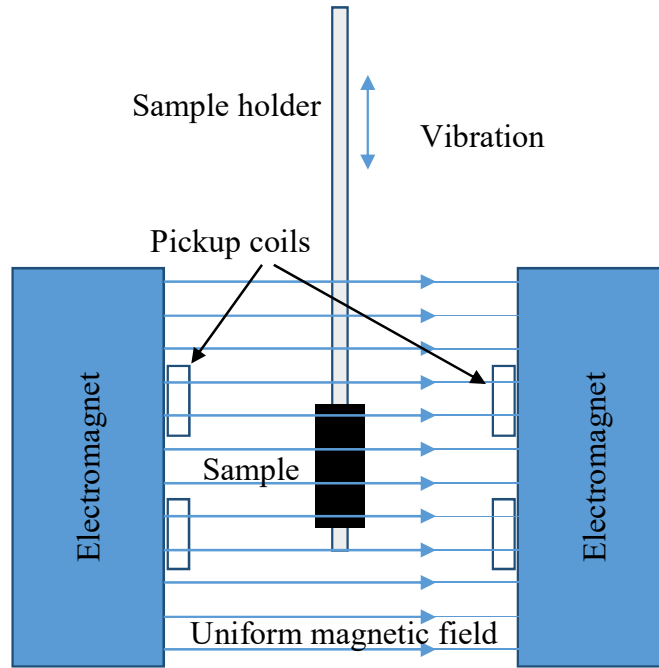


Figure A.6. Schematic diagram of a vibrating sample magnetometer.

Schematic diagram of a vibrating sample magnetometer is described in Figure A.6. A sample is magnetized when placed inside a uniform magnetic field that is generated by an electromagnet or a superconducting magnet. Then the sample is mechanically excited by vibrating piezoelectric actuators. When the magnetized sample moves near the pickup coil, it changes the magnetic field and the magnetic flux  $\Phi_B$  through the coil. According to Faraday's Law, the induced voltage generated in the coil is shown in equation A.7:

$$\varepsilon = -N \frac{d\Phi_B}{dt} \quad (\text{A.7})$$

where:  $\varepsilon$  is the induced voltage,

$N$  is the total number of turns of the loop,

$\Phi_B = B.A$ , ( $B$  is the magnetic field,  $A$  is the area of the loop),

$t$  is the time.

This voltage is proportional to the sample's magnetic moment. In a typical setup, the induced voltage is measured by using of a lock-in amplifier with the piezoelectric excitation signal as a reference. By changing strength of the applied magnetic field, it is possible to obtain the hysteresis curve of the sample's material.

## Appendix B. Microscopy basics

Microscope is an optical device used for imaging small specimens with high-resolution. Image quality mostly depends on the objective of the microscope, which determines the resolution of images. Here are some basic properties of microscope such as resolution, magnification, and type of illumination.

### Resolution

The resolution of an optical system isn't the number of pixels in its output images. It is defined as the shortest distance between two points on the image the observer can still distinguish.

For example, in Figure B.1, two airy diffraction patterns can be easily distinguished (a), still can be distinguished when they are not too close (b), and cannot be distinguished if the distance becomes too small (c).

The ultimate resolution of a microscope ( $d$ ) is determined by the wavelength of the radiation light ( $\lambda$ ), and the numerical aperture ( $NA$ ) of its light collecting system. It is mathematically given by the Abbe's formula B.1 [193]:

$$d = \frac{\lambda}{2NA} \quad (\text{B.1})$$

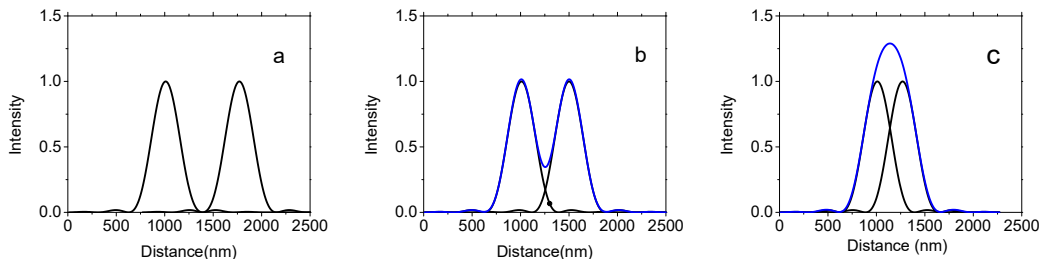


Figure B.1. Airy patterns and the limit of resolution.

For real, the resolution limit is somewhat greater than its theoretical limit because practical realization isn't perfect. For example, we can notice optical aberration of the lenses, misalignment of different subsystems, and so on.

$NA$  is the ability for collecting light by a lens. A high  $NA$  objective allows more efficient light harvesting. It gives better images. The  $NA$  value of a lens is calculated as equation B.2:

$$NA = n \sin \theta \tag{B.2}$$

where:  $n$  is the index of refraction of the medium in which the lens is working,  
 $\theta$  is the maximal half-angle of the cone of light that can enter or exit the lens.

A microscope objective with a higher  $NA$  needs to be closer to the object than a lower  $NA$  one.  $NA$  values above 1.0 also indicate that the lens is immersed in a fluid, instead of air, which fills the small gap between it and the sample. Fluid immersion makes a better optical interface than air.

Of course, shorter wavelengths will provide a better resolution. However, we have strong limits: usual optical systems aren't friendly with UV light, and biological objects are easily damaged by short wavelength.

Can we beat this resolution limit?

Figuratively speaking, we can imagine we have a small genie in our bottle, a small oracle in our microscope. We have more than the usual three wishes; in fact we have as many wishes as we want. He's a good genie as he is honest and doesn't try to mislead us. However, he is inflexible. As long as we ask anything wavey, it answers with the Abbe limit. If we want anything better, we must try other kinds of questions.

We are certain that *any* structure in the object emits a characteristic signal. The genie has access to virtually an unlimited quantity of information. However, most of it is lost when the wave propagates towards our detector.

Is it possible to get some parts of this complex information before it blurs away in the propagating wave? Yes, if we can take the information directly from the genie's hands. It's called "near field microscopy". A local probe catches the transient evanescent signals and allows them to propagate, in the probe, to the detector. This technique however is strictly limited close to nice surfaces. Soft materials are difficult to deal with and one can only look at a very small volume as the field of depth is very restricted.

We can proceed differently. Instead of trying to cheat the genie when collecting the answers, ask him very precise questions. If one has a way to create a "source" inside the sample, smaller than the Abbe limit, light collected from it is guaranteed to come from this

small region. Many clever ways have been devised for the “sources” and sub-resolution microscopy is a booming field now.

The problem now is that we have to pave the observation volume with those sources, often millions of them (experienced people will ask many questions in parallel). We can systematically scan the volume, or follow some tiny particles which move and interact with the sample thus relaying some information to us. Anyways, we have to collect a huge amount of “images”, process the useful signal from them, and fuse them in a big picture.

At this point, we have to get our own small genie. We have to train him to interact with the optical genie and to process all the individual tiny bits of information into a workable image. This small genie is usually called “software”. This genie is often maliciously compliant. You get the wrong answer as soon as the question is asked in a way which let the genie interpret it differently from your real intention. But at least, you can debug it and earn your nice images.

As a side note, this leads us to a common question people may ask to the programmer: are you sure your results are correct? No. I can't be. The thing can process billions of instructions per second. A single image needs minutes, even hours, of processing. No one can do it “by hand”. However, with proper unit test, and with known limit cases, one can have a good confidence in the software's results.

### **Magnification**

Magnification of a microscope depends on the magnifying power of both the objective and the ocular piece.

Total magnification (M) is normally simply the product of the two, as equation B.3:

$$M = M_{objective} \times M_{ocular} \quad (B.3)$$

Usual objective magnification power ranges from 4X to 100X and the common oculars magnification is 10X. As a result, the total magnification of a microscope ranges from 40X to 1000X. In fact, the useful magnification is limited by the Abbe limit on resolution. Best microscope can go up to 800X with air objectives and a little more than 1000X using immersion ones. The magnification factor is more useful for commercial purposes. Scientific imaging is more prone to use the resolution as its yardstick.

## **Bright field illumination**

Bright field illumination is very popular in optical microscopy. It corresponds to the first microscopes, which were designed as early as the 17th century. It is the simplest and most intuitive technique and it is still the most used setup today. A typical bright field illumination image has a dark sample with a white background. Some types of bright field illumination configurations are shown in Figure B.2.

There are four main components in bright field illumination:

- + The light Source can be any kind of source such as a laser, a halogen lamp, a xenon lamp or a light-emitting diode. The simplest setup just uses the sun reflected in a mirror.
- + Condenser Lens: focuses light from light source to the sample.
- + Objective Lens: collects light from the sample.
- + Eyepiece/Camera: views or records the image.

The bright field illumination technique is simple. However, it has some disadvantages. The most important one is that it provides low contrast images. No signal corresponds to the light's maximum intensity. The sample absorbs whatever light corresponds to its optical thickness and, usually, transmitted light is far from zero. We cannot amplify the useful signal as the bright empty field is already near the sensor saturation. We cannot use the full dynamic range of the sensor, hence the bad contrast. This technique is suitable for thick and big samples, but not for thin and small ones.

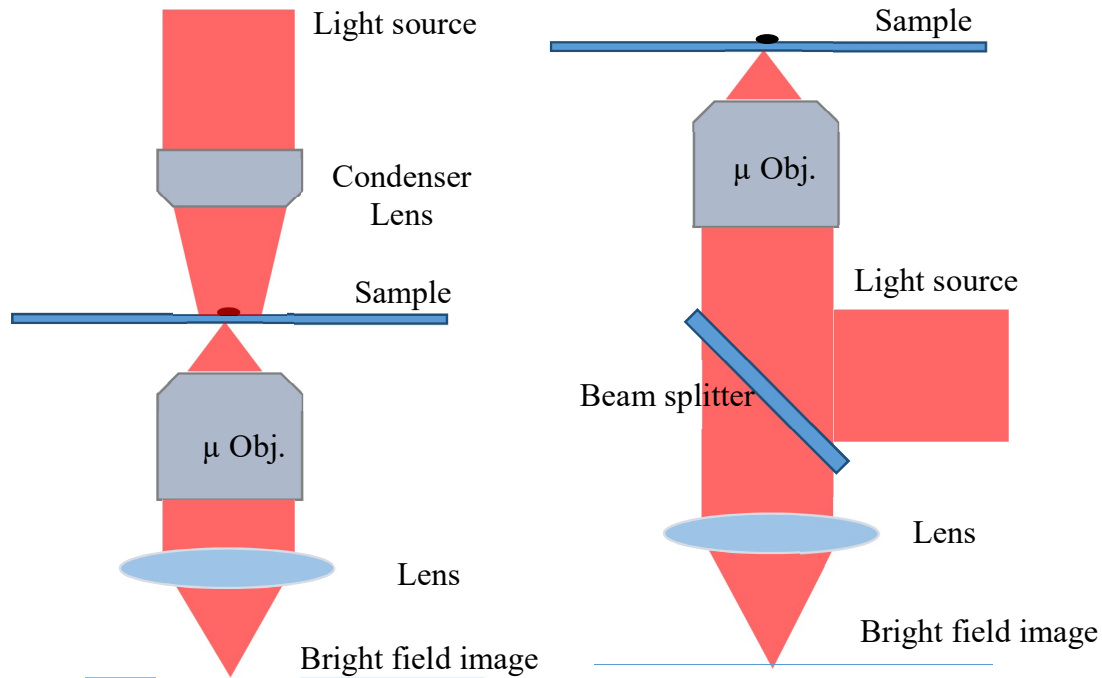


Figure B.2. Some type of bright field illumination configurations: transmission (left) and reflection (right).

### Dark field illumination

Dark field illumination is an arrangement such that the light source cannot directly hit the camera or the eyepiece. When light hits an object, it is scattered in all directions. The design of the dark field microscope removes the non-scattered light from light source and just only collects the scattered light from samples.

A dark field microscope can provide beautiful and amazing images. The dark field illumination image has a bright sample with a black background. No signal now corresponds to zero, the black background. Even if the objects scatter little light, we can have amplification in the detector. Even if amplifications bring its own noise (you see video noise if you take photographs in a dark environment), this technique is a far better use of the sensor's dynamic range than the previous white field technique. A dark field microscope is ideal for viewing objects that are unstained, transparent and absorb little or no light such as fibers, minerals, ceramics, thin polymers, NPs, living bacteria, mounted cells and tissues. Offering a very high contrast, this microscope can allow us to detect very small target, even as small as NPs.

Besides the above mentioned advantages, dark field microscopy suffers from some drawbacks:

- + It is not suitable for thick specimen,
- + The slides must be cleaned very carefully to get rid of small particles such as dust.
- + Control and operation are more complicated than those required by bright field.

Dark field microscopy has many applications. It could be a wonderful observation tool, especially when combined with other enhancements.

### **Conversion of a microscope from bright field to dark field**

A bright field microscope can be converted to a dark field microscope by using proper optical element such as a condenser with a beam stopper, or with an external light source. Some dark field kits are commercially available for this retrofit of a classical microscope.

In Figure B.3, the left-hand side shows a setup which is commonly used for commercial dark field microscopes. It is the most popular configuration because it is compact and requires minimal modifications in the microscope. The right-hand side configuration for a dark field microscope is usually used as a homemade microscope because it has a good ability to collect light, is inexpensive and offers further upgradability, even if its intrinsic resolution is a little worse than the one offered by the first configuration.

Figure B.4 indicates the difference between a bright field image and a dark field one in term of contrast.

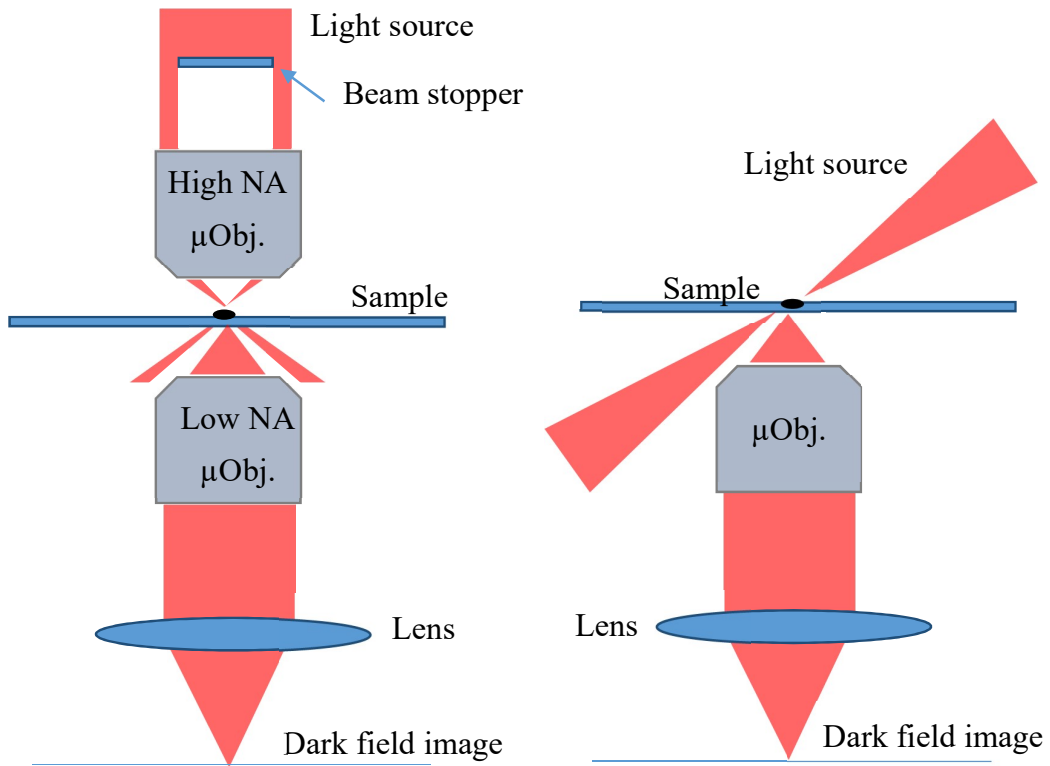


Figure B.3. Some types of dark field illumination configuration.



Figure B.4. Bright field illumination image (left) and dark field illumination image (right) of vessel.

### Appendix C. List of synthesis NPs experiments

Table C.1. List of synthesis NPs experiments in DEG

R <sub>Fe, i</sub> (%)	Compound (mol)	Drying	N <sub>2</sub>	Solvent	Temp. (°C)	Time (h)	Yield (*)	Coating	Analysis
0	Zn(Ac) <sub>2</sub> : 0.02	Vacuum	no	DEG	Reflux	6	**	no	Xray, TEM
0.01	Zn(Ac) <sub>2</sub> : 0.02 Fe(Ac) <sub>2</sub> : 0.0002	Vacuum	no	DEG	Reflux	6	**	no	TEM
0.1	Zn(Ac) <sub>2</sub> : 0.02 Fe(Ac) <sub>2</sub> : 0.002	Vacuum	no	DEG	Reflux	6	**	no	Xray, TEM
0.2	Zn(Ac) <sub>2</sub> : 0.02 Fe(Ac) <sub>2</sub> : 0.004	Vacuum	no	DEG	Reflux	6	**	no	TEM
0.05	Zn(Ac) <sub>2</sub> : 0.019 Fe(Ac) <sub>2</sub> : 0.001	toluene	yes	DEG	230	4	***	Yes	Xray, TEM
0.1	Zn(Ac) <sub>2</sub> : 0.018 Fe(Ac) <sub>2</sub> : 0.02	toluene	yes	DEG	230	4	***	no	AAS
0.15	Zn(Ac) <sub>2</sub> : 0.017 Fe(Ac) <sub>2</sub> : 0.03	toluene	yes	DEG	230	4	***	Yes	Xray

0.2	Zn(Ac) <sub>2</sub> : 0.016 Fe(Ac) <sub>2</sub> : 0.004	Toluene	yes	DEG	246	4	***	no	Xray TEM AAS
0.35	Zn(Ac) <sub>2</sub> : 0.013 Fe(Ac) <sub>2</sub> : 0.007	toluene	yes	DEG	230	4	***	Yes	Xray
0.5	Zn(Ac) <sub>2</sub> : 0.01 Fe(Ac) <sub>2</sub> : 0.01	toluene	yes	DEG	230	4	*****	Yes	Xray, TEM
0.5	Zn(Ac) <sub>2</sub> : 0.01 Fe(Ac) <sub>2</sub> : 0.01	toluene	yes	DEG	240	4	*****	Yes	VSM
0.5	Zn(Ac) <sub>2</sub> : 0.01 Fe(Ac) <sub>2</sub> : 0.01	Toluene	yes	DEG	Reflux	4	*****	yes	Xray, TEM, AAS

Table C.2. List of synthesis NPs experiments in PG

R <sub>Fe,i</sub> (%)	Compound (mol)	Drying	N <sub>2</sub>	Solvent	Temp. (°C)	Time (h)	Yield (*)	Coating	Analysis
0	Zn(Ac) <sub>2</sub> : 0.03	no	yes	PG	Reflux	2	*****	no	TEM
0	Zn(Ac) <sub>2</sub> : 0.03	Toluene	yes	PG	Reflux	2	*****	no	TEM
0	Zn(Ac) <sub>2</sub> : 0.02	Toluene	yes	PG	Reflux	2	*****	no	TEM
5	Zn(Ac) <sub>2</sub> : 0.02 Fe(Ac) <sub>2</sub> : 0.001	Toluene	yes	PG	Reflux	2	*****	no	AAS
10	Zn(Ac) <sub>2</sub> : 0.018 Fe(Ac) <sub>2</sub> : 0.02	toluene	yes	PG	188	2	*****	no	AAS
20	Zn(Ac) <sub>2</sub> : 0.016 Fe(Ac) <sub>2</sub> : 0.004	Toluene	yes	PG	188	2	*****	no	Xray, TEM, AAS
50	Zn(Ac) <sub>2</sub> : 0.01 Fe(Ac) <sub>2</sub> : 0.01	toluene	yes	PG	187	2	*****	no	VSM AAS

Table C.3. List of synthesis NPs experiments in mixture of DEG/PG

R <sub>Fe,i</sub> (%)	Compound (mol)	Drying	N <sub>2</sub>	Solvent	Temp. (°C)	Time (h)	Yield (*)	Coating	Analysis
5	Zn(Ac) <sub>2</sub> : 0.019 Fe(Ac) <sub>2</sub> : 0.001	toluene	yes	DEG: 60 PG: 30	220	4	*****	no	AAS
30	Zn(Ac) <sub>2</sub> : 0.02 FeCl <sub>2</sub> : 0.01	toluene	yes	DEG: 80 PG: 40	220	4	*	no	
50	Zn(Ac) <sub>2</sub> : 0.01 Fe(Ac) <sub>2</sub> : 0.01	toluene	yes	DEG: 65 PG: 15	190	4	*****	no	AAS
50	Zn(Ac) <sub>2</sub> : 0.01 Fe(Ac) <sub>2</sub> : 0.01	toluene	yes	DEG: 80 PG: 5	240	4	*****	no	AAS
67	Zn(Ac) <sub>2</sub> : 0.005 Fe(Ac) <sub>2</sub> : 0.01	Toluene	yes	DEG: 60 PG: 30	218	4	*****	no	AAS

## Appendix D. Synthesis of ZnO NPs in PG without azeotropic distillation

0.02 mol of zinc acetate dehydrate ( $\text{Zn}(\text{CO}_2\text{CH}_3)_2 \cdot 2\text{H}_2\text{O}$ , 98.0%), was dissolved in 80 ml of PG heated to reflux ( $187^\circ\text{C}$ ). In this synthesis, we did not use  $\text{Na}^+$  and there is unknown amount of water in acetate salt and PG solution. After 2 hours, a suspension of NPs was obtained. The chemical reaction in PG can produce NPs with very high yield (>98%). The weight of NPs obtained after synthesis is a little heavier than calculated theory weight. The TEM images show the mean size of PG-ZnO NPs is 120 nm (Figure D.1).

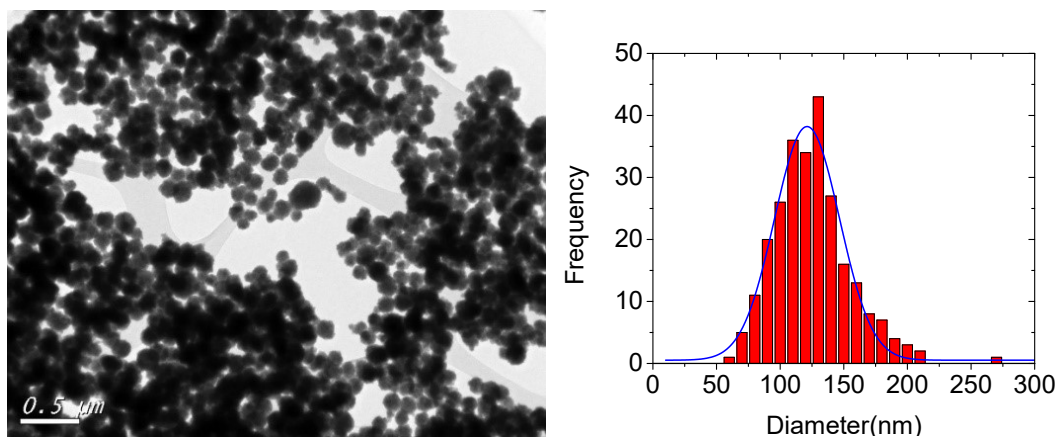


Figure D.1. TEM images and size distribution of PG-ZnO NPs with water.

## Appendix E. Synthesis of NPs in DEG without azeotropic distillation

Zn(Fe)O NPs ( $R_{Fe} = (0, 0.01, 0.1 \text{ and } 0.20)$ ) were synthesized with DEG as solvent. 0.02 mol of zinc acetate and iron II acetate was dissolved in 80 ml of DEG. The solution was heated to reflux. After 4 hours, a suspension of NPs was obtained. The influent of catalyst  $\text{Na}^+$  to size and crystalline quality were also investigated.

### With catalysts

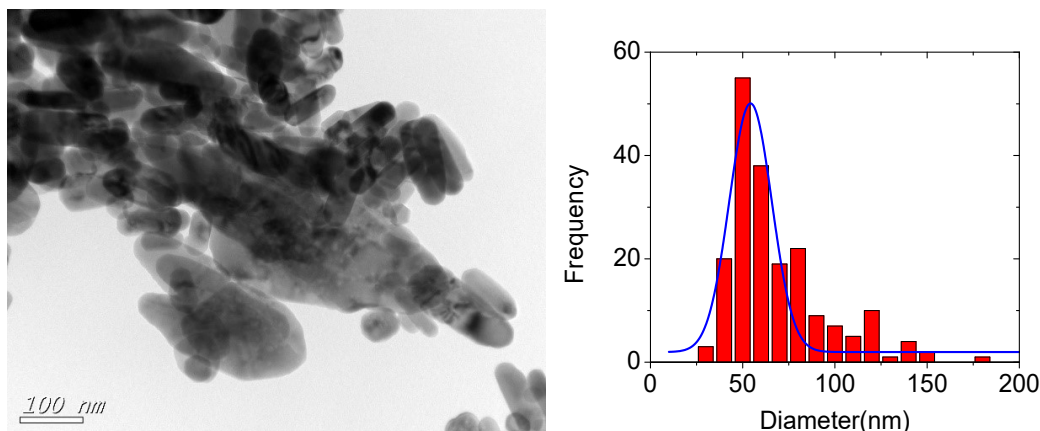


Figure E.1. TEM image and size distribution of DEG-ZnO NPs with catalysts.

ZnO NPs were synthesized with catalyst  $\text{Na}^+$  (NaOH, NaAc). In TEM images indicated that the average diameter of NPs is about 50 nm with broadband distribution (Figure E. 1). The shape of NPs is rod with the length up to hundreds nanometer. The XRD spectral show the crystal quality of NPs (Figure E.2).

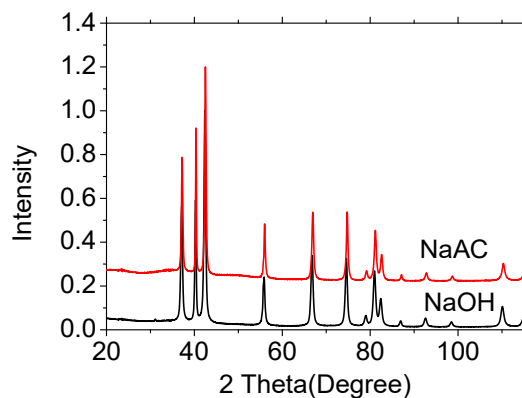
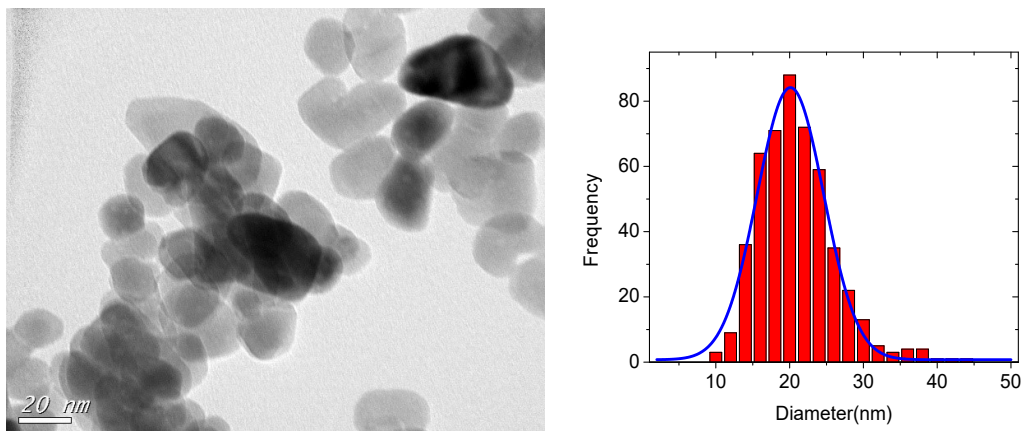


Figure E.2. XRD diffractogram of DEG-ZnO NPs synthesized with  $\text{Na}^+$ .

Because DEG is a hygroscopic liquid, there is amount of water in precursor and unknown amount of water in DEG. With catalyst  $\text{Na}^+$  and water, the chemical reaction is probably too fast, it leads to an uncontrolled crystal growth at different directions.

### With dried salt

In those experiments, we slowed down the synthesis rate, by dismissing catalysts ( $\text{Na}^+$ ).  $\text{Zn}(\text{Fe})\text{O}$  NPs ( $R_{\text{Fe}} = (0, 0.01, 0.1 \text{ and } 0.20)$ ) were synthesized with dried acetate.



*Figure E.3. TEM image and size distribution of DEG-ZnO NPs with dried salt.*

TEM and size distribution of ZnO NPs with dried salt shows that the NPs is uniform in size and shape and the average diameter of pure ZnO NPs is about 20 nm (Figure E.3).

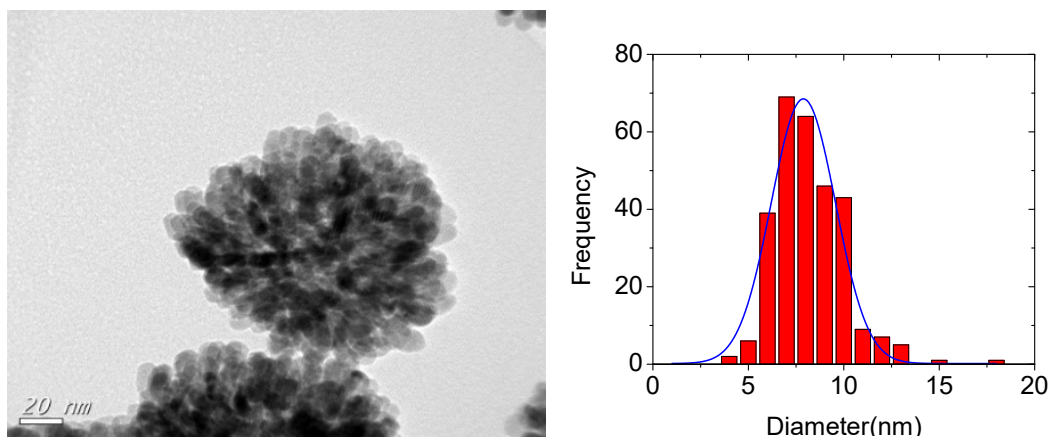


*Figure E.4. TEM image and size distribution of DEG-0.01 with dried salt.*

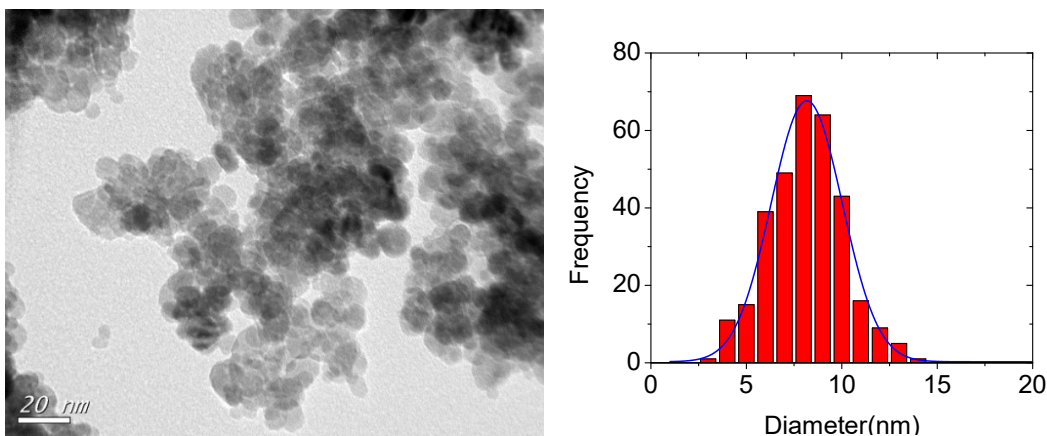


*Figure E.5. TEM image and size distribution of DEG-0.2 with dried salt.*

The TEM images of Zn(Fe)O NPs  $R_{Fe} = 0.01$  and  $0.2$  ( Figure E.4, Figure E.5) show that the NPs is round shape, average size is 8 nm and narrow distribution. XRD diffractogram of pure Zn(Fe)O ( $R_{Fe} = 0$  and  $0.1$ ) is shown in Figure E.6.

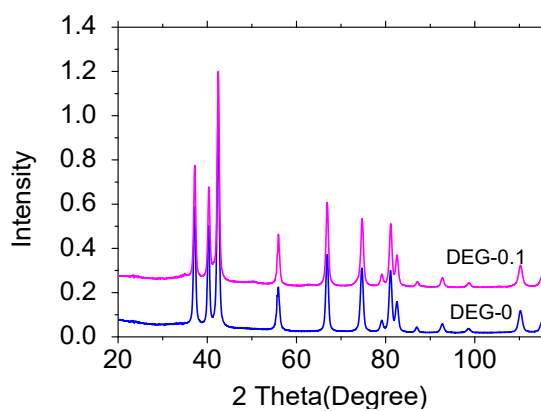


*Figure E.6. XRD diffractogram of pure ZnO and DEG-0.1.*

## **Appendix F. Carboxymethyl pullulan synthesis**

### **Carboxymethyl pullulan (CMP) synthesis**

1 g of pullulan (Hayashibara, Japan) was mixed with 1.35 g powder of sodium hydroxide, followed by the addition of 8 ml of propan-2-ol and 2 ml of water. It was then mixed with a solution containing 1.5 g of monochloroacetic acid in 2 ml of propan-2-ol. The pullulan carboxymethylation was carried out under stirring (200 rpm) at room temperature for 4 hours. The reaction was then stopped by adding 50 ml (70%) water ethanol (v / v) to the mixture. The CMP was filtered off, washed four times with (70%) ethanol-water (v / v) and diethyl ether before being dried overnight at 50 °C under vacuum to give white powder with a yield of 70%.

### **Determination amount of CM in CMP**

The degree of substitution (DS) of the carboxymethyl groups (CM), which relative to number of CM per unit of pullulan anhydroglucose, was obtained by conductometry.

First, approximately 100 mg of CMP was dissolved in 100 ml of HCl (0.05 M) and the pH adjusted to about 2.0 with dilute NaOH. The solution was then titrated with NaOH (0.05M). The titration curve is presented in Figure F.1. The first part of the curve (below  $V_1$ ) corresponds to the neutralization of the  $H^+$  ions originating from the strong HCl acid initially added, the plateau (from  $V_1$  to  $V_2$ ) is due to the neutralization of the carboxylic groups, while the last increase in conductivity (above  $V_2$ ) corresponds to an excess amount of NaOH.

The number of moles of CM is equal to that of NaOH in volume  $V_2 - V_1$  ( $V_{NaOH}$ ). The degree of substitution (DS) of CM can be calculated from 5 titrations in Table F.1. The results indicate that DS of CM is 1.

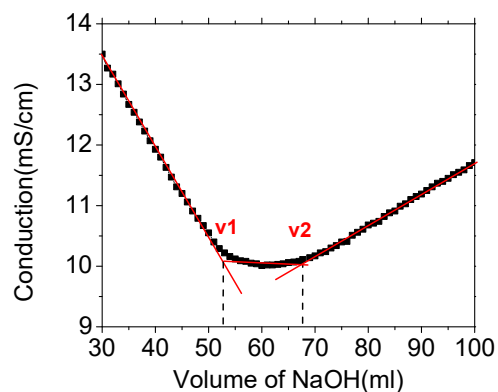


Figure F.1. Determination amount of CM in CMP

Table F.1. The degree of substitution of CM

Fraction	V NaOH (ml)	n CM (mmol)	m CMP (mg)	n CMP (mmol)	c CM (mmol/g)	DS CM
1	10.2	0.510	107.7	0.6262	4.7354	0.81449
2	10.3	0.515	107.7	0.6262	4.7818	0.82247
3	14.8	0.740	100.4	0.5837	7.3705	1.26773
4	12.9	0.645	107.7	0.6262	5.9889	1.03008
5	13.9	0.695	107.7	0.6262	6.4531	1.10994
Average					5.86593	1.00894

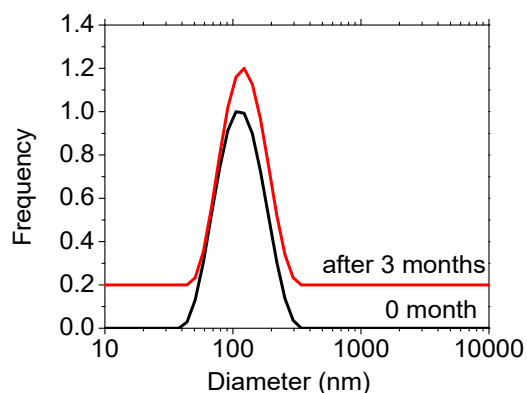


Figure F.2. Size distribution of CMP-0.50 NPs.

We coated our NPs with CMP. We measured the hydrodynamic diameters and the zeta-potentials of CMP-NPs with DLS (see Figure F.2). The results indicated that the size of CMP-NPs was about 145 nm with a charge surface of -24.8 mV. After 3 months, this value did not change evidencing the excellent stability of the suspension.

## Appendix G. Characterization of PEG-NPs

Polyethylene glycol with phosphonic acid and carboxylic acid end groups ( $M=2500$  g/mol, Specificpolymers) is one relevant polymer to graft on nanoparticles which PEG chain could limit early elimination in vivo. Its phosphonate group would allow strong interaction with Zn and Fe ions at the surface of the NPs and carboxylic end group ensures solubility in neutral pH water. It also offers grafting possibilities.

### Hydrodynamic size and stability

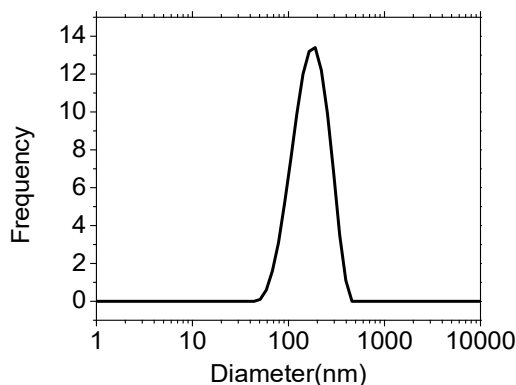


Figure G.1. Size distribution of PEG-0.50.

The DLS results indicate that the size of PEG-0.50 was about 135 nm (Figure G.1), with zeta-potential of  $-8.4$  mV, in good agreement with carboxylic end groups on PEG chain.

### Magnetic properties

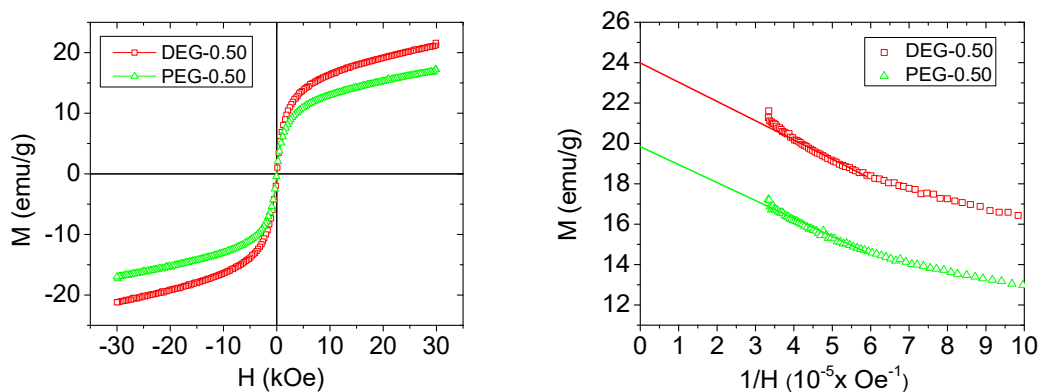


Figure G.2. Magnetization ( $M$ ) versus applied field ( $H$ ) of DEG-0.50 and PEG-0.50.

The saturation magnetizations of PEG-0.50 was 20 emu/gram (see Figure G.2).

## Infrared absorption spectroscopy

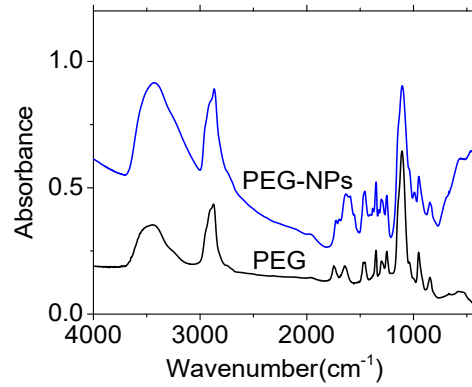


Figure G.3. Infrared absorption spectra of PEG-0.50.

FT-IR spectral evidenced PEG coating in the studied samples (Figure G.3).

## Thermogravimetry analysis

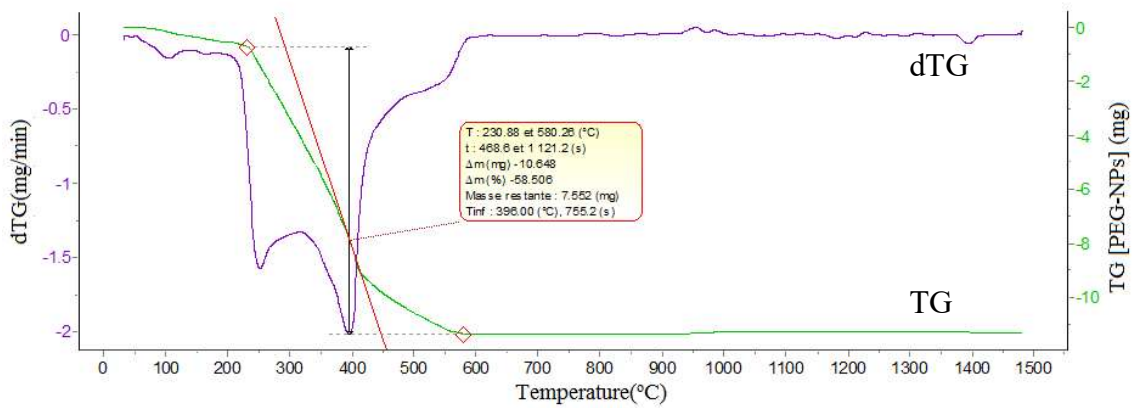


Figure G.4. Thermogram of PEG-0.50.

By analyzing thermogram, we determined that PEG-0.50 contained 58.5% of organic coating (Figure G.4).

## Appendix H. Characterization of fucoidane-NPs with different Fe concentration

We determined the magnetic properties of the coated NPs at 300 K when the applied field ranged from  $-30$  to  $+30$  kOe. Hysteresis plots show the variation of magnetization ( $M$ , emu/g) as a function of applied magnetic field ( $H$ , Oe).

The magnetism properties of fucoidan-coated NPs with different Fe concentration were investigated (Figure H.1). The results indicated that fuco-NPs ( $R_{Fe, I} = 0.05, 0.15,$  and  $0.35$ ) are paramagnetic and fuco-0.50 are superparamagnetic.

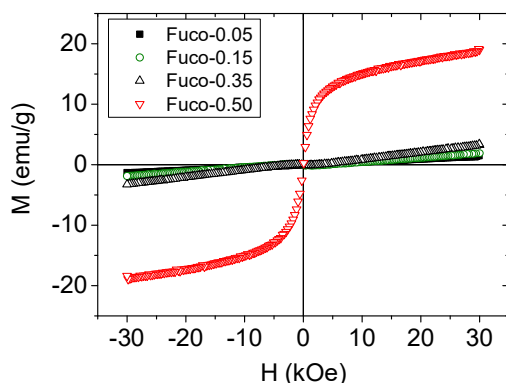


Figure H.1. Magnetization ( $M$ ) versus applied field ( $H$ ) curves of fuco-NPs with different Fe concentrations.

We measured the absorbance spectra of fuco-NPs with different Fe concentration. The results indicated that the absorption wavelength was in UV band. With low concentration of iron, the fuco-0.05 had a peak at 270 nm corresponding to the band gap of zinc oxide. For higher concentrations of iron, the peak at 270 nm was less pronounced (Figure H.2).

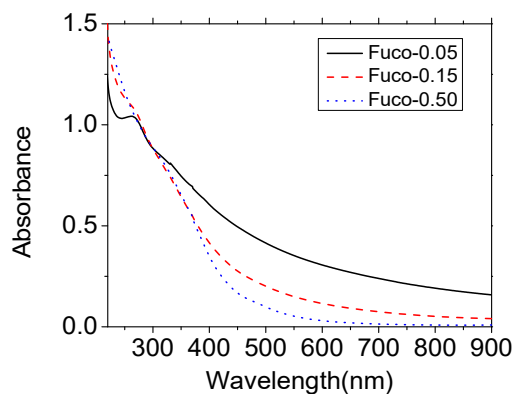


Figure H.2. Absorption spectra of fuco-NPs with different Fe concentrations.

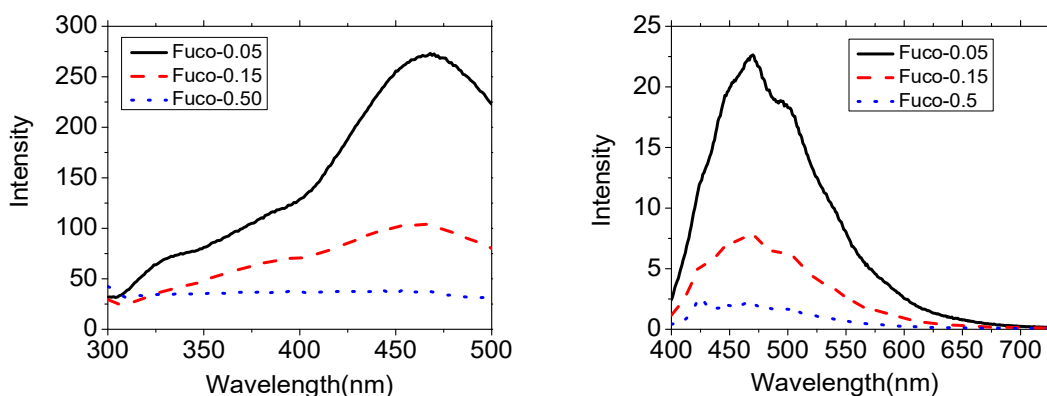


Figure H.3. Fluorescence spectra of fuco-NPs with excitation wavelengths of 270 nm (left) and 370nm (right) with different Fe concentrations.

The fluorescence intensity of coated NPs show that with higher concentration of Fe we had a lower fluorescence intensity (Figure H.3).

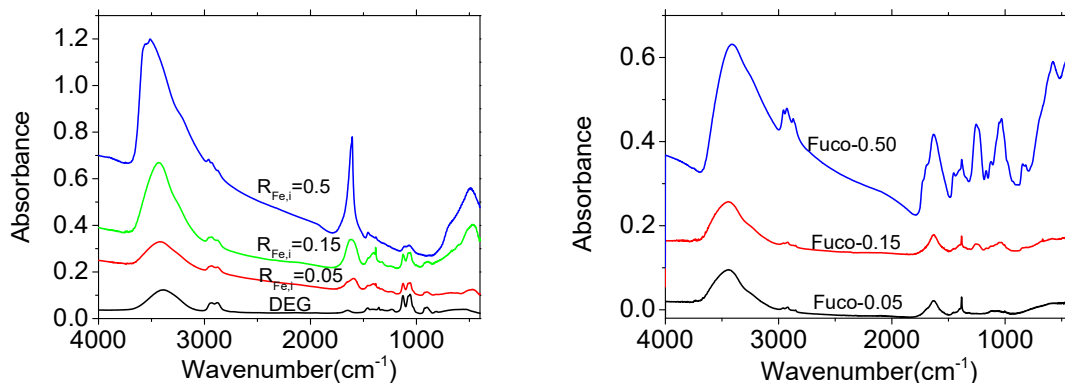


Figure H.4. Infrared absorption spectral of bare NPs and Fu-NPs with different Fe concentration.

Infrared absorption spectral evidenced fucoidan in the samples (Figure H.4).

## Appendix I. TEM images, size distribution and XRD spectra

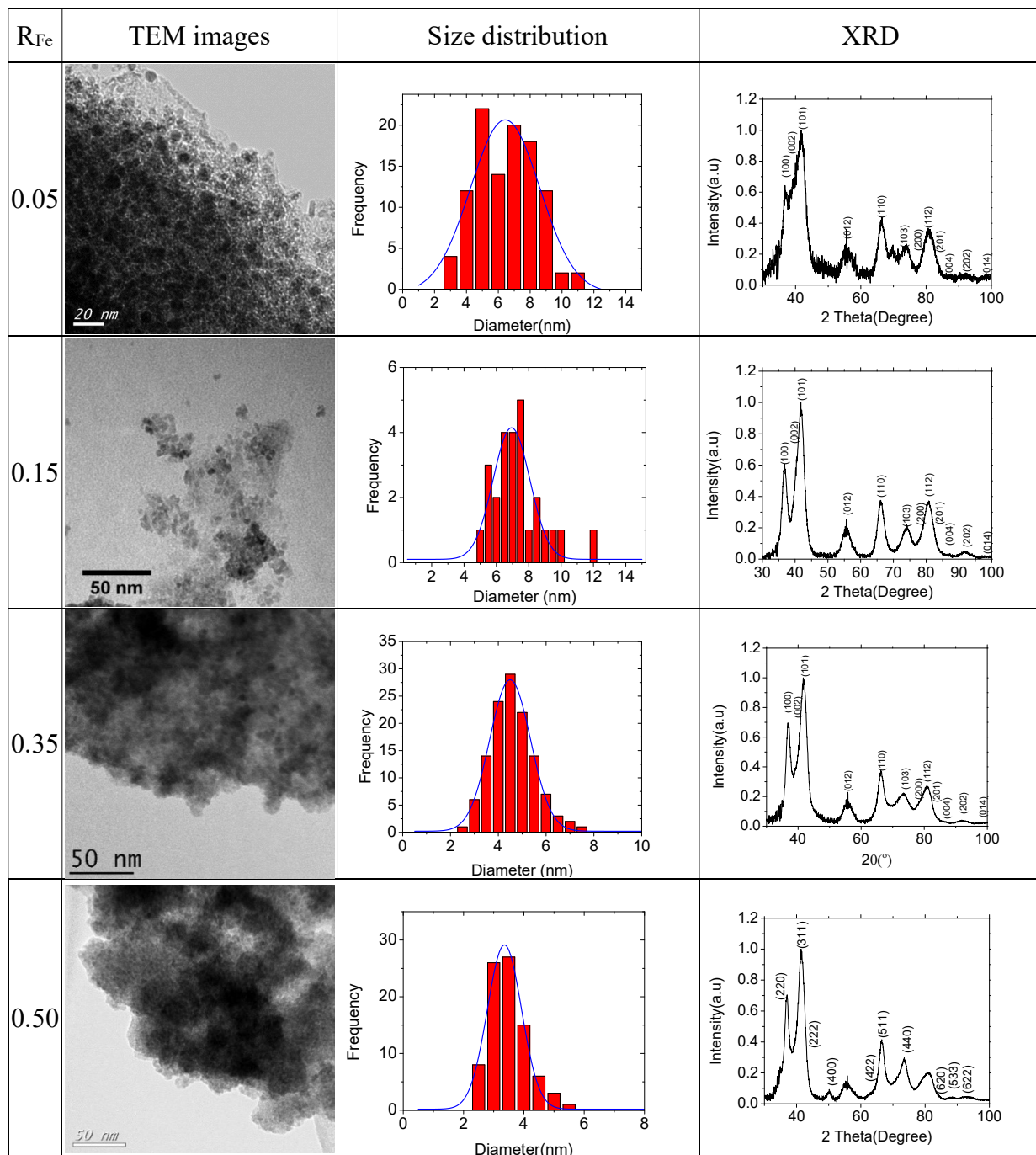


Figure I.1. TEM images, size distribution and XRD spectra of NPs.

TEM images, size distribution and XRD spectra of NPs with different concentration of Fe is presented in Figure I.1.

## Appendix J. XRD analysis report

The results of XRD analysis are gathered in Table J.1. Stoichiometric formulae proposed with our hypothesis have been added in bold characters on DEG-0.35 and DEG-0.5 panels. Rietvelt refinements have been performed with MAUD software and JCPDS card from  $Zn_{0.82}Fe_{0.123}O$  which allow the best fit with experimental data.

*Table J.1. XRD analysis report*

DEG-0.05	
Lattice parameters (nm):	a: 0.325839±6.68E-5; c: 0.53225±2.05 E-4
Coherent domains of diffraction (nm):	5.862±0.18
Microstrain :	1.79 E-2±3.87 E-4

DEG-0.1	
Lattice parameters (nm):	a: 0.32691±3.7 E-5; c: 0.52280±8.9 E-5
Coherent domains of diffraction (nm):	6.965±0.09
Microstrain :	8.1 E-3±1.7 E-4

DEG-0.15	
Lattice parameters (nm):	a: 0.327126±4.6 E-5; c: 0.52281±1.156 E-4
Coherent domains of diffraction (nm):	6.726±0.05
Microstrain:	8.6 E-3±8.55 E-5

DEG-0.35	
JCPDS : Zn <sub>0.82</sub> Fe <sub>0.123</sub> O Lattice parameters (nm):	a: 0.327094±2.83 E-5; c: 0.531681±2.83 E-5
Coherent domains of diffraction (nm)	5.78±0.22
Microstrain:	1.93 E-2±2.29 E-4

DEG-0.5	
JCPDS : Zn <sub>0.82</sub> Fe <sub>0.123</sub> O Lattice parameters (nm):	a: 0.32499±1.78 E-4; c: 0.530024±3.87 E-4
Coherent domains of diffraction (nm) / phase % (Volume-Weight)	3.85±0.36 33.4 ±0.46% _ 44.88%
Microstrain:	8.26 E-3±2.07 E-3
Zn Fe <sub>2</sub> O <sub>4</sub> Lattice parameters (nm):	a: 0.84752±4.39 E-4
Coherent domains of diffraction (nm) / phase % (Volume-Weight)	4.07±0.1 66.6 ±0.86%_55.12%
Microstrain:	8.11 E-5±4.33 E-3

## **Appendix K. Gaussian fit and center of mass method**

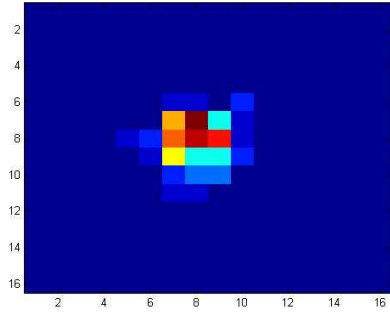
In this part, the speed and accuracy of Gaussian fit with least squares method and center of mass method were investigated with simulation data.

Using a Monte Carlo method, we simulated the Gaussian image of NPs received by a CCD camera. We used two algorithms to determine the position of the NPs. By comparison between the simulated location of NPs and the locations calculated by the two algorithms, it is possible to evaluate the accuracy of these methods.

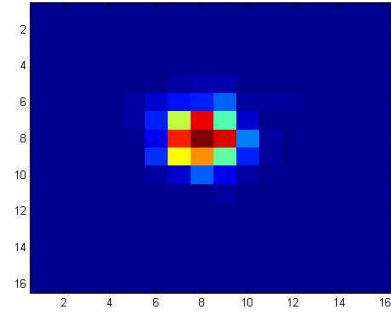
Single NP can be seen via microscopy if the number of photons emitted is large enough compared to the background noise. The 2D image of a NP is related to the Airy disk (a cut of the PFS - Point Spread Function of the imaging system). Because the Airy disk is similar to a Gaussian function, we used in this simulation a Gaussian approximation in order to reduce computing time.

Noise is an unwanted signal in measurements. Noise in the images obtained from the CCD camera may be due to thermal noise, intrinsic sensor noise, background noise that causes errors in locating process.

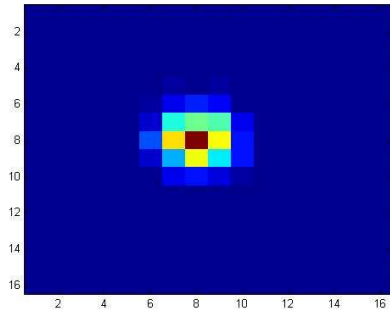
Using a Monte Carlo method, we simulated some images of NPs in 2D Gaussian distribution with several intensities and a noise which are similar to the parameter obtained in real images captured by the CCD camera. Simulated images of NPs with different collected photons count and noise are shown in Figure K.1.



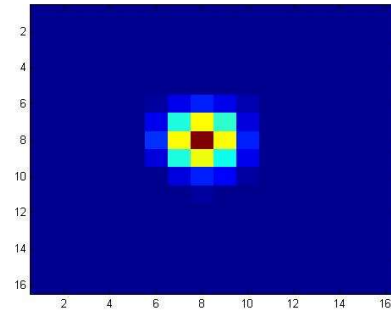
100 collected photons, no noise



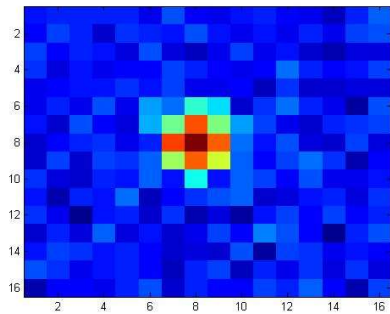
500 collected photons, no noise



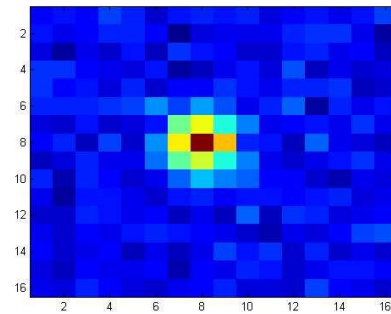
1000 collected photons, no noise



10000 collected photons, no noise



1000 collected photons, shot noise



1000 collected photons, shot noise and DC background

*Figure K.1. Simulated image of NPs with different collected photons count and noise.*

### Data without noise

Here we study images without noise and with 1000 incoming photons for each NP simulation. The number of NPs surveyed is 10000. We look at the error and the calculation speed of each of the two algorithms.

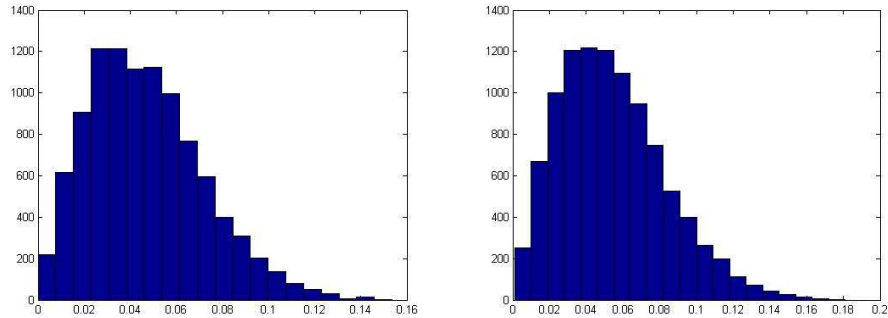


*Figure K.2. Error histograms of the center of mass method algorithm (left) and of the Gaussian fitting method algorithm, without noise.*

The results show that the error of the center of mass method algorithm is 0.047 pixel and elapsed time for every calculating is 9 ms. The error of the Gaussian fitting method is 0.054 pixel and the elapsed time for each run is 24 ms. Center of mass seems to be a little better and a lot faster (Figure K.2).

### Data with shot noise

Simulated images were added with shot noise with the SNR equal to 1. 1000 incoming photons are allowed for each NP simulation. The number of NP surveyed is 10000. The results show now that the error of the center of mass method algorithm is 0.071 pixel whereas the error of Gaussian fit method is 0.054 pixel (Figure K.3). Time is unchanged.

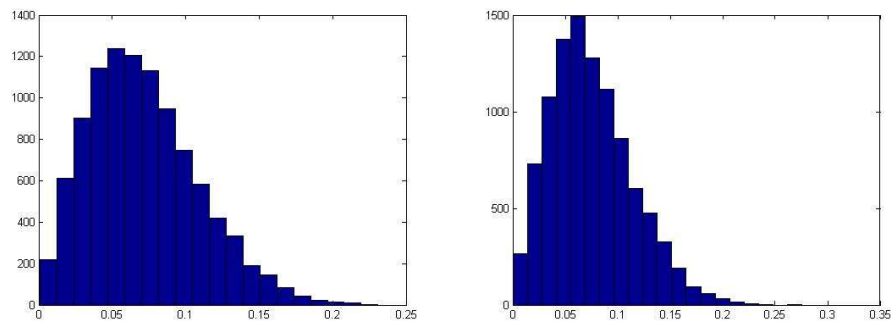


*Figure K.3. Error histogram of the center of mass method algorithm (left) and the Gaussian fitting method algorithm, with shot noise.*

## Data with shot noise and background

Again, we simulated images with a shot noise at a SNR equal to 1. We add a DC noise with SNR equal to 0.5. 1000 incoming photons are played for each NP simulation. The number of NP surveyed is 10000.

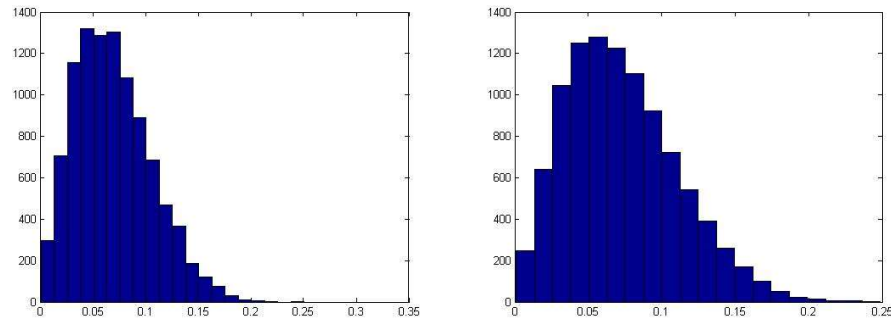


*Figure K.4. Error histogram of the center of mass method algorithm (left) and the Gaussian fitting method algorithm, with shot noise and background*

The results show now that the error of the center of mass method algorithm is 0.07 pixel and the error of Gaussian fit algorithm is 0.073 pixel (Figure K.4). With the same range of error, the computation time of the center of mass method (9 ms) is much lower than that of the Gaussian fitting by the least squares method (24 ms).

## Number of incident photons

In Figure K. 5, we can see that, if the collected photons count is less than 5000 photons, the center of mass is more accurate. The Gaussian fit algorithm gives better results with more than 5000 photons. The center of mass is a very good algorithm for quickly locating NPs with subpixel resolution. With its very fast estimation time, this algorithm is suitable for tracking NPs in real-time.

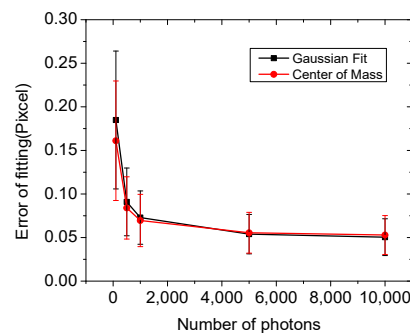


*Figure K.5. Error of the Gaussian fit algorithms and the center of mass algorithms versus the number of incoming photons*

## Appendix L. Accuracy of the 3D location algorithm

### Data simulation

We used again a Monte Carlo method in order to simulate the interference images of NPs as seen by the CCD camera. From the simulation of the location of the NPs and their distance from the focus plane, it is possible to study the accuracy of our image correction in 3 dimensions. The noise level is fixed at 100 photons for each simulation. The simulated interference images at a distance equal to  $30\ \mu\text{m}$  from the focus plane with different signal to noise ratio (SNR) values in Figure L.1.

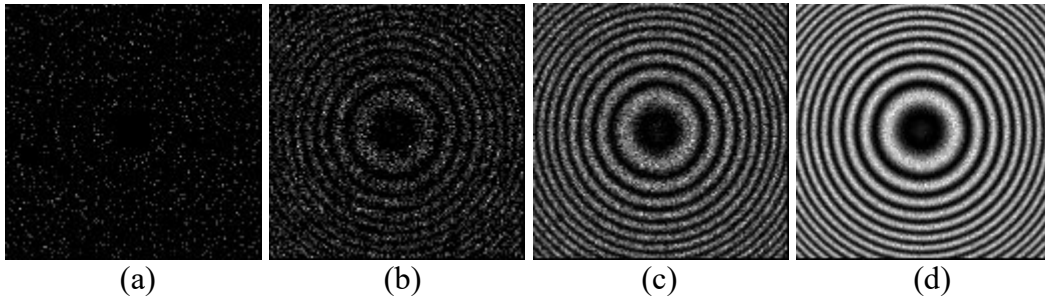


Figure L.1. Simulated interference images of NP versus SNR: 10 (a), 100 (b), 1000 (c), and 10000(d)

### Accuracy versus noise

By definition, noise is an unwanted signal in measurements. Noise in the images obtained from the CCD may be due to thermal noise, electronic noise in the camera itself, background noise that cause errors in the locating process. As the results of our simulations of interference images, as a function of the SNR, show, the SNR value should be better than 10 for sub-pixel accuracy. Interference images of NPs at several distances from the focus plane ( $z$ ) were also simulated (SNR =1000). The results of simulations indicate that the vertical limit for subpixel resolution ranges from 5 to  $50\ \mu\text{m}$  (Figure L.2).

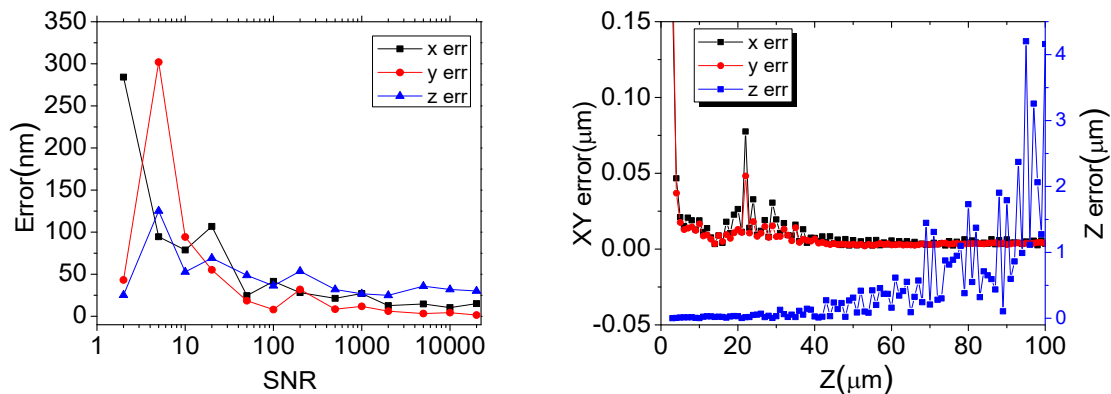


Figure L.2. Error versus SNR (left) and distance to focus plane (right).

## Appendix M. Matlab code for hyperspectral microscopy imaging

```
clear all;
close all;

BackGround = double(imread('BackGround.tif')); %Load Back Ground image
load 'NanoSpectrum.mat'; % Load spectrum of NPs
load 'LampSpectrum.mat'; % Load spectrum of lamp

FileDir='F:\hyper\znodata1\';
FileType='.tif';
FormatOfNumber='%d';
FileCounter=0;
NumberOfFile=630;
NumberString=sprintf(FormatOfNumber,FileCounter);
FileName=sprintf('%s%s%s',FileDir,NumberString,FileType);

IMGRaw= double(imread(FileName));
[nr,nc]=size(IMGRaw);
cube=zeros(nr,nc,NumberOfFile);

%*****
% Build wavelength array
startwave=400;
WlStepRatio=0.79365;
wavearray=(0:NumberOfFile-1)*WlStepRatio+startwave;

%*****
% Build cube of image versus wavelength
FileCounter=0;
while (FileCounter<NumberOfFile)
    NumberString=sprintf(FormatOfNumber,FileCounter);
    FileName=sprintf('%s%s%s',FileDir,NumberString,FileType);
    FileCounter=FileCounter+1;
    if exist(FileName,'file')
        cube(:, :,FileCounter)= double(imread(FileName));
        disp(wavearray(FileCounter));
    end
end
end
```

```

%*****
% Build image using SAM
anpha=zeros(nr,nc);
RefSpectrum=NanoSpectrum./Lampspectrum;
for i=1:nr
    for j=1:nc
        PixelSpectrum(1,:)=cube(i,j,:);
        PixelSpectrum(1,:)=PixelSpectrum(1,:)./Lampspectrum;
anpha(i,j)=acos(sum(PixelSpectrum(1,:).*RefSpectrum)/sqrt(sum(RefSpectrum.^2)*sum(Pixel
        Spectrum(1,:).^2)));
    end
end

%*****
% Detecting NPs by set a threshold filter
anpha2=anpha;
theshold=mean(mean(anpha2));
for i=1:512
    for j=1:512
        if anpha2(i,j) >theshold;
            anpha2(i,j)=theshold;
        end
    end
end

%*****
% Imaging and saving data
imagesc(anpha2);
colorbar
imwrite(anpha2*256,'HyperIMG.tif');

```

## Appendix N. Determination of iron content of the NPs by visible spectroscopy

Colorimetric analysis using spectrometer is a simple, fast, cheap, and reliable method. It can be used for determination amount of iron in samples [194]. The colorimetric analysis can provide us the ratio between weight of Fe and weight of NPs sample ( $m_{Fe}/m_{NPs}$ ) but it cannot be used to calculate  $R_{Fe}=Fe/(Zn+Fe)$  (mol/mol) directly, because there are amounts of other elements such as DEG,  $H_2O$  in the sample.

However, we can determine  $R_{Fe}=Fe/(Zn+Fe)$  (mol/mol) using colorimetric analysis by comparing with AAS data as the references because both of colorimetric analysis and AAS can give us the value of  $m_{Fe}/m_{NPs}$ . We assume that  $R_{Fe}$  versus  $m_{Fe}/m_{NPs}$  is a linear function ( $y=ax+b$ ). We can determine the values for variables of this function by using linear fitting with the ASS data (see Figure N. 1). In our case, the values of variables are:  $a = 18$ ,  $b = -0.054$ , and the  $R_{Fe}$  can be estimated as Table N.1.

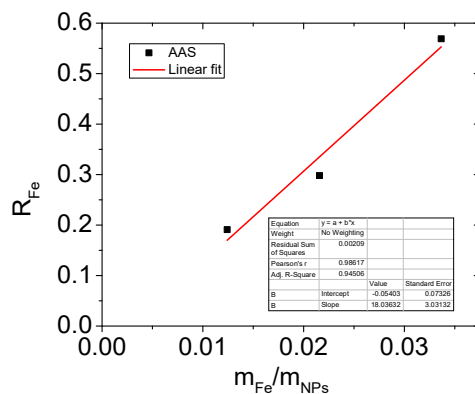


Figure N.1. Determination of relationship between  $R_{Fe}$  and  $m_{Fe}/m_{NPs}$ .

Table N.1. Estimation of  $R_{Fe}$  in samples

Sample	$m_{NPs}$ (mg)	$m_{Fe}$ (mg)	$m_{Fe}/m_{NPs}$	$R_{Fe}$ (mol/mol)
DEG-0.05	1.2	0.0078	0.0066	0.064
DEG-0.15	0.9	0.0116	0.0129	0.179
DEG-0.35	0.5	0.0143	0.0286	0.461